

DISS. ETH No. 14577

**LOCAL MESH REFINEMENT
ALGORITHMS FOR ENHANCED
MODELING CAPABILITIES IN THE
FDTD METHOD**

A dissertation submitted to the
SWISS FEDERAL INSTITUTE OF TECHNOLOGY
ZURICH

for the degree of
Doctor of Technical Sciences

presented by
NICOLAS PIERRE CHAVANNES
Dipl. El.-Ing. ETH, Switzerland
born April 25, 1972
citizen of Switzerland

accepted on the recommendation of
Prof. Dr. W. Fichtner, examiner
Prof. Dr. N. Kuster, Prof. Dr. L. Martens, co-examiners

2002

Contents

Summary	v
Zusammenfassung	ix
List of Acronyms	xiii
Acknowledgments	xvii
I Introduction	1
1 Motivation and Objectives	3
2 The Finite-Difference Time-Domain Technique	7
2.1 The FDTD Method Applied to Electromagnetics	7
2.1.1 Introduction	7
2.1.2 Discretizing Maxwell's Equations	8
2.1.3 Stability	11
2.1.4 Modeling of Boundaries	12
2.1.5 Implementation / Integration into Simulation Environments	14
3 Limitations of the FDTD Scheme with Respect to Spatial Resolution	21
3.1 Numerical Errors Caused by Stair-Stepped Modeling Approximations	21
3.1.1 Introduction	21
3.1.2 Investigations Based on Numerical Experiments	23
3.1.3 Investigations Based on Analytical Approaches	25

4	Overview of Modeling Techniques for Local Grid Refinement in the FDTD Method	33
4.1	Introduction	33
4.2	Cartesian Grids	34
4.2.1	Homogeneous Cartesian Grids	34
4.2.2	Graded / Non-Equidistant Cartesian Grids	35
4.3	Globally Non-Orthogonal Grids	35
4.4	Locally Unstructured Grids / Subcell Approaches	36
4.4.1	Contour-Path (CP) Related Methods	36
4.4.2	Subcell Algorithms Based on the Incorporation of Static Field Solutions	39
4.4.3	Algorithms Applied to Thin Structures	40
4.5	Subgrids	42
4.6	Hybrid Approaches	45
4.7	Conclusion	46
II	Algorithms for FDTD Local Mesh Refinement	63
5	A Novel 3-D CPFDTD Scheme for Modeling Grid Non-Conformally Aligned Transmitter Structures	65
5.1	Introduction	65
5.2	Numerical Methods	67
5.2.1	3-D CP Modeling Of Wire Structures	68
5.2.2	3-D CP Modeling of Extended Solid Objects	73
5.2.3	Modeling of the Source	74
5.2.4	Stability Considerations	77
5.3	Results and Validation	78
5.3.1	Dipole Antenna	79
5.3.2	Generic Phone	83
5.4	Conclusions	84
5.5	Appendix	87
5.5.1	Subcell Contour-Path Modeling of Dielectric Structures in FDTD	87
6	A Robust FDTD Local Refinement Scheme for General Application to Enhanced Antenna Analysis	93
6.1	Introduction	94
6.2	Method	95

6.2.1	Spatial Interpolation Algorithm	95
6.2.2	Temporal Updating Scheme	98
6.2.3	Special Treatment of Traversing PEC Materials	100
6.2.4	Integration Into a TCAD / Automeshing Environment	100
6.3	Reflection and Stability	101
6.3.1	Reflection from Boundary	101
6.3.2	Stability Considerations	102
6.3.3	Grid Nesting Capability	105
6.4	Conclusions	106
 III Benchmarks and Applications		111
7	Benchmarks:	
	Antennas Embedded in Complex Environments	113
7.1	Benchmarks	113
7.1.1	Helical Antenna on PEC Ground Plane	113
7.1.2	Helical Antenna on Generic Phone at 900 MHz	116
7.1.3	Generic Phone - SAM Phantom	119
7.2	Discussion: Computational Efficiency	122
8	RF Design of Mobile Phones by TCAD: Suitability and Li-	
	mitations of FDTD	127
8.1	Introduction	128
8.2	Mobile Phone	130
8.3	Numerical Method	131
8.4	Measurement Technique	132
8.5	FDTD Modeling	132
8.5.1	Implementation of Phone	132
8.5.2	Source Representation	135
8.5.3	Grid Generation / Simulation Parameters	137
8.6	Results and Validation	138
8.6.1	Validation of Antenna Model	139
8.6.2	EM Field Distribution - Free Space	141
8.6.3	Effect of the LCD Holder Connection	141
8.6.4	Radiation Pattern - Free Space	144
8.6.5	Performance at Flat Phantom	145
8.6.6	Performance at the SAM Head	149
8.6.7	Performance at Human Head	153
8.6.8	Radiation Pattern - SAM Phantom	153

8.6.9 Computational Requirements	154
8.7 Conclusions	155

IV Conclusions	161
9 Conclusion and Outlook	163
A List of Symbols	167
B Bibliography	169

Summary

The trend to mobility and miniaturization in communication, computing and medicine is clearly heading toward a fusion of these subsystems in *per-vasive computing* - interconnected intelligent subsystems providing numerous services embedded within human surrounding environments - a vision rapidly becoming reality within everyday life. Additional increasing consumer demand for attractive performance/price ratios as well as international mandatory safety guidelines addressing radio-frequency (RF) related possible health effects confront engineers with the development of highly efficient devices.

The exponential growth of computational power within recent decades has established a significant position for numerical simulation techniques, efficiently supporting product research and development (R&D) processes. The Finite-Difference Time-Domain (FDTD) method in particular has been chosen by many research institutions as the leading technique due to its general applicability.

Although activities in this area had a late start at ETH Zurich, the project EMSIM conducted within the Swiss research priority program MINAST as well as the currently running project SEMCAD++ supported by the Swiss Commission for Technology and Innovation (KTI) enabled IIS and IT'IS together with two local industry partners to form a widely recognized competence center in EM simulation methodology and near-field analysis within only a few years. Some of my research and development work conducted as a team member for these projects is condensed within this thesis.

The objectives of my thesis were derived from the obvious major drawbacks of the current implementations of FDTD. These are restricted spatial resolution and poorly realized computer aided design (CAD) environments, in addition to unknown uncertainties in the computation results obtained by the method. The development of novel robust FDTD local grid refinement schemes combined with and integrated into user-friendly electromag-

netic (EM) simulation environments became the main focus of this research work, whereby my colleagues concentrated more on algorithms improving the FDTD method's accuracy.

Part I of this thesis is attributed toward providing the scientific and theoretical background which underlies the numerical algorithms developed within the framework of this thesis. In chapter 3, a special focus is assigned to investigations related to the limitations of the FDTD method with respect to spatial grid resolution, i.e., *staircasing* errors. Conclusions reveal the significant contribution of errors caused by stair-stepped perfectly electric conductors (PEC) over dielectric material. Furthermore, the type of polarization applied to EM excitation and incidence on a PEC scatterer plays a major role, leading to large global effects in the entire computational domain, e.g., due to virtually excited non-physical EM waves. Chapter 4 provides a review of schemes proposed for improving the spatial resolution in the FDTD method. Particular attention is thereby drawn to methods which are related to this thesis, i.e., subcell and subgrid techniques.

The development of two novel algorithms for FDTD local grid refinement is documented in the second part of this thesis. Both methods have been chosen for development and implementation based on the findings from the literature survey. In chapter 5, a novel 3-D subcell technique is presented which enables improved representation of grid non-conformally aligned transmitter structures, further enhanced by a new source model adapted to such configurations. Whereas the literature heavily discusses scattering problems from mainly 2-D objects, a study dealing with subcell modeled active antenna structures had not been addressed thus far. A number of examples demonstrate the capabilities of the technique, benchmarked against stair-cased examples and validated by experimental data from the DASY4 near-field scanning system. In the appendix of the chapter, an extension of the method to dielectric structures is briefly discussed.

Chapter 6 presents a novel 3-D subgrid algorithm based on enhanced spatial interpolation as well as a new temporal scheme especially developed for this kind of multi-grid technique. Compared to existing algorithms it provides superior performance with respect to refinement by grid nesting, low reflections, robustness and general applicability, in particular when embedded within the SEMCAD solid modeling and automated grid generation environment. A rigorous validation of the scheme was carried out on the basis of benchmark examples with increasing modeling complexity, continuously cross-validated against highly resolved FDTD reference solutions, other numerical methods as well as measurements by examination of parameters from the near- and far-field, leading to excellent agreement between

the applied assessment techniques.

In the third part, the subgridding scheme - since already implemented into the SEMCAD simulation environment - is applied for the analysis of a broad variety of highly non-homogeneous near-field configurations related to mobile communications. Chapter 7 presents multiple examples of antenna simulations, namely helical antennas, which have often been poorly represented in previous studies. The novel techniques enable the detailed modeling of such structures and demonstrate the clear necessity of an appropriate spatial resolution to achieve improved accuracy for sensitive near-field parameters such as the feedpoint impedance. Furthermore, the definite advantages of local refinement techniques for reduced computational requirements are shown. All obtained results are benchmarked against experimental data.

The objective of Chapter 8 was to demonstrate that these improvements enable the easy and efficient application of FDTD beyond generic setups, e.g., metal boxes with wire antennas. For this reason, one of the latest commercial multi-mode handsets was thoroughly electromagnetically analyzed based on the electro-mechanical CAD file of the phone. The performance was analyzed in free-space as well as in the vicinity of various biological scatterers. All data was compared to measurements obtained by the DASY4 near-field scanner. The simulations could accurately predict all performance parameters, even the smallest changes in the grounding of elements. To our knowledge, this was the most detailed analysis of a real-world handset scenario ever conducted and clearly demonstrated the power of the implementation for industrial R&D departments, especially since the simulation could be completed within a few days.

Readers should note that this thesis consists of independent journal papers, resulting in unavoidable repetitions, mainly in the introductory sections of the chapters. Furthermore, a large amount of coding conducted in the framework of this thesis is not documented here. This became necessary to prepare the SEMCAD platform for implementation of these algorithms and their resulting visualizations.

Zusammenfassung

In den Bereichen Kommunikation, EDV sowie Medizin ist eine deutliche Tendenz hinsichtlich Mobilität und Miniaturisierung feststellbar, was schliesslich zur Verschmelzung der einzelnen Untersysteme führen wird. Die Vision des *Pervasive Computing* - intelligente, in unsere Umgebung eingebettete und miteinander verbundene Untersysteme, welche eine Vielzahl unterschiedlicher Dienste anbieten - werden schnell zum wesentlichen Bestandteil des Alltags. Die zudem stetig steigende Nachfrage nach ansprechendem Preis/Leistungs Verhältnis sowie internationale Richtlinien hinsichtlich möglicher Gesundheitsrisiken im Zusammenhang mit Mobilfunk erfordern die Entwicklung immer effizienterer Geräte.

Aufgrund des exponentiellen Wachstums der Leistungsfähigkeit von Computersystemen innerhalb der letzten Jahrzehnte etablierten sich numerische Simulationsmethoden im Forschungs- und Entwicklungsbereich neuer Produkte. Besonders die Finite-Differenzen Methode im Zeitbereich (FDTD) wird aufgrund ihrer allgemeinen Anwendbarkeit innerhalb vieler Forschungseinrichtungen eingesetzt.

Ogleich diesbezügliche Forschungsaktivitäten im Umfeld der ETH Zürich erst innerhalb der letzten Jahre eine Intensivierung erfuhren, etablierten sich die der ETH angegliederten Institutionen IIS und IT'IS in Zusammenarbeit mit zwei schweizer Industriepartnern innerhalb weniger Jahre zu einem angesehenen Kompetenz-Zentrum im Bereich der elektromagnetischen (EM) Simulations- und Nahfeld-Messtechnik. Dies wurde insbesondere im Rahmen des schweizerischen Schwerpunktprogramms MINAST EM-SIM und dem momentan durchgeführten Projekt SEMCAD++ ermöglicht, welches von der Kommission für Technologie und Innovation (KTI) finanziell unterstützt wird. Ein Teil meiner Forschungs- und Entwicklungstätigkeit welcher in diese Arbeit eingebettet ist, wurde im Rahmen der erwähnten Projekte durchgeführt.

Die Zielsetzung meiner Doktorarbeit gründet auf den Hauptnachteilen

der FDTD Methode, welche sich gegenwärtig in den meisten kommerziellen sowie forschungsbedingten Implementationen wiederfinden: eine durch die herkömmliche Methode vorgegebene eingeschränkte räumliche Auflösung des Modells sowie bloss ungenügend ausgearbeitete computergestützte Design (CAD) Programme. Zudem beeinflusst eine Vielzahl von nur spärlich erforschten, durch die Methode vorgegebenen Unsicherheiten, die Genauigkeit der berechneten Resultate. Aufgrund dieser Vorgaben konzentrierte sich die hier vorgestellte Forschungsarbeit hauptsächlich auf die Entwicklung von neuartigen und robusten Methoden zur lokalen Verfeinerung der räumlichen Auflösung und deren Integration in benutzerfreundliche auf graphische Eingabe basierte EM Simulationsprogramme. Die Arbeit meiner Kollegen konzentrierte sich stärker auf die Entwicklung von Algorithmen zur spezifischen Verbesserung der allgemeinen Genauigkeit in der FDTD Methode.

Der erste Teil der hier vorgestellten Arbeit beschäftigt sich mit den wissenschaftlichen und theoretischen Grundlagen auf welchen die im Rahmen dieser Dissertation entwickelten numerischen Algorithmen aufbauen. Der Schwerpunkt des dritten Kapitels liegt in der Untersuchung der durch die FDTD-Methode vorgegebenen Einschränkungen hinsichtlich räumlicher Gitterauflösung, den sogenannten *Staircasing*-Fehlern. Zusammenfassend ist ein deutlich überwiegender Einfluss des auftretenden Fehlers aufgrund von diskretisierten metallischen Strukturen im Vergleich zu dielektrischen Materialien feststellbar. Desweiteren zeigt die Art der Polarisierung einer elektromagnetischen Welle in Bezug zum Einfall auf ein metallisches Objekt eine grosse Wirkung auf bestimmte, sich im ganzen Rechenbereich manifestierende Fehler, z.B. durch virtuelle, aufgrund des *Staircasings* erzeugte EM Moden. Kapitel 4 fasst verschiedene numerische Algorithmen zur Verbesserung der lokalen räumlichen Auflösung in der FDTD Methode zusammen, wobei den Algorithmen, welche in direktem Zusammenhang mit dieser Dissertation stehen, vertieftes Augenmerk zukommt. Dies sind insbesondere *Subgitter*- und *Subzellen*-Methoden.

Die Entwicklung zweier neuartiger Algorithmen zur Verbesserung der lokalen räumlichen Auflösung in FDTD ist im zweiten Teil dieser Arbeit beschrieben. Anhand der in Kapitel 4 durchgeführten umfangreichen Literaturstudie erfolgte die Wahl zur Entwicklung und Implementierung derartiger Algorithmen auf *Subgitter* und *Subzellen* Methoden. Kapitel 5 beinhaltet die Herleitung eines neuen dreidimensionalen (3-D) *Subzellen*-Algorithmus, welcher eine genauere Simulation von Antennenstrukturen erlaubt, deren Geometrie nicht dem FDTD Gitter entsprechend orientiert ist. Um eine an diese Struktur angepasste Anregung zu realisieren, wurde zu-

dem ein neuartiges, verbessertes Quellenmodell entwickelt und implementiert. Zwar werden - im Allgemeinen zweidimensionale - Streuprobleme ausgiebig in der einschlägigen Literatur untersucht, jedoch wurden bisher keine Studien über Subzellenmodelle aktiver Antennen durchgeführt. Die neu entwickelten Methoden wurden schlussendlich an einer Vielzahl von Beispielen validiert und mit experimentellen Daten des DASY4 Nahfeld-Messsystems verglichen, wobei die deutliche Überlegenheit dieses Ansatzes gegenüber herkömmlicher *Staircase*-Modellierung gezeigt werden konnte. Im Anhang des 4. Kapitels findet sich in zusammengefasster Form eine Erweiterung der vorgestellten Methode, angewendet auf dielektrische Strukturen.

In Kapitel 6 wird ein neuartiger dreidimensionaler *Subgitter* Algorithmus vorgestellt. Die verwendete Methode basiert auf einer verbesserten räumlichen sowie einer neu entwickelten, speziell auf derartige Gitterkonfigurationen zugeschnittenen zeitlichen Interpolation. Im Vergleich mit bestehenden Lösungsansätzen bietet die hier beschriebene Methode aufgrund verschiedener Eigenschaften eine deutlich verbesserte Leistungsfähigkeit. Dies beinhaltet unter anderem die Möglichkeit, Gitter zu verschachteln, niedrige Reflexionen am Gitterübergang sowie eine hohe Stabilität und generelle Anwendbarkeit. Eingebettet in die SEMCAD Modellierungsumgebung welche mit einer automatischen Gittererzeugung ausgestattet ist, werden die Vorzüge der Methode unterstrichen. Unter Zuhilfenahme von verschiedenen Beispielen, welche sich durch eine stetig zunehmende Komplexität unterscheiden, konnte eine umfangreiche Validierung des Algorithmus durchgeführt werden. Hierbei wurden elektromagnetische Nah- und Fernfeld-Größen mit Referenzwerten aus hochaufgelösten Simulationen, anderen numerischen Methoden sowie Messdaten verglichen.

Im dritten Teil dieser Dissertation findet der *Subgitter* Algorithmus - da er bereits im SEMCAD Simulationsprogramm implementiert war - Anwendung auf die Nah- und Fernfeld Analyse einer Vielzahl von räumlich stark inhomogenen Simulationsbeispielen aus dem Bereich der Mobilkommunikation. Kapitel 7 konzentriert sich auf die Simulation von Antennenstrukturen, insbesondere von Helixantennen, welche in zahlreichen vorhergehenden Studien unzureichend simuliert wurden. Die Verwendung der hier vorgestellten Algorithmen ermöglicht die detaillierte Modellierung derartiger Geometrien und zeigt anhand unterschiedlicher Resultate die klare Notwendigkeit einer räumlich genügend feinen Auflösung in FDTD Simulationen. Dies gilt im Speziellen für die genaue Berechnung sensitiver Parameter wie z.B. der Fusspunktimpedanz. Insbesondere die durch Verwendung räumlich lokaler Verfeinerungsmechanismen erzielte drastische Reduktion benötigter Computerressourcen wird anhand zweier Beispiele aufgezeigt. Sämtliche Simu-

lationsresultate wurden zudem mit Messdaten validiert.

Das Ziel des achten Kapitels war zu zeigen, dass die neu entwickelten Algorithmen den Anwendungsbereich von FDTD auf einfache und effiziente Weise über einfache Beispiele, z.B. metallische Quader mit Drahtantennen, hinaus erweitern. Hierzu wurde, basierend auf dem CAD Datensatz eines der neusten handelsüblichen *Multiband*-Mobiltelefone, eine gründliche elektromagnetische Analyse durchgeführt. Diese erfolgte im Freiraum sowie in der unmittelbaren Umgebung verschiedener biologischer Streuobjekte, wobei die erhaltenen Simulationsresultate mit Messdaten des DASY4 Nahfeld-Messsystems verglichen wurden. Es gelang, mit Hilfe der Simulation jegliches EM Feldverhalten vorauszuberechnen, sogar Effekte die von kleinen Veränderungen der Masseverbindung einzelner Elemente herrührten. Unserer Kenntnis nach handelt es sich bei dieser Studie um die bisher detaillierteste Untersuchung eines realen Mobiltelefons. Besonders aufgrund der relativ problemlosen und schnellen Modellierung und Simulation innerhalb weniger Tage konnte die Leistungsfähigkeit der im Rahmen dieser Arbeit entwickelten Ansätze und deren Anwendung im Forschungs- und Entwicklungsbereich aufgezeigt werden.

Der Leser sei darauf aufmerksam gemacht, dass die hier vorgestellte Doktorarbeit aus einigen voneinander unabhängigen Veröffentlichungen zusammengesetzt ist. Dies führt hauptsächlich innerhalb der die Kapitel einleitenden Abschnitten zu unvermeidbaren Wiederholungen. Einen wesentlichen Teil dieser Dissertation nahm zudem die Entwicklung und Implementierung von Algorithmen zur Simulation und anschließenden Visualisierung im Rahmen des SEMCAD++ Projekts in Anspruch, die nicht weiter in der vorliegenden Arbeit dokumentiert sind.

List of Acronyms

1-D	One-Dimensional
2-D	Two-Dimensional
3-D	Three-Dimensional
A&P	Antennas & Propagation
AB	Absorbing Boundary
ABC	Absorbing Boundary Condition
ANSI	American National Standard Institute
ARFCN	Absolute Radio Frequency Channel Number
CAD	Computer Aided Design
CDMA	Code Division Multiple Access
CENELEC	Comité Européen de Normalisation Electrotechnique
CFL	Courant-Friedrichs-Lewy
CP	Contour Path
CPFDTD	Contour Path Finite-Difference Time-Domain
CT	Computer Tomography
CW	Continuous Wave
DASY	Dosimetric Assessment System
DCS	Digital Communications System
DTX	Discontinuous Transmission Mode
ELF	Extremely Low Frequencies
EM	Electromagnetic
EMC	Electromagnetic Compatibility
EMI	Electromagnetic Interference
EMSIM	Electromagnetic Simulation Platform
ETH	Eidgenössische Technische Hochschule
FCC	Federal Communications Commission (USA)
FDTD	Finite-Difference Time-Domain
FE	Finite-Element
FEM	Finite-Element Method

FI	Finite Integration
FIT	Finite Integration Technique
FM	Frequency Modulation
FVTD	Finite-Volume Time-Domain
GHz	Gigahertz
GMT	Generalized Multipole Technique
GPIB	General Purpose Interface Bus
GSM	Global System for Mobile Communications
GUI	Graphical User Interface
HDF	Hierarchic Data Format
HP	Hewlett Packard
HR	High Resolution
ICNIRP	International Commission for Non-Ionizing Radiation Protection
IEC	International Electrotechnical Commission
IEEE	Institute of Electrical and Electronics Engineers
IFH	Laboratory for Electromagnetic Fields and Microwave Electronics
IIS	Integrated Systems Laboratory
ISEAG	Integrated Systems Engineering AG
IT'IS	Foundation for Research on Information Technologies in Society
KTI	Commission for Technology and Innovation
LCD	Liquid Crystal Display
MHz	Megahertz
MINAST	Micro & Nano System Technology
MMP	Multiple Multipole Technique
MoM	Method of Moments
MRI	Magnetic Resonance Images
MTE	Mobile Telecommunications Equipment
NEC	Numerical Electromagnetics Code
NWA	Network Analyzer
OpenGL	OpenGL
P3	Pentium 3
P4	Pentium 4
PCB	Printed Circuit Board
PCS	Personal Communications Services
PEC	Perfect Electric Conductor
PML	Perfectly Matched Layer
PP	Post Processing
R&D	Research and Development
RCS	Radar Cross Section
RF	Radio Frequency

RMS	Root Mean Square
SAM	Specific Anthropomorphic Mannequin
SAR	Specific Absorption Rate
SEMCAD	Simulation Platform for Electromagnetic Compatibility, Antenna Design and Dosimetry
SPEAG	Schmid & Partner Engineering AG
SWR	Standing Wave Ratio
TCAD	Technical Computer Aided Design
TDMA	Time Division Multiple Access
TEM	Transverse Electromagnetic Propagation Mode
TH	Transverse Magnetic Propagation Mode

Acknowledgments

In summer 1996 I experienced my first contact with the BIOEM/EMC group, at that time embedded within the Laboratory for Electromagnetic Fields and Microwave Electronics (IFH). Motivated by a lecture on numerical simulation techniques given by Christian Hafner, I contacted Michael Burkhardt in order to participate within a semester work focusing on the numerical simulation of a generic mobile phone using FDTD. Until that time I had not been particularly fascinated by the subject of electrical engineering, although I had chosen it for my studies. However, this rapidly changed from that moment on. Although having had the impression of being embedded within a *very* passionate and time intensive working environment, I began to really enjoy the group and its people: highly professional, warm-hearted and full of a deep team spirit. This passion of the group overtook me, and I consequently decided to extend my stay, first for my diploma thesis and consequently to carry out a PhD thesis.

During the following (almost) four years of my thesis, the structure of the BIOEM/EMC group changed heavily due to mostly communicative challenges within IFH. Fortunately, and due to enormous efforts conducted by Niels Kuster, Thomas Schmid, Quirino Balzano, Prof. Wolfgang Fichtner, Prof. Albert Kündig and Prof. Ralf Hütter, the group was “saved” and reorganized. All PhD students were transferred to the Integrated Systems Laboratory (IIS); moreover, a new institution - the Foundation for Research on Information Technologies in Society (IT²IS) - was originated. This formed, in close cooperation with IIS and two related industry partners (SPEAG and ISEAG), a powerful and rapidly growing environment to continue the success story of the original BIOEM/EMC group.

First of all I would like to express my deep gratitude to Niels Kuster, who distinguishes himself with a unique and wide expertise in the field of bioelectromagnetics, as well as a relentless generosity with respect to almost

everything, except maybe *o-toro sushi*. Although attempting to cure my fear of flying by a rather *brut force* approach, I profited in a great many ways from these opportunities, in particular with our trips to Japan. I experienced him as a great mentor, highly enriching my learning process by assisting almost any time with his founded and comprehensive knowledge, and moreover, by allowing me the freedom to follow my own ideas. Special thanks are addressed to Prof. Wolfgang Fichtner for having accepted supervision of this work, as well as for his great support in “saving” the BIOEM/EMC group. At this point I want to thank Prof. Luc Martens, who accepted being co-examiner of this thesis and consequently performed a thorough review of the script.

My deepest thanks of course go to my friends and colleagues within the IT’IS/SPEAG structure, with whom I do not just spend most of my time but who have provided me with such great support, ideas, (sometimes loud) discussions and mostly funny days.

I will start here with the SEMCAD development team, which was founded at the beginning of this thesis in 1998 and which initially had the goal of producing a CAD based tool as an input to the MINAST EMSIM FDTD kernel, redeeming its users to create spheres with the *InitMediaCube* command. I want to thank Jürg Fröhlich for standing by with his wide and not just EM related knowledge, for keeping company during so many late-night VAW sessions by “cooking” or discussing in his amazingly literate way and finally for all the review work he performed. Thanks go to Andreas Christ who closely accompanied me through all these years, not just by establishing ourselves in the hard-fought FDTD community but also by pulling me back from deep research thoughts to reality by his sometimes scary *Neei-iiin!* screams. Deep gratitude goes to Hans-Ueli Gerber, who will actually always remain the “father” of SEMCAD, not just for being a *brilliant guy* but for supporting me in many coding-related ways, allowing a tiny insight into his experienced and elegant world of programming. Many thanks are addressed to Harald Songoro, who provided various support for coding and discussions which enriched the VAW scene with his charming and sometimes *direct* franco-canadian way, as well as Emilio Cherubini, the “OpenGL God”, who conjured the most amazing 3-D graphics on the screen within just a few minutes.

At this time I want to acknowledge the financial support of the Commission for Technology and Innovation (KTI) SEMCAD++ project which enabled great enhancement of the SEMCAD platform as well as the carrying out of this PhD.

Spatially moving my acknowledgements to Zeughausstrasse 43, location

of the IT'IS and SPEAG laboratories, I address my deepest thanks to all these powerful and fortunately increasing number of ladies within the team. In the first place addressing the queens of the lab: Katja Poković intensively tried to introduce me to the mysterious world of near-field measurements and the DASY system and moreover, spiritually sensed the right time to move towards Safari Bar and reflect on the passed week; Neviana Nikoloski performed substantial efforts in providing the large amount of experimental data which is included in this thesis – thanks so much. An immense volume of work is also done every day by the most effective IT'IS/SPEAG administrative support team. My sincere gratitude goes to Jacqueline Pieper, our “good spirit”, who finally brought some order into the not always properly structured affairs of the team, and moreover to Michelle Stubbs, for all the proofreading she did with respect to publications and this entire thesis. Many thanks and kisses for this. At this point I want to acknowledge Benedict DeSilva, for all the careful proofreading he performed during these years, furthermore all the administrative efforts carried out by Moni Lewis and Sibyl Akrong. Deep thanks also go to Jonathan Gubler and Thomas Schwitter who were always up-to-date with respect to the latest Mac rumors and did not just provide excellent Mac support but accompanied me in so many situations related to the generation of graphics and movies.

Major gratefulness must also be addressed to my PhD student colleagues: Juergen “Dr. J” Schuderer for heavily testing out implemented algorithms and SEMCAD in general, as well as Sven Ebert for spending an intensive time preparing our valuable GSM script. Rainer Mertens invested extensive efforts in the creation of the numerical SAM phantom model, and Walter Oesch greatly strengthened the appearance of the steadily growing “Bernese clan”.

My special thanks also go to the most valuable former SPEAG engineering and programming cracks: Oliver Egger for his coding support and the many night-life events he passionately organized, and Thomas Schmid for all the discussions we had during the good old IFH times, enriching our engineering attempts by his ingeniously intuitive problem solving.

Remembering the IFH times, I certainly have to sincerely thank Michael Burkhardt for inspiring me for FDTD and numerical simulations in such an intense manner during my semester and diploma work. Frank Schönborn greatly contributed toward enrichment of the entertainment in room G97. In addition, Ray Ballisti and Pascal Leuchtman provided outstanding support regarding UNIX system survival and EM related problems, respectively. Many thanks go to the “Austrian clan”, namely Wolfgang Kainz and Michael Frauscher for benchmarking SEMCAD and providing me with ideas for novel

features.

Very special thanks are also addressed to the academic guests which visited us. I would like to particularly mention Theodoros Samaras who, in his greek and *sweet-tempered* manner, inspired me within many distinguished discussions. Very much gratitude is mentioned with respect to Roger Tay, who greatly supported me in achieving the excellent outcome of chapter 8 and furthermore, benchmarked various SEMCAD algorithms.

To all the people I met during my Asia trips, namely Matsuo Kazuhiko, Young-Bae Song, Prof. Masao Taki, Dr. So-ichi Watanabe and Prof. Ihn-S. Kim, I express a lot of gratitude for having taken care of me with such generous hospitality, moreover enabling wide scientific information exchange, even on the topic of FDTD subgridding. In addition, I would like to address acknowledgements to Louis Slesin for always providing me with the latest BioEM rumors and providing entertaining discussions during last year's trips.

The intensive and close cooperation with our industry partners, namely with Ericsson Radio Systems AB, thereby addressing Martin Siegbahn, Dulce Altabella and Marc Douglas, resulted in a large number of inspiring scientific correspondence, leading to major improvements and extensions in the SEMCAD platform. Thanks a lot for your support.

At this time I would like to particularly amplify the gratitude I feel for the warm welcome and the smooth integration into the IIS environment which our entire group experienced during the turbulent times in the years 1999 and 2000. Sincere thanks go to all the amazingly professional members of the supporting and administrative team, namely Doelf Aemmer, Norbert Felber, Christine Haller, Margit Bocksberger, Bruno Fischer, Hansjörg Gisler and Hanspeter Mathys who all assisted me in many ways. A lot of acknowledgements also go to the IIS/ISG computer support, addressing Christoph Wicky, Fritz Zaucker as well as Tobias and Manuel Oetiker, who provided essential efforts for building up and maintaining the IT'IS computational infrastructure. Furthermore, thanks are expressed to FDTD and ISE related people such as Lars Bomholt, Peter Regli, Christian Schuster and Andreas Witzig for the smooth EMLAB - SEMCAD collaboration which we experienced during these years.

Many thanks must also be addressed to all my friends who often attempted and even managed to tear me out of the research environment in order to confront me with the *real life* out there, just mentioning some of you: Boris, Marc and the whole H7 gang; Mülli, Carlitos, Mäsi and the Mädels; Rodge, Ile & Nadia as well as my sister Sabine and my godson Alain. Folks, I think I'm back now !

In addition, I would like to thank Guiseppe Cimbali, Francesco Illy, Steve Jobs as well as Led Zeppelin, who all together made many of the late-night experiences at VAW easier to bear.

To three very special people in my life I would like to express my sincerest and deepest acknowledgements. Firstly to my parents who, in addition to supporting me in many ways, enabled my studies of electrical engineering. Last but not least I address the woman of all my love, dedicating her this thesis. Tabea, I thank you with all my heart for your widest support and deeply apologize for all the nights and weekends I considered spending time on this work to be more important than being with you.

Part I
Introduction

Seite Leer /
Blank leaf

Chapter 1

Motivation and Objectives

Recent decades have shown tremendous growth within the sector of mobile telecommunications equipment (MTE). Consumer demands for excellent product quality combined with low pricing have resulted in rigorous competition which heavily reduces product life cycles and hence the device development cycles. A definite trend is emerging within the continuous expansion of MTE applications toward *pervasive computing*, i.e., whole environments saturated with computing and wireless communication as well as in/on-body-mounted electro-medical devices. Recently introduced requirements, such as mandatory safety guidelines defined by international regulatory agencies are being followed by increasing public concern about possible adverse health effects from radio-frequency (RF) exposure.

RF engineers are therefore challenged to produce more and more efficient devices, revealing a clear demand for new analysis and optimization tools. As a complement to experimental instrumentation, the use of technical computer aided design (TCAD) has gained increasing interest, mainly due to rapidly increasing computational power. Particularly the Finite-Difference Time-Domain (FDTD) technique has gained high popularity for the simulation of electromagnetic (EM) problems, due to its straightforward explicit approach and the ability to compute largely non-homogeneous environments. However, applications to real-world engineering needs are often restrained by limited FDTD grid resolution and poorly implemented graphical user interfaces. Furthermore, most of the present local grid refinement algorithms have suffered from major restraints with respect to general applicability and robustness.

Right at the beginning of this thesis in 1998 the outcome of the EM-SIM project within the MINAST Swiss Priority Program merged into two awakening commercial EM simulation products, EMLAB and SEMCAD. The level of FDTD model complexity was already rather enhanced at that time with respect to non-homogeneous biological bodies; however, applied antenna configurations consisted mainly of simple structures like monopoles, PEC boxes or crudely modeled helices. Furthermore, biological and transmitter structures were only available in a voxel-based format, which clearly called for a 3-D CAD based model design environment combined with automated grid generation supporting enhanced FDTD modeling capabilities.

The objectives of this thesis were the development and analysis of novel generally applicable and robust FDTD local refinement techniques and their integration into the continuously developed 3-D TCAD environment SEMCAD. The investigations to achieve these demands consisted of the following parts:

- Analysis of the FDTD method itself as well as investigating the method inherent errors with respect to spatial resolution. This included a major review of studies reporting on staircasing, i.e., focusing on the influence of different simulation parameters on local and global errors.
- Provision of a review of existing methods for local grid refinement in the FDTD method based on the latest literature concentrating on schemes related to issues addressed within this thesis, namely subcell and subgridding techniques.
- Development of novel FDTD local grid refinement algorithms with strongly improved behavior and extended capabilities than existing ones, e.g., reduction of stability problems, enhanced accuracy and robustness as well as generalized applicability and adaptation to three dimensions.
- Rigorous analysis and benchmarking of the novel algorithms against straightforward FDTD modeling and existing approaches with respect to accuracy, stability considerations, efficiency and applicability. Moreover the methods were benchmarked against numerous examples providing measured data using the latest experimental tools.
- Major participation in the implementation of the EM simulation environment SEMCAD within the framework of the KTI funded project SEMCAD++. The deadlines defined by the project were adhered in

order to provide a rigorous EM simulation platform as the basis for all conducted applications within this thesis.

- Integration of the novel methods into the SEMCAD FDTD kernel. Moreover, the schemes were smoothly embedded into and combined with the automated grid and mesh generation structure of the code to enable its unrestricted usage. Even though enormously time intensive, the implementation and code generation part was only briefly outlined.
- Characterization of the developed algorithms' performance by application to various electromagnetic problems and studies in the field of mobile communications and antenna analysis. In addition to common antenna examples, the novel techniques enabled the modeling of complex real-world transmitter systems.
- Analysis of the possible influence of geometrical detail intensity on the behavior of FDTD simulation by application of the novel techniques. This extended the research on staircasing errors to general recommendations for FDTD modeling with an appropriate spatial resolution.
- Within the epilogue at the end of this thesis all achievements as well as open issues were summarized. Furthermore, ongoing/followed projects are discussed and possible future applications/visions of the developed enhanced FDTD modeling techniques are outlined.

Chapter 2

The Finite-Difference Time-Domain Technique

Abstract In this chapter the numerical scheme which underlies the algorithms developed within this thesis is outlined, whereby the basic theoretical background needed in the following chapters is examined and discussed. In addition, a concentrated specification of the most appropriate references which are related to the method is performed. Furthermore, the FDTD based simulation platform SEMCAD, the implementation of which is strongly related to this thesis, is briefly outlined.

2.1 The FDTD Method Applied to Electromagnetics

2.1.1 Introduction

The Finite-Difference Time-Domain (FDTD) method is based on a spatial and temporal discretization of Maxwell's equations, commonly within a rectangular cartesian grid originally proposed by Yee in 1966 [1]. Within the last two decades it gained rapidly increasing interest, mainly in electromagnetics (EM), for the simulation of complex and largely inhomogeneous structures due to its straightforward and explicit approach, resulting in various books providing theoretical and application oriented insights [2, 3, 4, 5, 6]. As depicted in figure 2.1, mainly in the late 90s but still today a huge number of

studies related to FDTD have been published (1999-2001: counts not complete), leading to about 4500 scientific papers total [7]. The exponentially increasing availability of computational power has made it the most popular numerical method for a broad range of applications and has resulted in the release of several public [8, 9, 10] and commercial FDTD based simulation platforms [11] - [22].

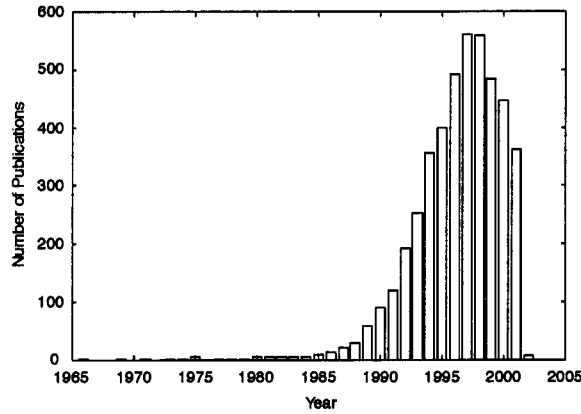


Figure 2.1: Number of FDTD related publications per year from 1965 up to today (source: [7], 1999-2001: counts not complete).

2.1.2 Discretizing Maxwell's Equations

By assuming a spatial environment without any electric or magnetic sources, the relations

$$\vec{B} = \mu \vec{H}, \quad \vec{D} = \epsilon \vec{E}, \quad \vec{J}_m = \rho' \vec{H}, \quad \vec{J}_e = \sigma \vec{E} \quad (2.1)$$

enable a definition of the time dependent Maxwell's curl equations in differential form as follows:

$$\frac{\partial \vec{H}}{\partial t} = -\frac{1}{\mu} \nabla \times \vec{E} - \frac{\rho'}{\mu} \vec{H} \quad (2.2)$$

$$\frac{\partial \vec{E}}{\partial t} = \frac{1}{\epsilon} \nabla \times \vec{H} - \frac{\sigma}{\epsilon} \vec{E} \quad (2.3)$$

where \vec{E} and \vec{H} indicate the electric and the magnetic field vectors, respectively. The electric permittivity and magnetic susceptibility are specified by

ϵ and μ , respectively, while σ defines the electric conductivity. The expressions \vec{J}_e and \vec{J}_m are electric and an equivalent magnetic current which define dielectric losses. ρ' indicates the corresponding magnetic conductivity.

The algorithm proposed by Yee is based on a description of the temporarily coupled system as described in equations 2.2 and 2.3 on the basis of a finite central difference approximation. Figure 2.2 depicts the position of the electric (yellow) and magnetic (green) field components for each primary and secondary Yee cell, respectively, allocated within the staggered cartesian grid. The fields are located in a way where each \vec{E} component is surrounded by four \vec{H} components and vice versa, which leads to a spatially coupled system of field circulations corresponding to the law of Faraday and Ampère. Each three E- and H-field components are assigned to a node i, j, k within the three dimensional (3-D) grid.

The discretization in time is performed in a leap frog manner by application of a temporally shifted updating for E- and H-field components as shown in figure 2.3. Thereby the electric components are calculated at incrementing time $t = (n+l)\Delta t$, ($l = 0, 1, 2, \dots$) with respect to a globally defined timestep Δt . The computation of the magnetic components is performed at $t = (n+l + \frac{1}{2})\Delta t$, ($l = 0, 1, 2, \dots$), i.e., shifted by half a timestep.

The original FDTD formulation proposed by Yee was intended for homogeneous, isotropic and lossless media on a uniform grid by application of a cartesian coordinate system. Achieving 2nd order accuracy using a 2nd order finite differences approximation for the differential equations 2.2 and 2.3 leads to

$$\frac{\partial u}{\partial x}(i, j, k, n) = \frac{u_{i+\frac{1}{2},j,k}^n - u_{i-\frac{1}{2},j,k}^n}{\Delta x} + O[(\Delta x)^2] \quad (2.4)$$

$$\frac{\partial u}{\partial t}(i, j, k, n) = \frac{u_{i,j,k}^{n+\frac{1}{2}} - u_{i,j,k}^{n-\frac{1}{2}}}{\Delta t} + O[(\Delta t)^2] \quad (2.5)$$

for time and space as shown for the x direction. The indices i, j, k indicate integer values specifying a certain node in the spatial grid (figure 2.2) and u^n any temporal dependent function at the time $n\Delta t$, i.e., the electric or magnetic field. $O[(\Delta x)^2]$ and $O[(\Delta t)^2]$ indicate the spatial and temporal second order error terms.

The x component of the electric field within equation 2.3 is formulated by application of central differences as follows:

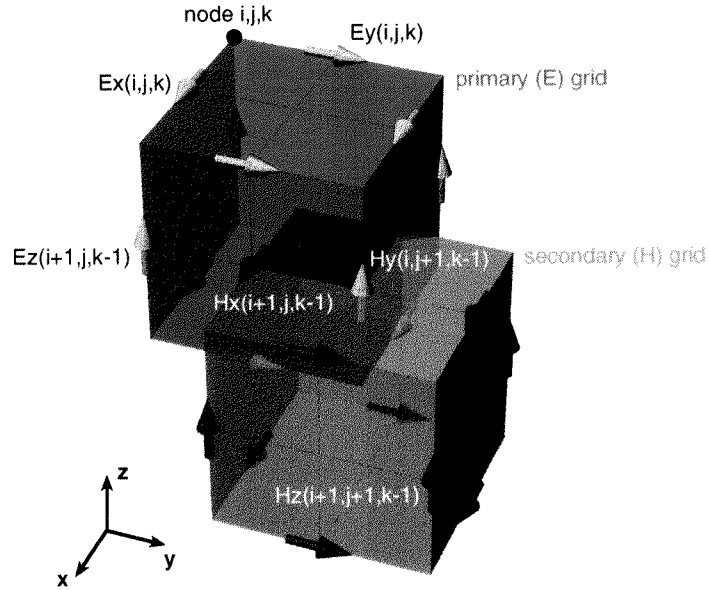


Figure 2.2: Primary and secondary cell within Yee grid representing E- and H-field components in the discretized space. Each node i,j,k within the grid represents three electric and magnetic field components located around a volume element.

$$\frac{E_x|_{i,j,k}^{n+1} - E_x|_{i,j,k}^n}{\Delta t} = \frac{1}{\epsilon_{i,j,k}} \left(\frac{H_z|_{i,j+\frac{1}{2},k}^{n+\frac{1}{2}} - H_z|_{i,j-\frac{1}{2},k}^{n+\frac{1}{2}}}{\Delta y} - \frac{H_y|_{i,j,k+\frac{1}{2}}^{n+\frac{1}{2}} - H_y|_{i,j,k-\frac{1}{2}}^{n+\frac{1}{2}}}{\Delta z} - \sigma_{i,j,k} E_x|_{i,j,k}^{n+\frac{1}{2}} \right) \quad (2.6)$$

By application of the semi-implicit approximation where it is assumed that

$$E_x|_{i,j,k}^{n+\frac{1}{2}} = \frac{E_x|_{i,j,k}^{n+1} - E_x|_{i,j,k}^n}{2} \quad (2.7)$$

the algorithm can be expressed in a fully explicit form, i.e., equation 2.6 is written as

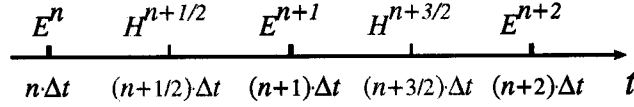


Figure 2.3: Leap-frog scheme: temporal updating of electric and magnetic field components using half a time step temporal separation.

$$\begin{aligned}
 E_x|_{i,j,k}^{n+1} = & \left(\frac{1 - \frac{\Delta t \sigma_{i,j,k}}{2\epsilon_{i,j,k}}}{1 + \frac{\Delta t \sigma_{i,j,k}}{2\epsilon_{i,j,k}}} \right) E_x|_{i,j,k}^n + \\
 & \left(\frac{\frac{\Delta t}{\epsilon_{i,j,k}}}{1 + \frac{\Delta t \sigma_{i,j,k}}{2\epsilon_{i,j,k}}} \right) \left(\frac{H_z|_{i,j+\frac{1}{2},k}^{n+\frac{1}{2}} - H_z|_{i,j-\frac{1}{2},k}^{n+\frac{1}{2}}}{\Delta y} - \right. \\
 & \left. \frac{H_y|_{i,j,k+\frac{1}{2}}^{n+\frac{1}{2}} - H_y|_{i,j,k-\frac{1}{2}}^{n+\frac{1}{2}}}{\Delta z} \right) \quad (2.8)
 \end{aligned}$$

A detailed description of the entire updating equations for electric and magnetic field components is given in [3]. The formulation based on Maxwell's equations in integral form, i.e., the law of Faraday and Ampère, is discussed within chapter 5. In time domain, the spatial and temporal updating scheme of the associated Finite-Integration Technique (FIT) [23] is of the same nature as the FDTD method, including stability and dispersion properties [3].

2.1.3 Stability

In order to guarantee numerical stability for the common FDTD approach, the upper limit of the timestep Δt must be bounded by a criterion which restricts an update cycle's EM fields propagation from cell to cell being faster than allowed by the phase velocity $v_p = 1/\sqrt{\mu\epsilon}$ within any material (ϵ, μ). Initially reported in [24], a stability analysis based on eigenmodes of the 3-D space was performed, while more recent publications apply a combination of alternative methods [25]. The corresponding Courant-Friedrichs-Lewy criterion for the general Yee grid defines stability as

$$\Delta t \leq \min \left\{ \frac{1}{v_p \cdot \sqrt{\frac{1}{(\Delta x)^2} + \frac{1}{(\Delta y)^2} + \frac{1}{(\Delta z)^2}}} \right\} \quad (2.9)$$

where $\Delta x, \Delta y$ and Δz indicate the spatial cartesian grid increments. The minimum ($\min\{\zeta\}$) condition must include all cells within the entire computational domain.

Although the common Yee method for non-dispersive, isotropic and lossless media is proven to be conditionally stable for algorithms introducing conformal modeling and special treatment of grid interfaces as performed in subcell and subgridding schemes, respectively, the derived stability criterion is no longer valid [26], [27], [28]. In order to avoid numerical instabilities in such modified schemes, the timestep Δt derived by the CFL criterion has to be further reduced. The algorithms developed in the scope of this thesis address stability issues within chapters 5 and 6, in sections 5.2.4 and 6.3.2.

2.1.4 Modeling of Boundaries

Contrary to boundary methods, the FDTD scheme requires the application of Absorbing Boundaries (AB) in order to spatially limit the computational domain. The common differential equations do not allow the determination of the tangential field components located at the domain boundaries, since this would require field information from outside the existing FDTD grid. A number of methods, so called Absorbing Boundary Conditions (ABC), have been proposed to reduce reflections from the computational boundaries, of which a very early formulation is found in [29]. In general, ABCs are essentially based on two principles: conditions imitating an absorbing material or conditions based on plane wave solutions to the wave equation. Within these methods the tangential electric field components have to be calculated in a way absorbing the incident wave as effectively as possible.

ABC Based on Wave Equations: One-Way Wave Equations

A common boundary operator of the second type was proposed in [30] and applied to the FDTD approach by Mur [31]. This boundary condition allows attenuation for waves propagating in just one direction. The method is commonly applied to plane wave excitations for a perpendicular angle of incidence with respect to the domain boundary. The tangential E-field components \vec{E}_{tan} located at the most outer cell layer must satisfy the one dimensional (1-D) wave equation in the normal direction, e.g., formulated in first order approximation and for the cartesian y direction:

$$\left(\frac{\partial}{\partial y} - \frac{1}{v_p} \frac{\partial}{\partial t} \right) \vec{E}_{tan} = 0 \quad (2.10)$$

By application of components from within the computational domain, equation 2.10 can be discretized and expressed in a finite differential equation of the form

$$E_0^{n+1} = E_1^n + \frac{v\Delta t - \Delta y}{v\Delta t + \Delta y} (E_1^{n+1} - E_0^n) \quad (2.11)$$

where E_0 is the tangential E-field component located at the domain truncation and E_1 indicates the colinear one shifted by Δy into the FDTD grid. An extension to 2nd order, which additionally allows the partial absorption of waves for a diagonal angle of incidence, is based on the same principle but of increased complexity for derivation. A three-dimensional ABC scheme allowing appropriate attenuation for EM plane wave excitation in arbitrary directions was proposed in [32].

ABC Based on Absorbing Media - The PML Approach

Different from the one-way wave equations, Berenger proposes in [33] a novel type of ABC leading to highly reduced reflections down to -80 dB in a broadband frequency range [3], [34]. The perfectly matched layer (PML) approach is based on introducing an artificial multi-layered highly absorbing medium located at the computational domain truncation. By matching both electric and magnetic conductivity (σ_e, σ_m) of the different layers a minimum reflection can be forced which consequently absorbs an incident wave within the multi-layered medium. The wave impedance for an artificial lossy dielectric material

$$\nu = \sqrt{\frac{\mu - j\frac{\sigma_m}{\omega}}{\epsilon - j\frac{\sigma_e}{\omega}}} \quad (2.12)$$

reduces to $\sqrt{\mu/\epsilon}$ and $\sqrt{\sigma_m/\sigma_e}$ by assumption of no losses and high losses, respectively. Choosing $\mu/\epsilon = \sigma_m/\sigma_e$ leads to minimum reflection at the intersection connecting both media. The original approach [33] applies a splitting of each field component into two sub-components to which the individually matched losses are assigned. The method's common application to open-domain dielectric non-lossy structures was extended to enable lossy material traversing the domain truncation in [35].

2.1.5 Implementation / Integration into Simulation Environments

All research work which has been performed in the framework of this thesis was conducted in parallel with the development of the FDTD based state-of-the-art EM simulation platform SEMCAD. Its application area is wide, targeting antenna design and optimization, EMC, EMI and dosimetry. Initially developed within the Swiss Priority Program for Micro and Nano System Technology (MINAST), it is currently being commercialized by Schmid & Partner Engineering AG (SPEAG). Continuous improvement and extension of the platform is performed within the scope of the SEMCAD++ project by R&D teams within a Swiss Consortium composed of the Institute for Integrated Systems (IIS) of the Swiss Federal Institute of Technology Zurich (ETHZ), the Foundation for Research on Information Technologies in Society (IT'IS), SPEAG and the Integrated Systems Engineering (ISE) AG and supported by the Commission for Technology and Innovation (KTI, Switzerland).

This thesis' contributions with respect to code generation and implementation into the SEMCAD platform can be briefly summarized as follows:

- Implementation of the subcell scheme into EMLAB code: the subcell algorithm presented in chapter 5 is integrated, enabling the generation of grid non-conformally aligned PEC structures via parameter input. The implementation is performed without affecting the existing FDTD routines, i.e., the updating of just the PEC nearby components is treated specially. A number of routines provide the extraction of EM field data within arbitrarily oriented sensor objects. (Transfer to SEMCAD platform within SEMCAD++ project)
- Implementation of the rotated source model into EMLAB code: the non-conformally aligned source model which is described in chapter 5, section 5.2.3 is activated by specification of a grid node for its spatial location. A hard-source provides the full set of available excitation types to be applied. (Transfer to SEMCAD platform within SEMCAD++ project)
- Implementation of the subgridding scheme: the novel subgrid algorithm presented in chapter 6 is integrated into the SEMCAD environment by implementation of a main class handling the interface between two connected grids (upper grid - subgrid). This class itself makes use of three subclasses which provide support for interpolation (3-D cubic

splines), data handling (organization of subgrid surface components) and data storage (of intermediate field values used in temporal interpolation). The implementation is done in a very modular way, enabling easy parameter changing (e.g., for varying the type of spatial interpolation scheme used).

- Extension of the subgrid integration to enable nesting: the subgrid main class was consequently extended in order to allow an arbitrary nesting of subgrids in a sequential and/or parallel manner. This is performed in general by defining parent and child grids for each subgrid (interface) of which the objects are processed during each update cycle. The implementation was thereby carried out in a way which leaves the existing FDTD grid objects untouched, i.e., the subgrid feature is set as a module on top of the common grid classes.
- Adaptation of the grid generator to embed the subgridding scheme: the existing semi-automatic generator for homogeneous and non-homogeneous grids was extended to allow a straightforward integration of the subgrids. The specific grid / subgrid objects are thereby handled recursively. Major attention was given to allow a combined application of subgrids and graded mesh in order to provide the most effective and general application. The grid generation user interface was extended to enable free positioning of the subgrids. Furthermore, all grids are graphically displayed within the GUI.
- Adaptation of the material assignment: in addition to the grid generation, the assignment of material to the different Yee cells had to be distinguished for and performed within the different grids. The 3-D ACIS solid objects are thereby first converted into triangulated structures and consequently processed using a 3 · 2-D analysis of the intersection points with the FDTD grid. Moreover, the material assignment of all objects located within different grids was graphically visualized within the GUI using 3-D OpenGL (OGL) routines.
- Adaptation of the source / field sensor handling: all sources as well as field sensors recording the EM fields (Yee components) at previously defined spatial locations had to be adapted to the new multi-grid concept. Depending on the location of the source/sensor in a specific grid, the Yee components from within this grid had to be recorded and processed (application of corresponding timestep, data extraction at postprocessor level).

- Generation of the postprocessing (PP) concept: not directly related to the novel algorithms, a global postprocessing concept was developed within the SEMCAD(++) project. It consists of a main class handling and keeping track of all result data and the corresponding viewers/charts. Via a token system, this main class manages the extraction of data from the HDF files, its processing with respect to the user input, the passing of processed data to a specific viewer as well as the data and viewer's lifetime.
- Implementation of the postprocessing engine: based on the action of the postprocessing main class which is determined by the user input, the time-domain data recorded during the simulation is extracted from the Hierarchical Data Format (HDF) files and processed (specific fields are assessed from the pure Yee E- and H-field components). This data is consequently passed to a chosen viewer/chart type.
- Implementation of the chart/viewer entities: an entire set of 1-D, 2-D and 3-D viewers and charts was integrated into the SEMCAD environment. For standalone floating charts like XY, Smith and polar charts as well as contour and surface viewers, a third party product [36] was applied for the visualization. In order to directly overlay EM field data into the GUI (scalar field, 3-D vector representation, 3-D far-field and 3-D field overlay on solid object's surfaces), i.e., in addition to the solids, a set of OGL based display routines have been implemented. All viewers were equipped with various user selectable customization possibilities.

The highly user-friendly solid modeling environment is based on the well approved ACIS modeling toolkit, allowing the generation of complex 3-D objects as well as the import of whole CAD datasets in various formats. Its CAD environment enables a free positioning, tilting and moving of objects without any restrictions to a predefined resolution or grid configuration. Fully automated generation of non-homogeneous meshes, robust subgrids as well as fast material assignment is supported. In addition, a large database of non-homogeneous human and animal phantoms as well as standard phantoms widens the application range to dosimetry related investigations.

The postprocessing engine enables the extraction of any time and frequency domain data from the near- and far-fields (U, I, Z, SWR, P, S-parameters; E, H, D, B, S, J; SAR peak and averaged; 2-D and 3-D far-field) and its visualization within a variety of appropriate viewers and charts (XY,

polar plot and Smith chart; 2-D contour, surface viewer, overlay in GUI; 3-D overlay on solid objects). In addition, the combined platforms SEMCAD and DASY4 allow the direct comparison of numerical and experimental data within the same postprocessing environment.

The kernel providing 3-D full wave simulation and engines for thermal and quasi-static computations incorporates all state-of-the-art FDTD related features, such as the latest boundary conditions (1st and 2nd order Mur, Higdon operator up to 4th order, PML, electric, magnetic) as well as various source/excitation types (hard-, voltage- and added-source; sinusoidal and Gaussian-sine signals). In addition to the novel algorithms presented within this thesis, a number of algorithms were uniquely implemented into SEMCAD enabling improved representation of dielectric planar material transitions and enhanced precision through phase velocity correction for non-homogeneous meshes.

References

- [1] K.S. Yee, "Numerical solution of initial boundary value problems involving Maxwell's equations in isotropic media", *IEEE Transactions on Antennas and Propagation*, vol. 14, pp. 302–307, 1966.
- [2] K.S. Kunz and R.J. Luebbers, *The Finite Difference Time Domain Method for Electromagnetics*, CRC Press, Boca Raton, FL, 1993.
- [3] A. Taflov, *Computational Electrodynamics - The Finite Difference Time Domain Method*, Artech House, Norwood, MA, 1995.
- [4] A. Taflov, *Advances in Computational Electromagnetics: The Finite Difference Time Domain Method*, Artech House, Norwood, MA, 1998.
- [5] D.M. Sullivan, *Electromagnetic Simulation Using The FDTD Method*, IEEE Press, Piscataway, NJ 00885-1331, 2000.
- [6] W. Sui, *Time-Domain Computer Analysis of Nonlinear Hybrid Systems*, CRC Press, Boca Raton, FL, 2001.
- [7] J. B. Schneider and K. Shlager, "Statistics pertaining to FDTD.org", www.fDTD.org, January, 2002.
- [8] Carsten Aulbert, Golm, Germany, "Geo-Radar FDTD", www.welcomes-you.com/radarfDTD.
- [9] R. Luebbers and K. Kunz, Pennsylvania State University, Pennsylvania, USA, "Penn State FDTD Code", [ftp.emclab.umr.edu](ftp://emclab.umr.edu).
- [10] Borg Group, University of Minnesota, Minnesota, USA, "ToyFDTD", www.borg.umn.edu/toyfDTD.
- [11] Computer Simulation Technology (CST), Darmstadt, Germany, "MAFIA / Microwave Studio", www.cst.de.
- [12] Electro Magnetic Applications (EMA), Lakewood, USA, "EMA3D", www.sni.net/emaden.
- [13] EMS-Plus, Durham, NC, USA, "EZ-FDTD", www.ems-plus.com.
- [14] IMST GmbH, Kamp-Lintfort, Germany, "Empire", imst254.imst.de/microw/products/empire.

- [15] Integrated Systems Engineering (ISE) AG, Zurich, Switzerland, "*EM-LAB*", www.ise.ch.
- [16] QWED, Warsaw, Poland, "*QuickWave-3D*", www.qwed.com.pl.
- [17] REMCOM Inc., State College, PA, USA, "*XFDTD*", www.remcom.com.
- [18] Schmid & Partner Engineering AG (SPEAG), Zurich, Switzerland, "*SEMCAD*", www.semcad.com.
- [19] Sigrity Inc., Binghamton, NY, USA, "*SPEED97*", www.sigrity.com.
- [20] Vector Fields Inc., Aurora, IL, USA, "*CONCERTO*", www.vectorfields.com.
- [21] Virtual Science, West Sussex, UK, "*Celia*", www.virtual-science.co.uk.
- [22] Zeland Software, Fremont, CA, USA, "*Fidelity*", www.zeland.com.
- [23] T. Weiland, "Maxwell's grid equations", *Frequenz*, vol. 44, no. 1, pp. 9–16, 1990.
- [24] A. Taflove and M.E. Brodwin, "Numerical solution of steady-state electromagnetic scattering problems using the time-dependent Maxwell's equations", *IEEE Transactions on Microwave Theory and Techniques*, vol. 23, pp. 623–630, Aug. 1975.
- [25] J.A. Pereda, L.A. Vielva, A. Vegas, and A. Prieto, "Analyzing the stability of the FDTD technique by combining the von Neumann method with the Routh-Hurwitz criterion", *IEEE Transactions on Microwave Theory and Techniques*, vol. 49, no. 2, pp. 377–381, Feb. 2001.
- [26] N.K.Madsen, "Divergence preserving discrete surface integral methods for maxwell's curl equations using nonorthogonal unstructured grids", *Tech. Rep. UCRL-JC-109787, Lawrence Livermore National Laboratory*, 1992.
- [27] M. Okoniewski, J. Anderson, J. Mrozowski, and S.S. Stuchly, "Arbitrarily located metal surfaces in FDTD technique", *Progress in Electromagnetics Research Symposium, Seattle, WA*, 1995.
- [28] P. Monk, "Sub-Gridding FDTD schemes", *ACES Journal*, vol. 11, no. 1, pp. 37–46, Mar. 1996.

- [29] D.E. Merewether, "Transient currents induced on a metallic body of revolution by an electromagnetic pulse", *IEEE Transactions on Electromagnetic Compatibility*, vol. 13, no. 2, pp. 41–44, May 1971.
- [30] B. Engquist and A. Majda, "Radiation boundary conditions for acoustic and elastic wave calculations", *Communications on Pure and Applied Mathematics*, vol. 32, pp. 313–375, 1977.
- [31] G. Mur, "Absorbing boundary conditions for the finite-difference approximation of the time-domain electromagnetic-field equations", *IEEE Transactions on Electromagnetic Compatibility*, vol. 23, no. 4, pp. 377–382, Nov. 1981.
- [32] R.L. Higdon, "Absorbing boundary conditions for difference approximation to the multi-dimensional wave equation", *Mathematics of Computation*, vol. 47, no. 176, pp. 437–459, Oct. 1986.
- [33] J.P. Berenger, "A perfectly matched layer for the absorption of electromagnetic waves", *Journal of Computational Physics*, Oct. 1994.
- [34] Z. Wu and J. Fang, "Numerical implementation and performance of perfectly matched layer boundary condition for waveguide structure", *IEEE Transactions on Microwave Theory and Techniques*, vol. 43, no. 12, pp. 2676–2683, Dec. 1995.
- [35] J. Fang and Z. Wu, "Generalized perfectly matched layer - an extension of berenger's perfectly matched layer boundary condition", *IEEE Microwave and Guided Wave Letters*, vol. 5, no. 12, pp. 451–453, Dec. 1995.
- [36] Gigasoft Inc., Keller, TX, USA, "Pro Essentials", www.gigasoft.com.

Chapter 3

Limitations of the FDTD Scheme with Respect to Spatial Resolution

Abstract Within this chapter the FDTD method inherent errors with respect to spatial grid resolution are outlined on the basis of the most relevant experimental and theoretical investigations from the FDTD literature. Finally, general conclusions and recommendations with respect to staircasing are pointed out.

3.1 Numerical Errors Caused by Stair-Stepped Modeling Approximations

3.1.1 Introduction

Because of its simplicity and straight-forward approach, the FDTD method has certain restrictions, in particular with respect to spatial resolution. For the common scheme major drawbacks especially arise for PEC structures which are either grid non-conformally aligned or of very fine spatial detail and are therefore represented in a stair-stepped approximation (*staircasing*). An additional disadvantage is posed by the missing or highly difficult determination of the method's quantitative uncertainty which is defined by the sum of multiple error sources. All summarized error sources may have a highly case dependent influence on the uncertainty of the examined system

within FDTD. This thesis mainly addresses the topics indicated in *italics*, i.e., errors which are mainly related to a coupled spatial model / grid representation, collected as follows:

- *insufficient representation of the geometrical physical model*: major simplifications in significant geometrical details and neglecting important electromechanical parts (topic is discussed in chapters 6, 7 and 8)
- *inaccurate material assignment*: incorrect location of materials within the spatial grid, e.g., bypassing two closely arranged PEC structures (topic is discussed in chapter 8)
- improper application of material parameters: neglecting dependence on frequency, temperature, field strength and spatial orientation as well as the implication of incorrect material parameters (e.g., usage of parameters measured at low frequencies for high frequency applications)
- *errors in source/excitation modeling*: spatially improper positioning of the source model (e.g., source not properly connected to transmitter structures, asymmetric location), application of simplified or improper signal types in the time domain (topic is discussed in chapter 5)
- *staircasing (PEC, lossy dielectric materials)*: major simplifications due to insufficient spatial discretization within FDTD, excitation of non-physical EM components due to stair-stepped material representations (topic is discussed within this chapter and in chapters 5, 6, 7 and 8)
- phase velocity errors: numerical dispersion errors due to insufficient FDTD grid refinement in spatially widely extended areas as well as in non-homogeneous (graded) meshes
- reflections from boundaries: insufficient absorption of the incident EM wave by the applied ABC, incorrect placement too close to the transmitter/scatterer, application of an ABC unsuited for the type of EM excitation
- low accuracy in computational processing (machine accuracy / data types, data extraction): application of insufficiently high computational resolution for specific algorithms within the simulation process or at the postprocessing level (e.g., usage of single precision accuracy for numerical schemes which rely on double precision)

Whereas various investigations have been performed addressing general grid resolution related numerical dispersion errors in the cartesian FDTD mesh [1], [2] only a number of publications directly address errors caused by the stair-stepped representation of material boundaries which are discussed within this section.

3.1.2 Investigations Based on Numerical Experiments

Staircasing artifacts can be subdivided into different types as shown in figure 3.1. Whereas the numerical error caused by single voxels and holes (b, c) is of a locally highly restricted nature, to steps (a) and wide area staircasing (e) special attention was drawn, namely in [3] examining the EM energy absorption in lossy dielectric materials.

Investigations have been performed in 2-D for a single step consisting of homogeneous tissue comparing the Specific Absorption Rate (SAR) for different dielectric parameters, plane wave polarizations, frequencies and grid refinements. Major effects were found with respect to polarization and grid resolution (material parameters: $\epsilon_r = 42$, $\sigma = 0.85 \text{ S/m}$, $f = 900 \text{ MHz}$). Local errors at the edge step of up to 50% have been reported for TE polarization, showing minor effects for a variation of the FDTD spatial discretization from 0.5 mm to 2 mm. The error decreases for TH polarization to about 15% by application of the same configuration but shows a stronger dependence with respect to the grid resolution. No significant influence on the error in SAR was observed by changing material parameters (permittivity: 5 - 80, conductivity: 0.85 - 2 S/m) nor from using different frequencies between 900-1800 MHz.

In contrast to spatially restricted local errors due to single steps, [3] further investigated globally significant errors due to staircasing on the basis of a dielectric sphere (diameter = 200 mm, $\epsilon_r = 42$, $\sigma = 0.85$) exposed to a plane wave excitation at $f = 900 \text{ MHz}$. Different spatial discretizations (1 - 4 mm) were applied, and the results were compared to a semi-analytical solution obtained using the Generalized Multipole Technique [4]. For reasons of different focusing effects within the dielectric sphere, a spatially more extended error in SAR varies from 5 - 15% with respect to grid resolution. In addition, a 45° rotated dielectric cube of 200 mm³ dimension (grid step: 3.8 mm, material properties same as for sphere) was exposed to a plane wave for two polarizations at $f = 900 \text{ MHz}$ and compared to a conformally aligned reference solution. Errors in SAR of 4 - 10% result if the wave vector \vec{k} is in a 45° incidence with the cube surface, whereas good agreement is obtained for \vec{k} being at orthogonal incidence.

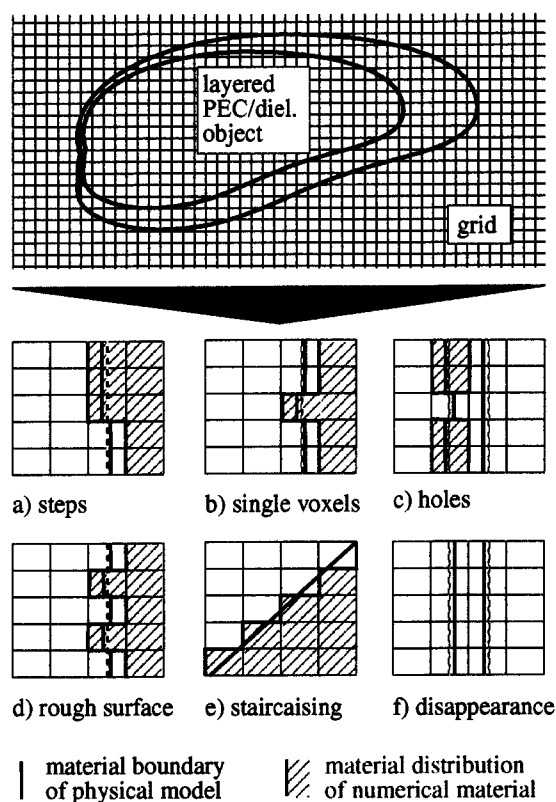


Figure 3.1: Distinction of staircasing artifacts for FDTD grid non-conformally aligned PEC or dielectric structures (source: [3]).

Experimental investigations on the far-field staircasing error for PEC structures are presented in [5] on the basis of a conducting strip and a circular cylinder. As a reference calculation, the conducting strip is first modeled FDTD grid conformally aligned as a single straight row of conducting cells (1 cell thickness) embedded in free space. A plane wave (TE polarization) illuminates the strip from below, propagating in a 5° angle of incidence. Consequently the setup was rotated by 5° leading to a stair-stepped strip line (every 12th cell normal to incident wave) and a plane wave excitation propagating conformally aligned with the grid. The staircasing error was then assessed via comparing the Radar Cross Section (RCS) of both examples using the technique described in [6]. Errors in the range of 1 dB

have been reported for resolutions of 100 cells per λ due to possible surface currents in the direction of the stripline thickness by the presence of staircasing. Furthermore, the cells oriented normal to the incident wave evoke short-wavelength (high-frequency) components in the scattered field. Strong deviations of 3 dB in the RCS compared to conformal modeling are obtained for a conducting cylinder (radius: 0.5 m, grid resolution: 20 mm) illuminated at 45° (TH polarization) by a plane wave at frequencies around 1 GHz.

The influence of the staircasing error on the near-field of a transverse electromagnetic (TEM) horn antenna was investigated in [7]. Except for a ringing effect in the tail area of the excited broadband pulse, no significant quantitative findings with respect to staircasing errors were reported. However, to achieve meaningful results, the FDTD grid must be chosen so that $\Delta s < \lambda/2$ for all significant frequencies in the excitation signal, where Δs indicates the diagonal length of the stairstep. For the applied 12:1 slope horn this yields in $\Delta s = \sqrt{(12\Delta x)^2 + (1\Delta x)^2}$ where Δx is the homogeneous grid step.

Investigations related to staircasing errors on resonant cavities for different dimensions and grid resolutions are presented in [8]. Errors in the range of 1-5 % with respect to the resonance frequency of the dominant mode have been reported for a spherical as well as for a cylindrical cavity, whereby coarse grid resolutions of about 10-20 cells per λ (at resonance frequency) were applied. A strong dependence of the error on the radius (spherical cavity) and on the spatial orientation (cylindrical cavity) are shown.

3.1.3 Investigations Based on Analytical Approaches

A rigorous analysis of staircasing errors is presented in [9] for a staggered air-PEC interface rotated by 45° with respect to the conformally aligned cartesian FDTD grid. A similar approach is presented in [10] but extends the analysis for 2-D air-PEC transitions to lossless dielectric materials. Due to the generality of this approach it is briefly outlined.

In order to analytically derive the staircasing errors at an air-dielectric interface, the setup in figure 3.2 is shown, applying a material transition boundary tilted by 45° . Both the reflection coefficient R at the transition and attenuation constant α for a surface wave supported by the staircased boundary are assessed. According to equations 2.4 and 2.5, the magnetic field at the location (l, m) can be expressed in discretized form as follows:

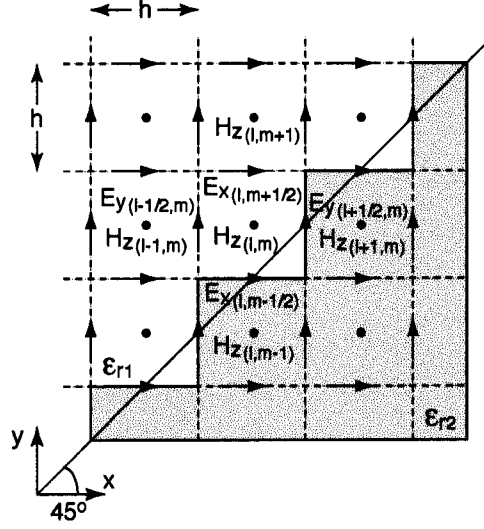


Figure 3.2: 2-D finite-difference grid for an air dielectric interface in the cartesian xy plane: the material transition boundary is tilted by 45° (source: [9]).

$$\frac{H_z|_{l,m}^{n+1} - H_z|_{l,m}^n}{\Delta t} = \frac{1}{\mu_0 h} \left(E_x|_{l,m+\frac{1}{2}}^{n+\frac{1}{2}} - E_x|_{l,m-\frac{1}{2}}^{n+\frac{1}{2}} + E_y|_{l-\frac{1}{2},m}^{n+\frac{1}{2}} - E_y|_{l+\frac{1}{2},m}^{n+\frac{1}{2}} \right) \quad (3.1)$$

where Δt indicates the timestep and h is the cell size corresponding to figure 3.2. The four E -field components which surround the H -field located at (l, m) are derived in a similar manner (just shown for E_y):

$$E_y|_{l-\frac{1}{2},m}^{n+\frac{1}{2}} = E_y|_{l-\frac{1}{2},m}^{n-\frac{1}{2}} - \frac{\Delta t}{\epsilon_0 h} (H_z|_{l,m}^n - H_z|_{l-1,m}^n) \quad (3.2)$$

$$E_y|_{l+\frac{1}{2},m}^{n+\frac{1}{2}} = E_y|_{l+\frac{1}{2},m}^{n-\frac{1}{2}} - \frac{\Delta t}{\epsilon_2 h} (H_z|_{l+1,m}^n - H_z|_{l,m}^n) \quad (3.3)$$

whereas equation 3.2 represents the electric field located in vacuum ($\epsilon_{r1} = 1$), equation 3.3 indicates the E -field within the dielectric ($\epsilon_2 = \epsilon_{r2}\epsilon_0$). Expressions for the E_x components can be derived in the same way and finally applied to substitute the E -field terms in equation 3.1

$$\begin{aligned}
\frac{\mu h^2}{(\Delta t)^2} (H_z|_{l,m}^{n+1} - 2H_z|_{l,m}^n + H_z|_{l,m}^{n-1}) = \\
\frac{1}{\epsilon_0} (H_z|_{l,m+1}^n - 2H_z|_{l,m}^n + H_z|_{l-1,m}^n) \\
+ \frac{1}{\epsilon_2} (H_z|_{l+1,m}^n - 2H_z|_{l,m}^n + H_z|_{l,m-1}^n) \quad (3.4)
\end{aligned}$$

Introducing expressions for the incident (*i*), reflected (*r*) and transmitted (*t*) magnetic fields for the air-dielectric interface rotated by 45° leads to

$$\begin{aligned}
H^i &= H_0 e^{-j\{k_x(lh) + k_y(mh) - \omega(n\Delta t)\}} \\
H^r &= RH_0 e^{-j\{k_y(lh) + k_x(mh) - \omega(n\Delta t)\}} \\
H^t &= TH_0 e^{-j\{k_{x2}(lh) + k_{y2}(mh) - \omega(n\Delta t)\}} \quad (3.5)
\end{aligned}$$

where the total field in vacuum is represented by the sum of H^i and H^r and k_{x2} as well as k_{y2} indicate the propagation constants within the dielectric material. They can be expressed in terms of the vacuum propagation constants by

$$k_{x2} = \frac{k_x + k_y}{2} + \sqrt{\frac{k_x^2}{2} - \left(\frac{k_x + k_y}{2}\right)^2} \quad (3.6)$$

$$k_{y2} = \frac{k_x + k_y}{2} + \sqrt{\frac{k_y^2}{2} - \left(\frac{k_x + k_y}{2}\right)^2} \quad (3.7)$$

where the propagation constant in the dielectric is represented by $k_2 = \omega\sqrt{\epsilon_r}\sqrt{\mu_0\epsilon_0}$. Investigating guided surface wave modes on the material interface the procedure proposed in [9] is applied for the 45° inclination which defines

$$k_x = \beta - j\alpha, \quad k_y = \beta + j\alpha \quad (3.8)$$

and assumes that $\alpha > 0$. Due to the continuity condition of the tangential magnetic field component at the material transition, the condition

$$k_{x2} + k_{y2} = k_x + k_y \quad (3.9)$$

is enforced for the wave propagation constants within both vacuum and dielectric. Following this condition and substituting the magnetic field expressions from the set of equations in (3.11) into equation 3.4, the reflection coefficient R can be indicated as follows:

$$R = - \left[\frac{A_1 + \left\{ \frac{1}{\epsilon_0} (A_2 e^{\alpha h} - 2) + \frac{1}{\epsilon_2} (A_2 A_3 - 2) \right\}}{A_1 + \left\{ \frac{1}{\epsilon_0} (A_2 e^{-\alpha h} - 2) + \frac{1}{\epsilon_2} (A_2 A_3 - 2) \right\}} \right] \quad (3.10)$$

where

$$\begin{aligned} A_1 &= 4 \frac{\mu h^2}{(\Delta t)^2} \sin^2 \left(\frac{\omega \Delta t}{2} \right) \\ A_2 &= 2 \cos(\beta h) \\ A_3 &= e^{-j \sqrt{(\beta h)^2 (\epsilon_{r2} - 1) - \epsilon_{r2} (\alpha h)^2}} \end{aligned} \quad (3.11)$$

The propagation of a guided wave mode is supported by the dielectric material's surface if the reflection coefficient R is approximately infinite. In order to examine such surface waves, the denominator of equation 3.10 is defined to be equal to zero. To examine the attenuation constant α as a function of the FDTD cell size h and the wavelength λ , the βh terms are eliminated. Using the numerical dispersion relation for the wave equation in the FDTD grid, e.g., from [9], follows that

$$\cos(\beta h) = \frac{1 - A_4}{\cosh(\alpha h)} \quad (3.12)$$

where

$$A_4 = \left(\frac{h}{c \Delta t} \right)^2 \sin^2 \left(\frac{\omega \Delta t}{2} \right) \quad (3.13)$$

and c indicates the speed of light in vacuum. By application of equation 3.12 for the substitution of the βh terms, a transcendental equation incorporating αh attenuation terms results as follows:

$$\begin{aligned} A_1 + \frac{1}{\epsilon_0} (e^{-j \alpha h} (2A_5) - 2) \\ + \frac{1}{\epsilon_2} \left(e^{-j \sqrt{\frac{1}{\cos^2(A_5)} (\epsilon_{r2} - 1) - \epsilon_{r2} (\alpha h)^2} - 2} \right) = 0 \end{aligned} \quad (3.14)$$

defining

$$A_5 = \frac{1 - \left(\frac{2}{C_n^2} \right) \sin^2 \left(\frac{C_n \pi h}{\sqrt{2} \lambda} \right)}{\cosh(\alpha h)} \quad (3.15)$$

and C_n denotes the Courant number, i.e., $C_n = (\sqrt{2}c\Delta t)/h$. The relation h/λ indicates the ratio of FDTD cell size to the wavelength of the excitation used.

Figure 3.3 compares the attenuation constant αh of an artificially induced surface wave versus h/λ for different values of ϵ_{r2} (for $C_n = 0.85$). Equation 3.14, i.e., $\alpha h = f(h/\lambda, \epsilon_{r2})$ directly indicates the grade of error due to the staircased interface representation. The error increases with respect to decreased FDTD grid resolution and increasing values for ϵ_{r2} . For $\epsilon_{r2} \rightarrow \infty$ the error indicated by αh approaches the one of an air-PEC material transition. In general, for common FDTD schemes the cell size h should be matched to satisfy the relation $h/\lambda \leq 0.1$.

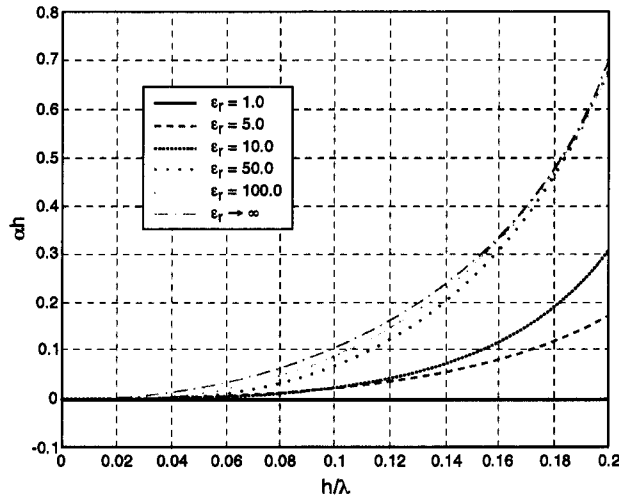


Figure 3.3: Artificially introduced surface wave due to staircasing on the air-dielectric material transition: attenuation constant αh versus h/λ for different values of ϵ_{r2} (source: [10]).

Summing up the analyzed studies, the following conclusions addressing staircasing errors can be drawn:

- In general, PEC material shows the highest influence on staircasing errors (the same tendency is observed for dielectric material with high ϵ_r).
- A significant effect is related to the polarization of an incident wave, i.e., the spatial orientation of the object with respect to EM waves.

- For an appropriate polarization of the EM wave incident on a staircased PEC structure virtual currents, surface waves and high frequency components are excited which do not occur for a properly represented object in the continuous world.
- Local staircasing errors due to single steps and voxels within dielectric materials may lead to high misestimation of local peak SAR but do not noticeably influence the averaged peak SAR.
- A slight change in the properties of dielectric materials (ϵ_r, σ) does not significantly change the staircasing error.
- Staircasing in dielectric materials may influence specially shaped geometries (focusing effect) but normally does not occur in simulation of largely non-homogeneous biological structures.
- In general, the FDTD cell size must not exceed $\lambda/10$ to achieve meaningful results. For slightly tilted PEC planes $\Delta s < \lambda/2$ should be valid for all significant frequencies in the excitation signal, where Δs indicates the diagonal length of the stairstep.

The novel algorithms which were developed within the framework of this PhD thesis do, in addition to a straightforward reduction of staircasing errors, also provide the possibility to spatially represent significant electromechanical details which would have been neglected by application of an insufficient grid resolution. The importance of this topic is pointed out in chapters 6, 7 and 8.

References

- [1] K.L. Shlager, J.G. Maloney, S.L. Ray, and A.F. Peterson, "Relative accuracy of several finite-difference time-domain methods in two or three dimensions", *IEEE Transactions on Antennas and Propagation*, vol. 41, no. 12, pp. 1732–1737, Dec. 1993.
- [2] J. Svirgelj and R. Mittra, "Grid dispersion error using the nonuniform orthogonal finite-difference time-domain method", *Microwave and Optical Technology Letters*, vol. 10, no. 4, pp. 199–201, Nov. 1995.
- [3] M. Burkhardt, *Contributions Toward Uncertainty Assessments and Error Minimization of FDTD Simulations Involving Complex Dielectric Bodies*, PhD thesis, Diss. ETH Nr.13176, Zurich, 1999.
- [4] C. Hafner, *The Generalized Multipole Technique for Computational Electromagnetics*, Artech House, 1990.
- [5] R. Holland, "Pitfalls of staircase meshing", *IEEE Transactions on Electromagnetic Compatibility*, vol. 35, no. 4, pp. 434–439, Nov. 1993.
- [6] K.R. Umashankar and A. Taflov, "A novel method to analyze electromagnetic scattering of complex objects", *IEEE Transactions on Electromagnetic Compatibility*, vol. 24, pp. 397–405, 1982.
- [7] J. B. Schneider and K. L. Shlager, "FDTD simulations of TEM horns and the implications for staircased representations", *IEEE Transactions on Antennas and Propagation*, vol. 45, no. 12, pp. 1830–1838, December 1997.
- [8] C. J. Railton and J. B. Schneider, "An analytical and numerical analysis of several locally conformal FDTD schemes", *IEEE Transactions on Microwave Theory and Techniques*, vol. 47, no. 1, pp. 56–66, January 1999.
- [9] A.C. Cangellaris and D.B. Wright, "Analysis of the numerical error caused by the stair-stepped approximation of a conducting boundary in fdtd simulations of electromagnetic phenomena", *IEEE Transactions on Antennas and Propagation*, vol. 39, no. 10, pp. 1518–1525, Oct. 1991.
- [10] A. Akyurtlu, D.H. Werner, V. Veremey, D.J. Steich, and K. Aydin, "Staircasing errors in FDTD at an air-Dielectric interface", *IEEE Microwave and Guided Wave Letters*, vol. 9, no. 11, pp. 444–446, Nov. 1999.

Chapter 4

Overview of Modeling Techniques for Local Grid Refinement in the FDTD Method

Abstract This chapter gives a wide review of existing proposed schemes for local improvement of the spatial grid resolution in the FDTD method. Major attention is thereby drawn to methods which are related to this thesis, i.e., subcell and subgridding techniques.

4.1 Introduction

Due to the reasons discussed in chapter 3, the common FDTD method inherent *staircasing* representation, for PEC material in particular, may have significant influence on the overall error in an FDTD computational domain. Within EM investigations which are strongly dependent on an appropriate representation of the surface for specific structures, these errors could lead to meaningless results. Although for such stair-stepped representations a straightforward mesh refinement produces a sufficient increase of accuracy, the results actually cannot converge to an exact solution, no matter how fine the mesh is made [1]. Moreover, an arbitrary straightforward grid refinement

is not applicable due to the limitations of computational resources, both in memory and runtime. These restrictions lead to numerous studies proposing algorithms which allow conformal or locally grid refining modeling of PEC and dielectric structures in FDTD. The schemes can be distinguished as follows:

- Cartesian grids
 - Homogeneous cartesian grids
 - Graded / non-equidistant cartesian grids
- Globally non-orthogonal grids
- Locally unstructured grids / subcell approaches
 - Contour-Path (CP) related methods
 - Subcell algorithms based on the incorporation of static field solutions
 - Algorithms applied to thin structures
- Subgrids
- Hybrid approaches

In the following section, a brief overview of the proposed methods will be given, mainly by extensively reviewing existing approaches for subcell and subgrid modeling and partially based on [2] regarding other conformal schemes.

4.2 Cartesian Grids

4.2.1 Homogeneous Cartesian Grids

In general, the avoidance of stair-stepped representations where not necessarily needed is highly recommended, due to the reasons discussed in chapter 3 in particular for PEC materials. Therefore, the orientation of PEC structures such as RF transmitters, wires or plates FDTD grid conformally aligned should be enforced. Due to reduced influence from *staircasing*, lossy dielectric objects such as head models can be placed grid non-conformally aligned.

However, for certain small-scale structures it is possibly unavoidable to apply an excessively fine grid by application of the common homogeneous

Yee grid approach which will quickly result in FDTD grid numbers limited by the computational resources available. Sections 7.2 and 8.6.9 within chapters 7 and 8 address this issue by comparison of the computational requirements for a combined graded mesh - subgrid approach to pure graded mesh as well as homogeneous grids, concluding that the range of applications is highly limited for the latter way of modeling.

4.2.2 Graded / Non-Equidistant Cartesian Grids

In order to save computational resources, a highly straightforward solution is proposed by introduction of a cartesian grid using spatial steps with varying increments along the x, y and z coordinate axes. Still maintaining rectangularly shaped cells, the approach allows the increase of the mesh resolution in specific, appropriate regions. However, since the grading expands along the entire width of a cartesian axis, the technique also wastes computational resources in regions of minor interest. Moreover, the central differences are lost due to non-uniform mesh steps, which consequently does not satisfy second order accuracy. Although preserving global second order accuracy [3, 4] of the homogeneous grid, locally first order errors influence the overall uncertainty depending on the grading ratio and cell size.

Initially reported in the late 70s, the scheme was applied to a variety of EM related problems in the field of Radar Cross Section (RCS) assessment [5, 6], waveguide structures [7, 8], numerical dosimetry [9, 10] and optics [11], demonstrating the clear outweighing of the reduced computational requirements over diminished accuracy by the grading [12, 13].

In [13, 14] heuristically derived rules are presented for appropriate mesh generation which keeps the local grading error within certain limits. A general overview of proposed methods heading a reduction of errors in non-uniform meshes is shown in [15, 16]. In addition to locally introduced errors by graded mesh, significant influence from numerical dispersion errors may occur, as reported for homogeneous mesh in [17, 18], and extensively analyzed and improved for non-homogeneous mesh in [19, 20, 21, 22].

4.3 Globally Non-Orthogonal Grids

In various situations, e.g., when bodies of revolution, spherical or cylindrical structures are involved in FDTD modeling processes, it seems appropriate to use non-orthogonal grids in order to take the structure dependent underlying coordinate system into account. A derivation of corresponding update

equations does not pose significant challenges, as has been extensively discussed in [23, 24]. Further methods using globally unstructured grids have been proposed in order to take local non-conformities into account. The first FDTD algorithm for generalized nonorthogonal coordinates is presented in [25]. In this approach, the fields are expressed in terms of their covariant (flow along a coordinate direction) and contravariant (flux through a constant coordinate surface) components. An integral formulation is used to obtain the update equations. In the early 90s the author of [25] cautioned that his original nonorthogonal grid scheme may be of limited utility compared to other more versatile conformal techniques. Different aspects of generalized non-orthogonal grid schemes were addressed, such as numerical stability, dispersion and the determination of the appropriate time step, e.g., in [26, 27]. Methods combining orthogonal with non-orthogonal grids by overlapping schemes were proposed in [28]. Within this method, the fields located in the non-orthogonal grid are connected to the orthogonal grid via spatial interpolation, a technique which is also applied in hybrid approaches as well as subridding. As discussed later in much more detail, methods which consider local non-conformities such as subcell and contour path based methods were developed. In contrast to global non-orthogonal grids, local non-conformities can be taken into account, sustaining the principal characteristics of the orthogonal FDTD method.

4.4 Locally Unstructured Grids / Subcell Approaches

4.4.1 Contour-Path (CP) Related Methods

Locally unstructured grids apply modified schemes which use a common cartesian grid in the entire computational domain except for cells directly adjacent to an object or a spatial region of particular interest. Such locally distorted meshes result in an excellent trade-off between invested computational resources and obtained accuracy due to the straightforward application to a small number of cells compared to globally unstructured mesh. The Contour Path FDTD (CPFDTD) method introduced in the early 90s [29] and [30] has been broadly suggested for the reduction of uncertainties caused by staircasing applied to PEC and dielectric objects. It is based on a formulation of Maxwell's equations in integral form, i.e., Ampère's and Faraday's law, allowing the transfer of geometrical information from FDTD grid non-conformally aligned structures into the field updating equations.

The original formulation was mainly applied to study scattering phenomena from single and multiple PEC and dielectric spherical structures [30].

Since some of EM Yee field components are affected by the presence of material transitions, they are not incorporated in the computation process, whereby a non-reciprocal *borrowing* of neighboring fields is applied. Although the common Yee scheme for non-dispersive, isotropic and lossless media has analytically proven to be stable using different approaches [31], [32], for modified schemes such as the original CPFDTD method this stability criterion is no longer valid, as shown, e.g., in [33] and [34]. Due to the use of the above mentioned non-causal and non-reciprocal collinear nearest neighbor approximation for the non-used field components, spuriously generated energy is introduced into the system, which leads to late-time instabilities within the analysis of closed and lossless resonant structures [34], [35].

In order to widen the method's capabilities to closed resonant structures, a modified scheme of the original CPFDTD method is presented, initially proposed in [35] and extended in [36] and [37]. Based on passive circuit theory including capacitors and gyrators, its approach reconstitutes the lost reciprocity by performing a forced coupling between correlated electric and magnetic field components applied to spatially extended PEC objects. The scheme was benchmarked on the basis of a grid non-conformally aligned circular cylindrical resonant cavity.

As in the mid 90s, alternative approaches to the common CPFDTD scheme were presented, e.g., in [38], where the non-reciprocal nearest neighbor approximation was not applied. However, the authors propose a similar approach to the original one, where standard Yee updating is used within the remaining computational domain. For all cells which are affected by PEC material, local corrections are applied to the update equations. The scheme was benchmarked using the analysis of microstrip lines. A very simple and basic local refinement scheme is proposed in [39]. It assumes PEC objects to have a surface shape aligned either passing through the diagonal of an FDTD cell or conformally aligned with the grid. Consequently, modified update equations are applied for the diagonally cut cells.

A conformal technique similar to the CPFDTD approach but based upon the volume-integral form of Faraday's and Ampère's laws is proposed in [40]. As performed in the original method, this scheme also applies a non-reciprocal *borrowing* of fields for certain grid components. A straightforward algorithm for incorporating 3-D geometric information about PEC structures into the FDTD update equations is proposed in [41]. This approach leads to a formulation of equations similar to that provided by the CPFDTD

method, but an additional factor, based on the electrostatic behavior of the fields, is used to modify borrowed field components. For validation, the scheme was applied for the calculation of the resonance frequencies of rectangular, cylindrical and spherical cavities.

In [42], a local refinement method is presented which is derived from the original CPFDTD approach and combined with techniques enabling improved representation of thin objects within FDTD [43], [44]. The scheme was consequently applied to model a three-dimensional pyramidal horn coated by a thin layer of dielectric material on the inner E-plane walls.

By the late 90s a novel FDTD locally conformal method applied to grid non-conformally aligned PEC structures was proposed in [45] for the 2-D case and extended to three dimensions in [46]. Its approach is very simple; moreover, it does not perform any non-reciprocal nearest neighbor approximations. The FDTD update equations for the electric field are kept the same as used in the conventional Yee scheme, while the magnetic field update equations for cells which are affected by metallic boundaries are slightly modified to incorporate geometric factors describing the metallic structure. However, in order to achieve convergence to a stable solution, the Courant number has to be reduced to 50-70% of its limit. Benchmarking of the method was performed on the basis of a spherical cavity as well as a circular microstrip patch. A study and comparison of this local refinement approach to *staircasing* and other schemes discussed within this section ([29, 39]) is presented in [47], related to narrow-angled TEM horn antennas. A study comparing the original CPFDTD method to a conformal method shown in [28] is presented in [48] on the basis of PEC circular cylinders. An extensive comparison of local refinement methods [37, 41, 46] to straightforward staircase modeling as well as to analytical results with respect to reflection from the interface boundary is performed in [49] on the basis of PEC cylindrical and spherical resonant cavities.

The locally conformal method introduced in [46] was extended from PEC objects to the modeling of grid non-conformally aligned dielectric objects in the late 90s [50] and benchmarked for open- and closed-type dielectric cylinders. A recent publication reports the method's integration into a conformal FDTD modeling and simulation package provided by the authors [51]. A combination of this method with the use of symmetry planes is shown in [52] for the analysis of center-fed bow-tie antennas.

A recent publication [53] proposes a novel method based on the original CP approach but avoiding collinear borrowing approximations by subdividing the electric fields on the distorted grid into multiple components. The scheme, applied to the simulation of a horn antenna, is compared to exper-

imental results.

An early publication from the late 70s [54] introduces so called *effective permittivities* applied to an improved modeling of 2-D grid non-conformally aligned dielectric structures. It is based on a similar approach as shown in [39] for the PEC case, i.e., by restricting dielectric material to lying either conformally aligned or in a cell-diagonal orientation. The resulting permittivity is determined from weighting the initial permittivities of two adjacent regions via contribution of the area. The technique was applied and examined, e.g., in [55] for a rotated cube exposed to a plane wave excitation in vacuum. For objects arbitrarily oriented in three dimensions the formulation was extended in [56] by introducing an averaged electric-flux density. An algorithm recently published in [57] also makes use of effective permittivities by introduction of the effective dielectric tensor, i.e., by incorporation of the dielectric boundary alignment with respect to the orientation of the electric field vector in the FDTD grid. An alternative method addressing subcell modeling of dielectric discontinuities is shown in [58] for two dimensions. Effective permittivities are determined by a preprocessing analysis of the geometrical object's intersections with FDTD grid cells. The method was extended to the 3-D case in [59] and improved with respect to applicability in [60] by overcoming the preprocessing analysis using a more general and systematic approach.

Grid-conformally aligned planar dielectric boundaries are generally treated by averaging the material properties on both sides. Recent publications [61], [62] address the issue of planar material boundaries in more detail, suggesting a method to calculate effective permittivities which retain the scheme's second-order accuracy for boundaries parallel to the grid axis without coinciding with a mesh line. An extensive analysis of such planar material interfaces is discussed in [63], further providing a general material boundary error correction for a frequency and propagation direction of optimization.

The method presented in [1] and within chapter 5 of this thesis introduces a novel CP based algorithm which mainly addresses active PEC transmitter structures non-conformally aligned to the grid.

4.4.2 Subcell Algorithms Based on the Incorporation of Static Field Solutions

Certain configurations including strongly varying field gradients may lead to unacceptable errors within FDTD, even for material boundaries which are conformally aligned to the grid. One solution to overcome these uncertain-

ties is the application of a highly resolved grid within the regions of interest, e.g., using multiple cells to resolve a thin sheet in its thickness. However, this quickly leads to challenges with respect to computational resources.

A more elegant way is based on including local static field behavior in the vicinity PEC objects, as was initially proposed in the early 90s [65] by incorporation of correction factors into the FDTD update equations of all cells affected by the material. The approach was consequently extended to an improved modeling of curved metallic boundaries in [66, 67]. However, since the schemes did not provide unconditional stability, in [68] a stable static field solution technique is proposed based on energy conservation, incorporating a priori field knowledge into the FDTD algorithm. In a publication from the late 90s [69], the same authors present a novel technique for the analysis of thin wires and narrow strips. It is based on a finite element formulation which provides a means by which FDTD may be generalized to include whatever a priori knowledge of the field is available without compromising stability. A simple technique to improve the accuracy of the staircased FDTD method is presented in [70] for flat metal planes or metallic corners which are not aligned conformally to the grid. This technique relies as well on the incorporation of correction factors based on the electrostatic field behavior near affected PEC structures. More recently, within [71] the technique presented in [68] was extended to handle situations where sharp metal edges are not aligned with the grid. This novel scheme was used to analyze microwave related applications in [72].

The incorporation of a priori field knowledge into the standard FDTD algorithm overcomes the limitations of strongly varying fields in the vicinity of metallic structures. For this specific kind of application, the summarized techniques are therefore superior to any other approach, due to a possible use of rather coarse grids instead of enormously high mesh refinements. Although a similar effect is achievable by application of subgridding, these techniques will be considered for further investigation.

4.4.3 Algorithms Applied to Thin Structures

For extremely high ratios with respect to wavelength and the smallest possible spatial extension of the geometrical structure, the application of special FDTD subcell models is highly necessary. In particular for thin structures like wires, sheets and slots, a straightforward modeling by the common FDTD scheme would quickly lead to limitations of computational resources. By straightforward application of coarsely resolved grids to geometries with spatial subcell extension, the dimension of the structure will be determined

by the grid resolution, which hardly ever matches its actual dimension. In the following section, a number of algorithms targeted for enhanced representation of such structures are summarized.

In the early 80s the implementation and analysis of an FDTD thin strut formalism was presented in [73]. It allows the modeling of arbitrarily thin wires in the FDTD technique, without the need to reduce the FDTD grid size to the thickness of the wire. An FDTD thin slot formulation (TSF), based on representing the slot with a modified material, was presented in [74]. Following the work proposed in [75], update equations were derived which are suitable for the modeling of sub-cellular structures such as wires, narrow slots, and lapped joints embedded within conducting screens [76, 77] leading, e.g., to the well known *thin-wire* formalism. The corresponding update equations were obtained from the integral form of Faraday's law rather than the differential form and resulted in modified equations only for cells directly adjacent to the sub-cellular structure.

Enhancements of the presented subcell models were consequently initiated within various following studies in the beginning of the 90s. The application of an integro-differential equation formalism to thin slots is presented in [78] and was extended to model lossy slots by the use of a surface boundary condition [79]. Enhancements with respect to thin slot formalisms by incorporation of singularities by the field variation near the slot are proposed in [80]. The same authors also presented a small hole formalism for small hole coupling [81]. A similar approach applied to thin aperture scattering is shown in [82]. Major investigations with respect to accuracy and late time instabilities for this kind of local refinement scheme have been performed in [83] and [84].

FDTD subcell methods particularly applied to conducting as well as dielectric thin sheets were initially reported in [85]. A further enhanced model addressing dielectric sheets by considering both, normal and tangential field components at the air/sheet interface was presented in [43]. Other subcell models focusing on subcell modeling of thin PEC and dielectric material sheets were independently proposed in [44], [86] and [87]. The latter two publications only consider the tangential E-field component at the thin sheet/air transition. A comparison of FDTD methods for modeling thin dielectric and conducting sheets is given in [88].

A recent publication [89] introduces an elegant way of modeling thin wires by extending the *thin-wire* formalism proposed in [76]. The authors report the particularly high suitability of the scheme for antennas using dipole-like sources. The improvements were achieved using modified field components, mainly in the wire-end region, obtained from results performed

by application of the Method-of-Moments (MoM). Moreover, a novel and corresponding improved feed/excitation model applied to this kind of structure is presented in [90]. A recent study addressing improved modeling of thin PEC sheets is shown in [91], extending the method initially proposed in [46] to thin sheets.

The algorithms summarized in this section provide a very effective method of representing specific thin structures such as wires and sheets. However, the use of subgrids to assess the required grid resolution presents a more canonical way with respect to the FDTD method; moreover, it includes the possibility for later introduction of thin-structure schemes.

4.5 Subgrids

A very general and highly efficient approach to overcome restrained grid resolution is the introduction of a subgrid. Such subdomains consist of smaller FDTD mesh cells and are placed themselves within a specific sub-region of the computational domain. The grid structure of the remaining main grid is thereby not modified, i.e., no computational resources are wasted in regions of minor interest as from using graded mesh.

The subgridding topic was initially reported in the early 80s [92], introducing a technique which applies two separate updating cycles for the field computation. Within the first cycle all components located in the main grid are updated, whereby field components in the boundary region of the subgrid are stored. These values consequently act as boundary solutions used for the computation of the local grid in a second cycle. Extended but still simple schemes were presented at the end of the 80s in [93, 94] based on linear interpolation in both time and space.

Within the last 15 years the development of various subgrid algorithms has been reported, solving the most crucial issue in subgridding - the transfer of field information between coarse and fine grid - by application of different approaches. Compared to [92], these schemes allow the simultaneous processing of both main- and subgrid within one single updating cycle.

Schemes based on the Helmholtz Equation show high efficiency but are mainly applied to plane wave examples and often derived for the 2-D case only. In [18], a 2-D approach based on general hyperbolic partial differential equations [95] applied to Maxwell's curl equations and assuming TE mode propagation is introduced. A nestable basic refinement of 1:4 is achieved and tested for a waveguide example. In [96], a simple 1:2 refinement technique based on spatial interpolation of E- and H-fields in the interface region is

briefly discussed. A detailed description is given for a 1:3 subgridding technique based on a discretized form of the wave equation in order to obtain fields located at the boundary. The applicability of this scheme is restricted to homogeneous media. A modification of this technique is shown in [97], leading to improved efficiency, demonstrated on the basis of a 2-D rectangular waveguide. The authors report reflections of less than -45 dB for frequencies up to 65 GHz. The cell sized used for this example was not reported. A recent publication [98] addressing the Helmholtz equation uses optimal chosen FDTD updating coefficients for the transition region from coarse to fine grids which were derived from a technique minimizing the phase error [20]. For validation, 2-D scattering and propagation problems were applied. An alternative 2-D approach targeting the determination of optimized coupling coefficients between main- and subgrid is presented in [99] by application of the wave equation. The authors report good performance compared to a non-optimized method, i.e., low reflections (-70 dB to -40 dB) in a 25 GHz broad frequency range, tested in 2-D waveguide problems.

A 3-D approach (1:2 refinement) based on curl and source matrices in the Finite-Integration (FI) technique [100] shows a good behavior with respect to stability but therefore requires reduction of the timestep determined by the Courant-Friedrichs-Lewy (CFL) criterion by a factor of 2. Recently, a similar method was presented in [101] and [102] where the authors apply a passive electrical circuit equivalent approach [35] combined with a modified temporal interpolation scheme to increase stability. In contrast to [100], a 1:3 refinement is applied. Reflections in the range of -40 dB in up to 20 GHz (0.3 mm subgrid mesh step) were reported, assessed on the basis of inhomogeneous resonator examples.

In [103] the method presented in [97] was extended to three dimensions and modified for the coarse-grid updating procedure to achieve higher stability than the original scheme. However, the method does not allow materials traversing the boundary, and reflections from the subgrid boundaries in the range of -35 dB have been reported for refinement factors around 3 applied to waveguide structures. In a recent publication [104], the same authors propose a novel subgridding technique based on Ampère's law in integral form which extends the previous approach to enable PEC or dielectric materials passing the boundary. The reported reflections are in the same range as shown in [103], but the scheme was tested for refinements up to 1:11.

Significant improvements with respect to generalized applicability are achieved by methods introduced in the late 90s which are based on 3-D spatial and temporal interpolation for the data transfer between coarse and fine grids. In [105] a scheme (1: odd integer refinement) is proposed which

permits non-magnetic or PEC materials to traverse the interface boundary between the two grids. Linear interpolation is applied for the determination of boundary field values; furthermore, correction factors are introduced in order to improve stability. Reflections in the range of -45 dB (1:3 refinement, $\lambda/10$ cell size) as well as reductions of the maximum CFL to about 0.7 have been reported, based on antenna and scattering problems. Stability is tested for up to 22 000 timesteps. A method, again based on linear interpolation in space and combined interpolation/extrapolation in time but by considering both E- and H-fields in the interface region, is presented in [106]. For a 1:5 refinement using a $\lambda/50$ cell size in the subgrid, the reflection error is in the range of -50 dB derived from a scattering example. Stability was tested for 2 500 timesteps by reducing the maximum CFL to about 0.5. The scheme does not yet support materials traversing the subgrid - main grid interface. Excellent performance with respect to both low reflections and high stability is demonstrated in [107]. The algorithm, based on spline interpolation in space and combined interpolation/extrapolation in time applied to an overlapping region connecting both grids, allows an intersection of dielectric and PEC material at the boundary. Reflections below -50 dB in a 20 GHz range (0.5 mm cells size) are reported, assessed for a number of parallel plate and waveguide examples. A nested mesh application of this scheme presented in [108] to model antenna structures such as dipoles and helices shows errors up to 20% for certain configurations ($\lambda/2$ dipole at $f = 900$ MHz, $\lambda/300$ cell size, 1:16 refinement) in the closest vicinity of the antenna. A linear interpolation based scheme, also using an overlapping connecting region such as in [107] and combined with correction factors, is derived for the 2-D case in [109]. Qualitatively good results are reported, based on plane wave and a thin slot example. In [110] the authors present an alternative linear interpolation based approach which was applied for characterization of far-field parameters and RCS of an antenna and a numerically represented missile.

An efficient subgridding scheme applied to regions of different dielectric constants embedded into each other is proposed in [111]. It is derived for two dimensions, and the refinement factor is determined by the ratio obtained for two adjacent dielectrics. In addition, a basic stability analysis was performed. Basic investigations on subgridding error analysis and stability is presented in [112, 113] for the spatial scheme of a specific 2-D subgrid based on a simple interpolation approach. In [27], methodologies regarding the general numerical stability of the FDTD technique are discussed and finally applied to the subgrid method presented in [100].

The subgridding scheme proposed in [2] and within chapter 6 of this thesis was developed with a focus on robustness, stability and general ap-

plicability, i.e., by allowing the traverse of arbitrary material distributions in the subgrid - main grid boundary. Its flexible nature enabled a straightforward implementation into a CAD environment providing automated grid generation.

4.6 Hybrid Approaches

Methods different from FDTD may have specific advantages for certain configurations incorporating increased homogeneity, e.g., a single curved antenna structure might be modeled more appropriately using a Finite-Element (FE) technique rather than FDTD due to the stair-stepped approach. Therefore, major attempts have been performed to combine FDTD with other methods, leading to an assembly of the individual method's advantages.

Initial efforts to achieve hybridization are reported in [115] for combining FDTD with the Method-of-Moments (MoM) within an investigation on coupling problems. In the beginning of the 90s hybrid approaches were extended to combine FDTD with other methods such as presented in [116] for the scalar wave equation applied to the simulation of a Vivaldi antenna, reducing the computational requirements. Introducing a hybrid ray-FDTD method applied to examine scattering from a cavity with complex termination was presented in [117]. The FDTD method was coupled with the Partial Eigenfunction Expansion (PEE) in [118] achieving major improvements with respect to computation time for shielded structures. An extension of this method to cylindrical coordinate systems is presented in [119]. Also by the mid 90s FDTD hybridization was widened to incorporate domain methods such as FET as well as the Finite-Volume Time-Domain (FVTD) formulation. In [120] a technique was derived, combining FDTD with FVTD based on conformal and unstructured grids by application of interpolation for the data exchange and applied to scattering problems. The direct coupling of two different methods without using interpolation is shown in [121] for an unstructured FV grid with a structured cartesian Yee mesh by positioning corresponding cells of each grid on the same nodes. Interfacing of an FE scheme is performed in [122] by incorporation of an overlapping transition region between the two grids and solved by means of the FE method in the time domain. The method is consequently extended to additionally include MoM in [123]. Recent publications report the hybridization of different coordinate systems within FDTD, such as for cartesian-cylindrical approaches in [124] and [125] to analyze cylindrical structures with enhanced performance.

4.7 Conclusion

Targeting the usability of numerical simulations for a wide range of applications in the fields of antenna design, EMC, EMI as well as dosimetry, the following requirements with respect to FDTD modeling capabilities can be summed up:

- ability to model highly nonhomogeneous lossy dielectric and PEC structures / material distributions
- possibility to resolve highly detailed and small structures
- application to large ratios between widest spatial extension and smallest detail structure
- high applicability for large ratios between FDTD cell size and smallest wavelength
- highest possible flexibility for integration into existing FDTD environments
- high suitability for combination/integration in automated FDTD grid generation within CAD environment
- high performance with respect to robustness, stability and low disturbing influence of the incorporated algorithm
- high efficiency with respect to time and memory consumption

Recapitulating all concluding remarks given in chapters 3 and 4, furthermore considering the availability of the state-of-the-art 3-D full wave FDTD solver from the MINAST EMSIM project as well as the simulation platform SEMCAD as the basis for implementation, the following methods have been determined to be the most appropriate:

- subcell CP based approach:
 - the CP approach has proven to be widely applicable to various problems (PEC, dielectric); most of the presented subcell schemes are originally CP based
 - it is easily extendable to match certain configurations, e.g., by incorporation of static field solutions

- although the object's shape has to be geometrically analyzed, a straightforward implementation into existing FDTD codes is enabled (application only to adjacent cells)
 - in case of instabilities (closed resonating structures), modified algorithms have been suggested
 - high computational efficiency is achieved, since only a low number of grid cells (adjacent to object of interest) has to be modified
 - the method leads to highly improved accuracy while being computationally inexpensive (only modification of update coefficients)
- interpolation based subgrid approach:
 - particularly applicable to specific regions of interest in order to improve local field behavior (e.g., for scattering, near-field coupling, strong field gradients, etc.), no waste of computational resources
 - possible combination with automated grid generation, based on cartesian coordinate system
 - possibility of grid nesting
 - combination with other local grid refinement techniques provided, e.g., for combined subgrid - graded mesh schemes
 - incorporation of high flexibility through subgridding due to its general applicability (no restrictions with respect to usage within complex non-homogeneous environments)
 - no limitations with respect to the modeling of relevant fine and detailed structures
 - no geometrical analysis of affected objects/structures required
 - straightforward integration into existing FDTD codes, only slight modification of implemented structures
 - computationally highly efficient due to multi-grid structure, i.e., processing of Yee scheme within individual grids which are interfaced with each other
 - parallelizable

References

- [1] A.C. Cangellaris and D.B. Wright, "Analysis of the numerical error caused by the stair-stepped approximation of a conducting boundary in fdtd simulations of electromagnetic phenomena", *IEEE Transactions on Antennas and Propagation*, vol. 39, no. 10, pp. 1518–1525, Oct. 1991.
- [2] K. L. Shlager and J. B. Schneider, "A survey of the finite-difference time-domain literature", in *Advances in Computational Electrodynamics: The Finite-Difference Time-Domain Method*, A. Taflové, Ed., chapter 1, pp. 1–62. Artech House, Boston, MA, 1998.
- [3] P. Monk and E. Süli, "A convergence analysis of Yee's scheme on non-uniform grids", *SIAM Journal of Numerical Analysis*, vol. 31, no. 2, pp. 393–412, April 1994.
- [4] P. Monk and E. Süli, "Error estimates for Yee's method on non-uniform grids", *IEEE Transactions on Magnetics*, vol. 30, no. 5, pp. 3200–3203, September 1994.
- [5] K. S. Kunz and K. M. Lee, "A three-dimensional finite-difference solution of the external response of an aircraft to a complex transient EM environment: I—The method and its implementation", *IEEE Transactions on Electromagnetic Compatibility*, vol. 20, no. 2, pp. 328–333, 1978.
- [6] K. S. Kunz and K. M. Lee, "A three-dimensional finite-difference solution of the external response of an aircraft to a complex transient EM environment: II—Comparison of predictions and measurements", *IEEE Transactions on Electromagnetic Compatibility*, vol. 20, no. 2, pp. 333–341, 1978.
- [7] V. J. Branković, D. V. Krupežević, and F. Arndt, "An efficient two-dimensional graded mesh finite-difference time-domain algorithm for shielded or open wave-guide structures", *IEEE Transactions on Microwave Theory and Techniques*, vol. 40, no. 12, pp. 2272–2277, December 1992.
- [8] E. A. Navarro, N. T. Sangary, and J. Litva, "Some considerations on the accuracy of the nonuniform FDTD method and its applications to waveguide analysis when combined with the perfectly matched layer

- technique", *IEEE Transactions on Microwave Theory and Techniques*, vol. 44, no. 7, pp. 1115–1124, July 1996.
- [9] A. Tinniswood, G. Lazzi, and O.P. Gandhi, "The use of the expanding-Grid FDTD method for simulation of CAD-Derived personal wireless telephones", *Microwave and Optical Technology Letters*, vol. 22, no. 1, pp. 24–29, July 1999.
- [10] P. Bernardi, M. Cavagnaro, S. Pisa, and E. Piuze, "A graded-mesh FDTD code for the study of human exposure to cellular phones equipped with helical antennas", *Applied Computational Electromagnetics Society Journal*, vol. 16, no. 2, pp. 90–96, July 2001.
- [11] G. Shen, Y. Chen, and R. Mittra, "A nonuniform FDTD technique for efficient analysis of propagation characteristics of optical-fiber waveguides", *IEEE Transactions on Microwave Theory and Techniques*, vol. 47, no. 3, pp. 345–349, March 1999.
- [12] D.H. Choi and W.J.R. Hofer, "A graded mesh FD-TD algorithm for eigenvalue problems", in *17th European Microwave Conference Digest*, 1987, pp. 413–417.
- [13] B. Q. Gao and O. P. Gandhi, "An expanding-grid algorithm for the finite-difference time-domain method", *IEEE Transactions on Electromagnetic Compatibility*, vol. 34, no. 3, pp. 277–283, August 1992.
- [14] W. Heinrich, K. Beilenhoff, P. Mezzanotte, and L. Roselli, "Optimum mesh grading for finite-Difference method", *IEEE Transactions on Microwave Theory and Techniques*, vol. 44, no. 9, pp. 1569–1574, Sept. 1996.
- [15] S. Xiao and R. Vahldieck, "A fast FDTD analysis of guided wave structures using a continuously variable mesh with second order accuracy", *Journal of the Institute of Electronics and Telecommunication Engineers*, vol. 41, no. 1, pp. 3–14, 1995.
- [16] R. C. Tupynamba and A. S. Omar, "Comparison between FDTD graded grids", in *IEEE MTT-S Int. Microwave Symp.*, Baltimore, MD, June 1998, vol. 2, pp. 905–906.
- [17] A. Taflov, *Computational Electrodynamics - The Finite Difference Time Domain Method*, Artech House, Norwood, MA, 1995.

- [18] I. S. Kim and W. J. R. Hoefer, "Numerical dispersion characteristics and stability factor for the TD-FD method", *Electronics Letters*, vol. 26, no. 7, pp. 485–487, 1990.
- [19] J. Svirgelj and R. Mittra, "Grid dispersion error using the nonuniform orthogonal finite-difference time-domain method", *Microwave and Optical Technology Letters*, vol. 10, no. 4, pp. 199–201, Nov. 1995.
- [20] J. W. Nehrass, J. O. Jevtić, and R. Lee, "Reducing the phase error for finite-difference methods without increasing the order", *IEEE Transactions on Antennas and Propagation*, vol. 46, no. 8, pp. 1194–1201, August 1998.
- [21] J. B. Schneider and C. L. Wagner, "FDTD dispersion revisited: Faster-than-light propagation", *IEEE Microwave Guided Wave Letters*, vol. 9, no. 2, pp. 54–56, February 1999.
- [22] Andreas Christ, Jürg Fröhlich, and Niels Kuster, "Analysis and correction of numerical phase velocity errors in nonuniform FDTD meshes", *IEEE Transactions on Microwave Theory and Techniques*, 2001, submitted.
- [23] A. Taflov, *Advances in Computational Electromagnetics: The Finite Difference Time Domain Method*, Artech House, Norwood, MA, 1998.
- [24] A. Taflov and S. C. Hagness, *Computational Electrodynamics - The Finite Difference Time Domain Method, 2nd Edition*, Artech House, Norwood, MA, 2000.
- [25] R. Holland, "Finite difference solutions of Maxwell's equations in generalized nonorthogonal coordinates", *IEEE Transactions on Nuclear Science*, vol. NS-30, no. 6, pp. 4589–4591, 1983.
- [26] R. Nilavalan, I. J. Craddock, and C. J. Railton, "Practical method for the determination of time step in non-orthogonal FDTD", *Electronics Letters*, vol. 37, no. 11, pp. 679–680, May 2001.
- [27] P. Thoma and T. Weiland, "Numerical stability of finite difference time domain methods", *IEEE Transactions on Magnetics*, vol. 34, no. 5, pp. 2740–2743, September 1998.
- [28] K. S. Yee, J. S. Chen, and A. H. Chang, "Conformal finite-difference time-domain (FDTD) with overlapping grids", *IEEE Transactions on*

Antennas and Propagation, vol. 40, no. 9, pp. 1068–1075, September 1992.

- [29] T.G. Jurgens, A. Taflove, K. Umashankar, and T.G. Moore, “Finite-difference time-domain modeling of curved surfaces”, *IEEE Transactions on Antennas and Propagation*, vol. 40, no. 4, pp. 357–366, Apr. 1992.
- [30] T.G. Jurgens and A. Taflove, “Three-dimensional contour FDTD modeling of scattering from single and multiple bodies”, *IEEE Transactions on Antennas and Propagation*, vol. 41, no. 12, pp. 1703–1708, Dec. 1993.
- [31] A. Taflove and M.E. Brodwin, “Numerical solution of steady-state electromagnetic scattering problems using the time-dependent Maxwell’s equations”, *IEEE Transactions on Microwave Theory and Techniques*, vol. 23, pp. 623–630, Aug. 1975.
- [32] J.A. Pereda, L.A. Vielva, A. Vegas, and A. Prieto, “Analyzing the stability of the FDTD technique by combining the von Neumann method with the Routh-Hurwitz criterion”, *IEEE Transactions on Microwave Theory and Techniques*, vol. 49, no. 2, pp. 377–381, Feb. 2001.
- [33] N.K.Madsen, “Divergence preserving discrete surface integral methods for Maxwell’s curl equations using nonorthogonal unstructured grids”, *Tech. Rep. UCRL-JC-109787, Lawrence Livermore National Laboratory*, 1992.
- [34] M. Okoniewski, J. Anderson, J. Mrozowski, and S.S. Stuchly, “Arbitrarily located metal surfaces in FDTD technique”, *Progress in Electromagnetics Research Symposium, Seattle, WA*, 1995.
- [35] I.J. Craddock, C.J. Railton, and J.P. McGeehan, “Derivation and application of a passive equivalent circuit for the finite difference time domain algorithm”, *IEEE Microwave and Guided Wave Letters*, vol. 6, no. 1, pp. 40–42, 1996.
- [36] C.J. Railton and I.J. Craddock, “Stabilized CPFDTD algorithm for the analysis of arbitrary 3D PEC structures”, *IEE Proceedings on Microwaves, Antennas and Propagation*, vol. 143, no. 5, pp. 367–372, Oct. 1996.

- [37] C.J. Railton, I.J. Craddock, and J.B. Schneider, "The analysis of general two-dimensional PEC structures using a modified CPFDTD algorithm", *IEEE Transactions on Microwave Theory and Techniques*, vol. 44, no. 10, pp. 1728–1733, Oct. 1996.
- [38] J. Fang and J. Ren, "A locally conformed finite-difference time-domain algorithm of modeling arbitrary shape planar metal strips", *IEEE Transactions on Microwave Theory and Techniques*, vol. 41, no. 5, pp. 830–838, May 1993.
- [39] P. Mezzanotte, L. Roselli, and R. Sorrentino, "A simple way to model curved metal boundaries in FDTD algorithm avoiding staircase approximation", *IEEE Microwave Guided Wave Letters*, vol. 5, no. 8, pp. 267–269, August 1995.
- [40] S. G. Garcia, T. M. Hung-Bao, B. G. Olmedo, and R. G. Mart'in, "Volume-conformation method to study scattering by PEC objects with FDTD", *IEE Proceedings H: Microwaves, Antennas and Propagation*, vol. 143, no. 2, pp. 131–136, April 1996.
- [41] J. Anderson, M. Okoniewski, and S. S. Stuchly, "Practical 3-D contour/staircase treatment of metals in FDTD", *IEEE Microwave Guided Wave Letters*, vol. 6, no. 3, pp. 146–148, March 1996.
- [42] P.A. Tirkas and C.A. Balanis, "Contour path FDTD method for analysis of pyramidal horns with composite inner E-plane walls", *IEEE Transactions on Antennas and Propagation*, vol. 42, no. 11, pp. 1476–1483, Nov. 1994.
- [43] P. A. Tirkas and K. R. Demarest, "Modeling of thin dielectric structures using finite-difference time-domain technique", *IEEE Transactions on Antennas and Propagation*, vol. 39, no. 9, pp. 1338–1344, September 1991.
- [44] J. G. Maloney and G. S. Smith, "The efficient modeling of thin material sheets in the finite-difference time-domain (FDTD) method", *IEEE Transactions on Antennas and Propagation*, vol. 40, no. 3, pp. 323–330, March 1992.
- [45] S. Dey, R. Mittra, and S. Chebolu, "A technique for implementing the FDTD algorithm on a nonorthogonal grid", *Microwave and Optical Technology Letters*, vol. 14, no. 4, pp. 213–215, March 1997.

- [46] S. Dey and R. Mittra, "A locally conformal finite-difference time-domain (FDTD) algorithm for modeling three-dimensional perfectly conducting objects", *IEEE Microwave Guided Wave Letters*, vol. 7, no. 9, pp. 273–275, September 1997.
- [47] J. B. Schneider and K. L. Shlager, "FDTD simulations of TEM horns and the implications for staircased representations", *IEEE Transactions on Antennas and Propagation*, vol. 45, no. 12, pp. 1830–1838, December 1997.
- [48] M.W. Steeds, S.L. Broschat, and J.B. Schneider, "A comparison of two conformal methods for FDTD modeling", *IEEE Transactions on Electromagnetic Compatibility*, vol. 38, no. 2, pp. 181–187, May 1996.
- [49] C. J. Railton and J. B. Schneider, "An analytical and numerical analysis of several locally conformal FDTD schemes", *IEEE Transactions on Microwave Theory and Techniques*, vol. 47, no. 1, pp. 56–66, January 1999.
- [50] S. Dey and R. Mittra, "A conformal finite-difference time-domain technique for modeling cylindrical dielectric resonators", *IEEE Transactions on Microwave Theory and Techniques*, vol. 47, no. 9, pp. 1737–1739, September 1999.
- [51] W. Yu and R. Mittra, "A conformal FDTD software package modeling antennas and microstrip circuit components", *IEEE Antennas and Propagation Magazine*, vol. 42, no. 5, pp. 28–39, October 2000.
- [52] J. George, "A fast and efficient FDTD approach for the modeling of center-fed bow-tie microstrip antennas", *Microwave and Optical Technology Letters*, vol. 28, no. 4, pp. 272–274, February 2001.
- [53] Y. Min, B. Kil, and S. Lee, "Novel contour-path finite-difference time-domain (CPFDTD) algorithm for modeling objects with curved surfaces", *Microwave and Optical Technology Letters*, vol. 28, no. 4, pp. 285–287, February 2001.
- [54] T. Weiland, "Verlustbehaftete wellenleiter mit beliebiger randkontur und materialbelegung", *AE"U*, vol. 33, no. 4, pp. 170–174, 1979.
- [55] M. Burkhardt, *Contributions Toward Uncertainty Assessments and Error Minimization of FDTD Simulations Involving Complex Dielectric Bodies*, PhD thesis, Diss. ETH Nr.13176, Zurich, 1999.

- [56] N. Kaneda, B. Houshmand, and T. Itoh, "FDTD analysis of dielectric resonators with curved surfaces", *IEEE Transactions on Microwave Theory and Techniques*, vol. 45, no. 9, pp. 1645–1649, September 1997.
- [57] J.-Y. Lee and N.-H. Myung, "Locally tensor conformal FDTD method for modeling arbitrary dielectric surfaces", *Microwave and Optical Technology Letters*, vol. 23, no. 4, pp. 245–249, 1999.
- [58] W. K. Gwarek, "Analysis of an arbitrarily-shaped planar circuit—A time-domain approach", *IEEE Transactions on Microwave Theory and Techniques*, vol. 33, no. 10, pp. 1067–1072, October 1985.
- [59] M. Celuch-Marcysiak and W. K. Gwarek, "Higher order modelling of media interfaces for enhanced FDTD analysis of microwave circuits", in *24th European Microwave Conf.*, Cannes, France, September 1994, pp. 1530–1535.
- [60] G. Marrocco, M. Sabbadini, and F. Bardati, "FDTD improvement by dielectric subgrid resolution", *IEEE Transactions on Microwave Theory and Techniques*, vol. 46, no. 12, pp. 2166–2169, Dec. 1998.
- [61] T. Hirono, Y. Shibata, W. W. Lui, S. Seki, and Y. Yoshikuni, "The second-order condition for the dielectric interface orthogonal to the Yee-lattice axis in the FDTD scheme", *IEEE Microwave Guided Wave Letters*, vol. 10, no. 9, pp. 359–361, September 2000.
- [62] K.-P. Hwang and A. C. Cangellaris, "Effective permittivities for second-order accurate FDTD equations at dielectric interfaces", *IEEE Microwave and Wireless Components Letters*, vol. 11, no. 4, pp. 158–160, April 2001.
- [63] Andreas Christ, Andreas Witzig, Niels Kuster, and Wolfgang Fichtner, "Correcting the numerical reflection coefficient of the FDTD method for the efficient simulation of VCSE-Lasers", to be submitted.
- [64] N. Chavannes and N. Kuster, "A novel 3-D CPFDTD scheme for modeling grid non-Conformally aligned transmitter structures", *IEEE Transactions on Antennas and Propagation*, Submitted, 2001.
- [65] D.B. Shorthouse and C.J. Railton, "The incorporation of static field solutions into the finite difference time domain algorithm", *IEEE Transactions on Microwave Theory and Techniques*, vol. 40, pp. 986–994, 1992.

- [66] C.J. Railton, "Use of static field solutions in the fdtd method for the efficient treatment of curved metal surfaces", *Electronics Letters*, vol. 29, no. 16, pp. 1466-1467, 1993.
- [67] C. J. Railton, "An algorithm for the treatment of curved metallic laminas in the finite difference time domain method", *IEEE Transactions on Microwave Theory and Techniques*, vol. 41, no. 8, pp. 1429-1438, August 1993.
- [68] I. J. Craddock and C. J. Railton, "Stable inclusion of *a priori* knowledge of field behavior in the FDTD algorithm: Application to the analysis of microstrip lines", in *IEEE Antennas and Propagat. Soc. Int. Symp.*, Baltimore, MD, July 1996, vol. 2, pp. 1300-1303.
- [69] I. J. Craddock and C. J. Railton, "A new technique for the stable incorporation of static field solutions in the FDTD method for the analysis of thin wires and narrow strips", *IEEE Transactions on Microwave Theory and Techniques*, vol. 46, no. 8, pp. 1091-1096, August 1998.
- [70] J. Anderson, M. Okoniewski, and S. S. Stuchly, "Subcell treatment of 90° metal corners in FDTD", *Electronics Letters*, vol. 31, no. 25, pp. 2159-2160, December 1995.
- [71] K. P. Esselle, M. Okoniewski, and M. A. Stuchly, "Analysis of sharp metal edges at 45° to the FDTD grid", *IEEE Microwave Guided Wave Letters*, vol. 9, no. 6, pp. 221-223, June 1999.
- [72] S. M. Foughipour and K. P. Esselle, "Enhanced FD-TD equations for diagonal metal edges and their microwave applications", in *Asia-Pacific Microwave Conf., APMC 2000*, Sydney, Australia, December 2000, pp. 361-364.
- [73] R. Holland and L. Simpson, "Finite-difference analysis of EMP coupling to thin struts and wires", *IEEE Transactions on Electromagnetic Compatibility*, vol. EMC-23, no. 2, pp. 88-97, May 1981.
- [74] J. Gilbert and R. Holland, "Implementation of the thin-slot formalism in the finite-difference EMP code THREDII", *IEEE Transactions on Nuclear Science*, vol. NS-28, no. 6, pp. 4269-4274, 1981.
- [75] K. S. Yee, "Numerical solution to Maxwell's equations with non-orthogonal grids", Tech. Rep. UCRL-93268, Lawrence Livermore National Laboratory, 1987.

- [76] K. R. Umashankar, A. Taflove, and B. Beker, "Calculation and experimental validation of induced currents on coupled wires in an arbitrary shaped cavity", *IEEE Transactions on Antennas and Propagation*, vol. 35, no. 11, pp. 1248–1257, November 1987.
- [77] A. Taflove, K. R. Umashankar, B. Beker, F. Harfoush, and K. S. Yee, "Detailed FD-TD analysis of electromagnetic fields penetrating narrow slots and lapped joints in thick conducting screens", *IEEE Transactions on Antennas and Propagation*, vol. 36, no. 2, pp. 247–257, February 1988.
- [78] D. J. Riley and C. D. Turner, "Hybrid thin-slot algorithm for the analysis of narrow apertures in finite-difference time-domain calculations", *IEEE Transactions on Antennas and Propagation*, vol. 38, no. 12, pp. 1943–1950, December 1990.
- [79] D. J. Riley and C. D. Turner, "The inclusion of wall loss in finite-difference time-domain thin-slot algorithms", *IEEE Transactions on Electromagnetic Compatibility*, vol. 33, no. 4, pp. 304–311, 1991.
- [80] B.-Z. Wang, "Enhanced thin-slot formalism for the FDTD analysis of thin-slot penetration", *IEEE Microwave Guided Wave Letters*, vol. 5, no. 5, pp. 142–143, May 1995.
- [81] B.-Z. Wang, "Small-hole formalism for the FDTD simulation of small-hole coupling", *IEEE Microwave Guided Wave Letters*, vol. 5, no. 1, pp. 15–17, January 1995.
- [82] J. H. Oates and R. T. Shin, "Small aperture modeling for EMI applications using the finite-difference time-domain technique", *Journal of Electromagnetic Waves and Applications*, vol. 9, no. 1/2, pp. 37–69, 1995.
- [83] K.-P. Ma, M. Li, J. L. Drewniak, T. H. Hubing, and T. P. Van Doren, "Comparison of FDTD algorithms for subcellular modeling of slots in shielding enclosures", *IEEE Transactions on Electromagnetic Compatibility*, vol. 39, no. 2, pp. 147–155, 1997.
- [84] M. Li, K.-P. Ma, D. M. Hockanson, J. L. Drewniak, T. H. Hubing, and T. P. Van Doren, "Numerical and experimental corroboration of an FDTD thin-slot model for slots near corners of shielding enclosures", *IEEE Transactions on Electromagnetic Compatibility*, vol. 39, no. 3, pp. 225–232, 1997.

- [85] C. J. Railton and J. P. McGeehan, "An analysis of microstrip with rectangular and trapezoidal conductor cross sections", *IEEE Transactions on Microwave Theory and Techniques*, vol. 38, no. 8, pp. 1017–1022, August 1990.
- [86] R. J. Luebbers and K. Kunz, "FDTD modeling of thin impedance sheets", *IEEE Transactions on Antennas and Propagation*, vol. 40, no. 3, pp. 349–350, March 1992.
- [87] J. J. Boonzaaier and C. W. I. Pistorius, "Scattering by thin lossy dielectric plates— A finite-difference time-domain approach", *Microwave and Optical Technology Letters*, vol. 6, no. 5, pp. 326–332, 1993.
- [88] J. G. Maloney and G. S. Smith, "A comparison of methods for modeling electrically thin dielectric and conducting sheets in the finite-difference time-domain (FDTD) method", *IEEE Transactions on Antennas and Propagation*, vol. 41, no. 5, pp. 690–694, May 1993.
- [89] M. Douglas, M. Okoniewski, and M. A. Stuchly, "Accurate modeling of thin-wire antennas in the FDTD method", *Microwave and Optical Technology Letters*, vol. 21, no. 4, pp. 261–265, 1999.
- [90] S. Watanabe and M. Taki, "An improved FDTD model for the feeding gap of a thin-wire antenna", *IEEE Microwave Guided Wave Letters*, vol. 8, no. 4, pp. 152–154, April 1998.
- [91] S. Dey, "Efficient modeling of thin perfectly conducting sheet type of objects by using the finite-difference time-domain technique", *Microwave and Optical Technology Letters*, vol. 28, no. 5, pp. 333–336, March 2001.
- [92] K. S. Kunz and L. Simpson, "A technique for increasing the resolution of finite-difference solutions of the Maxwell's equation", *IEEE Transactions on Electromagnetic Compatibility*, vol. EMC-23, no. 4, pp. 419–422, November 1981.
- [93] K. S. Yee, "A subgridding method for the finite difference time domain algorithm to solve Maxwell's equations", Tech. Rep. UCRL-96772, Lawrence Livermore National Laboratory, 1987.
- [94] J. C. Kasher and K. S. Yee, "A numerical example of a 2-D scattering problem using a subgrid", *Applied Computational Electromagnetics Society Journal and Newsletter*, vol. 2, no. 2, pp. 75–102, 1987.

- [95] M. J. Berger and J. R. Olinger, "Adaptive mesh refinement for hyperbolic partial differential equation", *Journal of Computational Physics*, vol. 53, pp. 484–512, 1984.
- [96] S.S. Zivanovic, K.S. Yee, and K.K. Mei, "A subgridding method for the time-Domain finite-Difference method to solve maxwell's equations", *IEEE Transactions on Microwave Theory and Techniques*, vol. 39, no. 3, pp. 471–479, Mar. 1991.
- [97] D. T. Prescott and N. V. Shuley, "A method for incorporating different sized cells into the finite-difference time-domain analysis technique", *IEEE Microwave Guided Wave Letters*, vol. 2, no. 11, pp. 434–436, November 1992.
- [98] J.W. Nehrbass and R. Lee, "Optimal finite-Difference sub-Gridding techniques applied to the helmholtz equation", *IEEE Transactions on Microwave Theory and Techniques*, vol. 48, no. 6, pp. 976–984, June 2000.
- [99] S. Wang, F. L. Texeira, R. Lee, and J.-F. Lee, "Optimization of two-dimensional subgridding schemes for the finite-difference time-domain method", in *International Conference on Electromagnetics in Advanced Applications (ICEAA 01)*, Torino, Italy, September 2001, pp. 121–124.
- [100] P. Thoma and T. Weiland, "A consistent subgridding scheme for the finite difference time domain method", *International Journal of Numerical Modelling*, vol. 9, pp. 359–374, 1996.
- [101] K. M. Krishnaiah and C. J. Railton, "Passive equivalent circuit of FDTD: An application to subgridding", *Electronics Letters*, vol. 33, no. 15, pp. 1277–1278, 1997.
- [102] K. M. Krishnaiah and C. J. Railton, "A stable subgridding algorithm and its application to eigenvalue problems", *IEEE Transactions on Microwave Theory and Techniques*, vol. 47, no. 5, pp. 620–628, May 1999.
- [103] M. J White and M. F. Iskander, "Development of a multigrid FDTD code for three-dimensional applications", *IEEE Transactions on Antennas and Propagation*, vol. 45, no. 10, pp. 1512–1517, October 1997.

- [104] M.J. White, Z. Yun, and M.F. Iskander, "A new 3-D FDTD multigrid technique with dielectric traverse capabilities", *IEEE Transactions on Microwave Theory and Techniques*, vol. 49, no. 3, pp. 422–430, Mar. 2001.
- [105] M.W. Chevalier, R.J. Luebbers, and V.P. Cable, "FDTD local grid with material traverse", *IEEE Transactions on Antennas and Propagation*, vol. 45, no. 3, pp. 411–421, Mar. 1997.
- [106] W. Yu and R. Mittra, "A new subgridding method for the finite-Difference time-Domain (FDTD) algorithm", *Microwave and Optical Technology Letters*, vol. 21, no. 5, pp. 330–333, June 1999.
- [107] M. Okoniewski, E. Okoniewska, and M. Stuchly, "Three-Dimensional subgridding algorithm for FDTD", *IEEE Transactions on Antennas and Propagation*, vol. 45, no. 3, pp. 422–429, Mar. 1997.
- [108] S. Chaillou, J. Wiart, and W. Tabbara, "A subgridding scheme based on mesh nesting for the ftd method", *Microwave and Optical Technology Letters*, vol. 22, no. 3, pp. 330–333, Aug. 1999.
- [109] S. Kapoor, "Sub-cellular technique for finite-difference time-domain method", *IEEE Transactions on Microwave Theory and Techniques*, vol. 45, no. 5, pp. 673–677, May 1997.
- [110] B. Beillard, Y. Chevalier, J. Andrieu, Y. Imbs, and B. Jecko, "Spatial subgridding in FDTD", *European Physical Journal. Applied Physics*, vol. 4, no. 3, pp. 297–302, 1998.
- [111] T.O. Körner and W. Fichtner, "Refractive index adaptive gridding for finite-Difference time-Domain methods", *International Journal of Numerical Modelling*, vol. 12, 1999.
- [112] P. Monk, "Sub-Gridding FDTD schemes", *ACES Journal*, vol. 11, no. 1, pp. 37–46, Mar. 1996.
- [113] P. Monk, "Error estimates for subgridded FDTD schemes", in *12th Annual Review of Progress in Applied Computational Electromagnetics*, Monterey, CA, March 1996, vol. 1, p. 619.
- [114] N. Chavannes, J. Fröhlich, H.-U. Gerber, and N. Kuster, "A robust FDTD local refinement scheme for general application to enhanced antenna analysis", *IEEE Transactions on Microwave Theory and Techniques*, Submitted, 2002.

- [115] A. Taflove and K. Umashankar, "A hybrid moment method/finite-difference time-domain approach to electromagnetic coupling and aperture penetration into complex geometries", *IEEE Transactions on Antennas and Propagation*, vol. 30, no. 4, pp. 617–627, April 1982.
- [116] P. H. Aoyagi, J.-F. Lee, and R. Mittra, "A hybrid Yee algorithm/scalar-wave equation approach", *IEEE Transactions on Microwave Theory and Techniques*, vol. 41, no. 9, pp. 1593–1600, September 1993.
- [117] R. Lee and T. T. Chia, "Analysis of electromagnetic scattering from a cavity with a complex termination by means of a hybrid-ray FDTD method", *IEEE Transactions on Antennas and Propagation*, vol. 41, no. 11, pp. 1560–1569, November 1993.
- [118] M. Mrozowski, "A hybrid PEE-FDTD algorithm for accelerated time domain analysis of electromagnetic waves in shielded structures", *IEEE Microwave Guided Wave Letters*, vol. 4, no. 10, pp. 323–325, October 1994.
- [119] M. Mrozowski, M. Okoniewski, and M. A. Stuchly, "Hybrid PEE-FDTD method for efficient field modelling in cylindrical co-ordinates", *Electronics Letters*, vol. 32, no. 3, pp. 194–195, 1996.
- [120] K. S. Yee and J. S. Chen, "Conformal hybrid finite difference time domain and finite volume time domain", *IEEE Transactions on Antennas and Propagation*, vol. 42, no. 10, pp. 1450–1455, October 1994.
- [121] D. J. Riley and C. D. Turner, "Interfacing unstructured tetrahedron grids to structured-grid FDTD", *IEEE Microwave Guided Wave Letters*, vol. 5, no. 9, pp. 284–286, September 1995.
- [122] A. Monorchio and R. Mittra, "A novel subgridding scheme based on a combination of the finite-element and finite-difference time-domain methods", *IEEE Transactions on Antennas and Propagation*, vol. 46, no. 9, pp. 1391–1393, September 1998.
- [123] A. R. Bretones, A. Monorchio, G. Manara, R. G. Martin, and R. Mittra, "Hybrid technique combining finite element, finite difference and integral equation methods in time domain", *Electronics Letters*, vol. 36, no. 6, pp. 506–508, 2000.

- [124] J. M. Tranquilla, M. Feng, H. M. Rizzo, and K. G. Clark, "A cartesian-cylindrical hybrid FD-TD analysis of composite microwave applicator structures", *Journal of Microwave Power and Electromagnetic Energy*, vol. 34, no. 2, pp. 97–105, 1999.
- [125] I. J. Craddock, D. L. Paul, C. J. Railton, G. Ball, and J. Watts, "Cylindrical-cartesian FD-TD model of a 17-element conformal antenna array", *Electronics Letters*, vol. 37, no. 24, pp. 1429–1431, 2001.

Part II

**Algorithms for FDTD Local
Mesh Refinement**

Seite Leer /
Blank leaf

Chapter 5

A Novel 3-D CPFDTD Scheme for Modeling Grid Non-Conformally Aligned Transmitter Structures

Abstract In this paper, a novel three-dimensional subcell algorithm for modeling metallic objects which are non-conformally oriented within the finite-difference time-domain grid is proposed. The generally applicable algorithm is based on the Contour-Path (CP) technique and enables, in combination with an enhanced non-conformally aligned source model, a more accurate spatial representation of antenna structures than the common staircase approach. To evaluate the performance of the new algorithm, the simulation results are compared with the classical staircase approach for dipole antennas as well as for a generic phone. Significant improvements were achieved for all antenna parameters from the near- and far-field, i.e., feedpoint impedance, radiation pattern and field distributions.

5.1 Introduction

The Finite-Difference Time-Domain (FDTD) method, originally presented by Yee [1] and greatly enhanced, e.g., in [2] and [3], has become the most

¹N. Chavannes and N. Kuster, "A novel 3-D CPFDTD scheme for modeling grid non-conformally aligned transmitter structures", *IEEE Transactions on Antennas and Propagation*, 2001 - to be published.

widely used technique in electromagnetic computations. Although the Method of Moment (MoM) techniques are still dominant in antenna analysis, FDTD is often the only suitable method when antennas are not isolated but embedded in complex dielectric and lossy environments [4, 5, 6, 7]. However, the conformal alignment of all parts of the antenna and source configurations is often not possible, e.g., the complex RF part of a mobile phone (PCB - matching network - multiband antennas), horn antennas, complex antenna arrays, etc. The classical staircasing approach for modeling these non-conformal parts can lead to significant uncertainties. Increasing the mesh density reduces the method inherent errors for grid non-orthogonal aligned media interfaces caused by the staircasing approximation [8], [9]. However, limited computational resources restrict the application of any dense grid refinement for particular cases.

In order to reduce these limitations and to generally increase the modeling flexibility within FDTD, a number of algorithms have been proposed which represent curved perfectly electrically conducting (PEC) structures different from staircase modeling:

1. The use of non-orthogonal coordinate systems or a globally unstructured mesh [10], [11]. These approaches overcome part of the modeling drawbacks; nevertheless they pose high efforts in the grid generation and increase the computational requirements by a multiple of the common rectilinear FDTD scheme.
2. A modification of the standard Yee equations by incorporation of static field solutions in the vicinity of the curved metallic surface [12].
3. Locally distorted meshes, i.e., modifications in the original Yee scheme, only have to be applied to cells which are in the immediate vicinity of the PEC object, which forms an excellent trade-off between invested computational resources and obtained accuracy. The Contour Path (CP) method for FDTD (CPFDTD) introduced in [13] has been broadly applied to reduce the uncertainties caused by staircasing for a wide range of open-domain applications.

Despite the known problems, FDTD has been widely used for the modeling of mobile transmitter structures like cellular telephones, e.g., [14]. In [15] the increased antenna length caused by the staircased representation has been partially compensated by introducing correction factors. However, this rather simple approach is not satisfactory, since even the insensitive far-field pattern shows a rotation compared to the conformally aligned model,

with errors of more than 25% for certain angles. The total radiated power behaves very sensitively with respect to the spatial discretization, leading to deviations of 20% for an FDTD cell size of $\lambda/33$.

To overcome these limitations, a novel approach is presented in this paper which extends the common CPFDTD scheme to general 3-D antenna structures which are arbitrarily rotated around the major cartesian axes. The modified CP scheme is not restricted to objects consisting of multiple mesh cells within its minimum spatial extensions but is applicable to thin structures of subcell dimensions, such as filaments and sheets of finite length. As will be discussed in section 5.2, the method's general availability was achieved by splitting up specific Yee grid edges, i.e., introducing virtual field components which are consequently used within the CP integration process. Furthermore, a novel source model is proposed which, in contrast to common approaches, allows an excitation of FDTD grid non-conformally aligned antenna configurations.

In section 5.3 the developed schemes are applied to a 3-D analysis of grid non-conformally aligned dipole antennas as well as a more complex generic phone model. In addition, all results are compared to a straightforward staircase approach and a conformally aligned reference calculation.

5.2 Numerical Methods

In contrast to the common FDTD algorithm, the CP method is not based on Maxwell's equations in differential form but in integral form using Ampère's and Faraday's laws, indicated as follows:

$$\oint_C \vec{H} \cdot d\vec{l} = \int \int_S (\vec{J}_C + \vec{J}_S) \cdot d\vec{S} + \frac{\partial}{\partial t} \int \int_S \vec{D} \cdot d\vec{S} \quad (5.1)$$

$$\oint_C \vec{E} \cdot d\vec{l} = -\frac{\partial}{\partial t} \int \int_S \vec{B} \cdot d\vec{S} \quad (5.2)$$

where \vec{J}_S and \vec{J}_C specify the source and the conduction current, respectively, while the contour C encloses the area S . Applied to a cartesian grid, both contours, i.e., for the magnetic field H and the electric flux density D , are chained. Ampère's and Faraday's law applied to a discretized grid use the same temporal updating scheme as the common FDTD algorithm. Therefore, the CP method has to be applied only to Yee cells which are in the closest vicinity of the PEC structure and therefore directly connected to the metallic object, e.g., the antenna.

5.2.1 3-D CP Modeling Of Wire Structures

Applying the developed CP based algorithms to thin wire antenna structures or PEC sheets requires adherence to the following rules:

1. The antenna has to be within a primary Yee grid plane but may be arbitrarily rotated around the cartesian FDTD axes.
2. The tips of the antenna must be located on a primary Yee grid line.
3. If a source is placed in the feedpoint region, it must be excited symmetrically according to the antenna's orientation.

Rule 2 has to be applied since all EM field information from the tip of the antenna is not transformable into the FDTD grid if the tip is located inside a Yee cell. A further local refinement of the grid around the antenna tip would have to be applied in this case.

Figure 5.1 depicts the position of such a non-conformally oriented thin wire structure of a dipole antenna within the FDTD grid. Specific electric field components (indicated by large arrows) cannot be computed by the Yee algorithm, since the corresponding magnetic components are located on opposite sides of the wire. These E-field components have to be deactivated and will be left unused. All those H-components located around the wire have to be determined by application of the CP updating equations based on Faraday's law, whereby only the wire non-tangential non-zero E-field components are used. Depending on the location of the antenna in the FDTD grid, different updating equations have to be applied. For the general case shown in figures 5.1 and 5.2 the corresponding update equations are split up in three groups summarized for each cartesian direction.

1. H_z field components:

Assuming no E-field contribution from the electric conducting subpath E_{tan} , the equations for the two H_z components

are as follows:

$$H_z \Big|_{i,j}^{n+\frac{1}{2}} = H_z \Big|_{i,j}^{n-\frac{1}{2}} + \frac{\Delta t}{\mu_0(A_1 + A_{c1})} (l_{y1} E_y \Big|_{i,j}^n + l_x E_x \Big|_{i,j+1}^n - l_{y2} E_y \Big|_{i+1,j+1}^n) \quad (5.3)$$

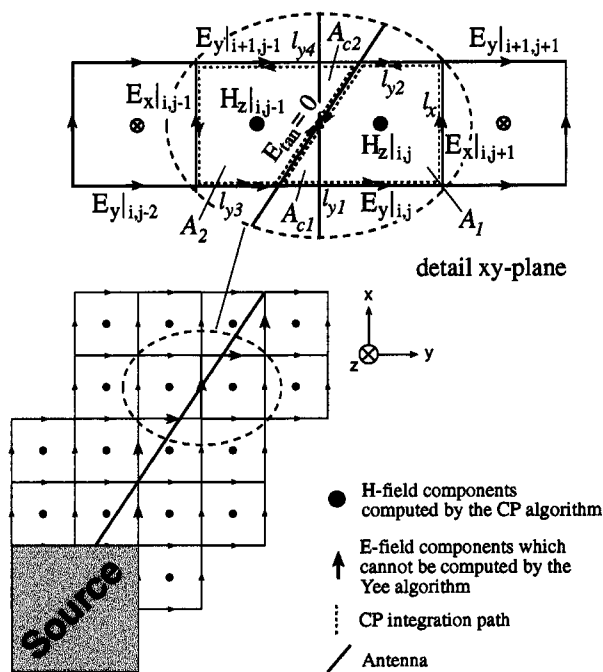


Figure 5.1: CP method applied to a non-conformally oriented thin wire structure of a dipole antenna in the xy-plane (determination of H_z component).

$$H_z \Big|_{i,j-1}^{n+\frac{1}{2}} = H_z \Big|_{i,j-1}^{n-\frac{1}{2}} + \frac{\Delta t}{\mu_0(A_2 + A_{c2})} (l_{y3} E_y \Big|_{i,j-2}^n - l_x E_x \Big|_{i,j-1}^n - l_{y4} E_y \Big|_{i+1,j-1}^n) \quad (5.4)$$

where A_1 and A_{c1} form the total area within the contour enclosing $H_z \Big|_{i,j}$ and A_2 and A_{c2} express the corresponding area for $H_z \Big|_{i,j-1}$. The particular lengths on each side of the antenna within the integration path in the y -direction are indicated by the elements l_{y1} to l_{y4} . l_x signifies the Yee cell extension in the x -direction. All three E-field components (E_x and E_y) which are affected by the presence of the antenna are deactivated and not taken into account. However, these two E_y components are needed for the CP integration. Therefore a so

called *collinear borrowing* is performed, whereby their collinear nearest neighbor components $E_y \Big|_{i,j-2}^n$ and $E_y \Big|_{i+1,j+1}^n$ are used instead.

2. H_x field components:

For the determination of the affected H_x components, figure 5.2 shows a part of the scenario within the FDTD grid. Since some of the electric field components placed within the primary Yee grid plane (index k) have been deactivated, all H_x components located above and below have to be calculated using modified equations. Thereby an E_y -field segment at index k from each side of the antenna is introduced into the CP as follows:

$$\begin{aligned} H_x \Big|_{i,j-1,k-1}^{n+\frac{1}{2}} &= H_x \Big|_{i,j-1,k-1}^{n-\frac{1}{2}} + \\ &\frac{\Delta t}{\mu_0 l_y l_z} \left(-l_z E_z \Big|_{i,j,k-1}^n - l_y E_y \Big|_{i,j-1,k-1}^n + \right. \\ &\left. l_z E_z \Big|_{i,j-1,k-1}^n + l_1 E_y \Big|_{i,j-2,k}^n + l_2 E_y \Big|_{i,j,k}^n \right) \end{aligned} \quad (5.5)$$

$$\begin{aligned} H_x \Big|_{i+1,j,k-1}^{n+\frac{1}{2}} &= H_x \Big|_{i+1,j,k-1}^{n-\frac{1}{2}} + \\ &\frac{\Delta t}{\mu_0 l_y l_z} \left(-l_z E_z \Big|_{i+1,j+1,k-1}^n - l_y E_y \Big|_{i+1,j,k-1}^n + \right. \\ &\left. l_z E_z \Big|_{i+1,j,k-1}^n + l_4 E_y \Big|_{i+1,j-1,k}^n + l_3 E_y \Big|_{i+1,j+1,k}^n \right) \end{aligned} \quad (5.6)$$

where l_1 to l_4 indicate parts of a Yee cell length in the y -direction which have been separated by the presence of the antenna, i.e., which are located on different sides of the antenna. l_y and l_z are the Yee cell extensions in the y - and z -directions, respectively. The remaining values $H_x \Big|_{i,j-1,k}$ and $H_x \Big|_{i+1,j,k}$ are determined in precisely the same way.

3. H_y field components:

The determination of the H_y components is depicted in figure 5.2 as well. The electric field component in the y -direction, which is separated by the antenna wire, cannot be computed by the common Yee algorithm, but is needed in order to calculate the two H_y components

($H_y|_{i,j,k-1}, H_y|_{i,j,k}$). Moreover, the E-field vector has opposite spatial directions depending on the side of observation with respect to the PEC wire. Therefore, the E-field component has to be split up into two subparts, E_1 and E_2 . If the antenna is oriented at a very flat angle with respect to the x -direction, multiple neighboring collinear E_x components are influenced by the PEC. Thus it is not possible to assess the values for E_1 and E_2 by a collinear borrowing of the collinear electric Yee grid components.

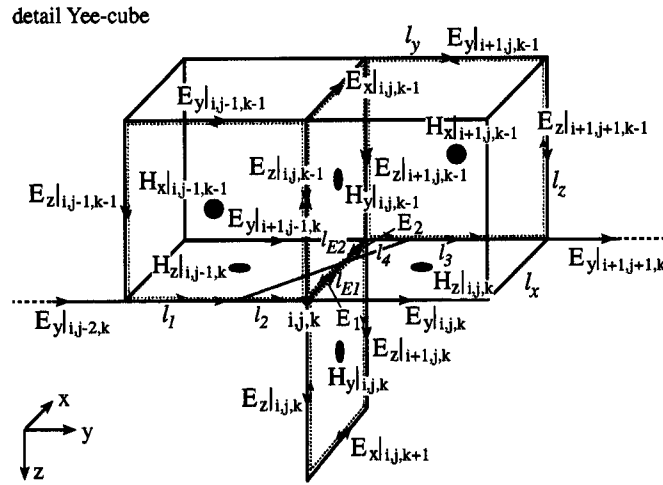


Figure 5.2: 3-D illustration of the CP method used to determine the H_x and H_y components located above and below the antenna.

In order to consequently extract the field components E_1 and E_2 , a novel method related to a scheme shown in [16] is proposed. Faraday's law is applied to the reduced areas A_1 and A_2 surrounded by the corresponding integration paths. Using these contour paths, equations 5.3 and 5.4 are modified as follows:

$$H_z \Big|_{i,j}^{n+\frac{1}{2}} = H_z \Big|_{i,j}^{n-\frac{1}{2}} + \frac{\Delta t}{\mu_0 A_1} (l_y E_y \Big|_{i,j}^n + l_x E_x \Big|_{i,j+1}^n - l_y E_y \Big|_{i+1,j+1}^n - l_{E1} E_1) \quad (5.7)$$

$$H_z \Big|_{i,j-1}^{n+\frac{1}{2}} = H_z \Big|_{i,j-1}^{n-\frac{1}{2}} + \frac{\Delta t}{\mu_0 A_2} (l_{y3} E_y \Big|_{i,j-2}^n - l_x E_x \Big|_{i,j-1}^n - l_y E_y \Big|_{i+1,j-1}^n - l_{E2} E_2) \quad (5.8)$$

l_{E1} and l_{E2} indicate the length of the subpath for E_1 and E_2 , respectively.

E_1 and E_2 are now extracted by setting the right side terms of equations 5.3 and 5.7 as well as equations 5.4 and 5.8 to equality.

$$E_1 = \frac{1}{l_{E1}} (l_{y1} E_y \Big|_{i,j,k}^n - l_{y2} E_y \Big|_{i+1,j+1,k}^n + l_x E_x \Big|_{i,j+1,k}^n) - \frac{\mu_0(A_1 - AC_1)}{l_{E1}\Delta t} (H_z \Big|_{i,j,k}^{n+\frac{1}{2}} - H_z \Big|_{i,j,k}^{n-\frac{1}{2}}) \quad (5.9)$$

$$E_2 = \frac{1}{l_{E2}} (-l_{y4} E_y \Big|_{i+1,j-1,k}^n + l_{y3} E_y \Big|_{i,j-2,k}^n - l_x E_x \Big|_{i,j-1,k}^n) + \frac{\mu_0(A_2 - AC_2)}{l_{E2}\Delta t} (H_z \Big|_{i,j-1,k}^{n+\frac{1}{2}} - H_z \Big|_{i,j-1,k}^{n-\frac{1}{2}}) \quad (5.10)$$

The results obtained from equations 5.9 and 5.10 are consequently used to calculate $H_y \Big|_{i,j,k-1}^{n+\frac{1}{2}}$ as follows:

$$H_y \Big|_{i,j,k-1}^{n+\frac{1}{2}} = H_y \Big|_{i,j,k-1}^{n-\frac{1}{2}} + \frac{\Delta t}{\mu_0 l_x l_z} (-l_z E_z \Big|_{i,j,k-1}^n + l_x E_x \Big|_{i,j,k-1}^n + l_z E_z \Big|_{i+1,j,k-1}^n - l_{E1} E_1 - l_{E2} E_2) \quad (5.11)$$

The $H_y \Big|_{i,j,k}^{n+\frac{1}{2}}$ component located below the index k primary Yee grid plane is determined in the same manner as just indicated in equation 5.11. All remaining E- and H-field components located around the wire antenna which have not been mentioned within this section 5.2.1 are calculated using the common Yee updating scheme.

5.2.2 3-D CP Modeling of Extended Solid Objects

The CP modeling of a non-conformally oriented perfectly conducting box can be performed analogously to the wire using slightly modified updating equations. Figure 5.3 shows a detailed view of the phone box rotated in the xy-plane of the cartesian Yee grid. By taking into consideration that the PEC structures do not contribute to the CP integral, equations 5.12 and 5.13 are used to determine those H_x components which are influenced by the boundary structure of the box.

$$\begin{aligned}
 H_x \Big|_{i,j,k-1}^{n+\frac{1}{2}} &= H_x \Big|_{i,j,k-1}^{n-\frac{1}{2}} + \\
 &+ \frac{\Delta t}{\mu_0 A} \left(-l_z E_z \Big|_{i,j+1,k-1}^n - l_s E_y \Big|_{i,j+1,k-1}^n + \right. \\
 &\quad \left. l_s E_y \Big|_{i,j+1,k}^n \right)
 \end{aligned} \tag{5.12}$$

$$\begin{aligned}
 H_x \Big|_{i,j,k}^{n+\frac{1}{2}} &= H_x \Big|_{i,j,k}^{n-\frac{1}{2}} + \\
 &\frac{\Delta t}{\mu_0 l_y l_z} \left(-l_z E_z \Big|_{i,j+1,k}^n - l_s E_y \Big|_{i,j+1,k}^n + \right. \\
 &\quad \left. l_z E_z \Big|_{i,j,k}^n + l_y E_y \Big|_{i,j,k+1}^n \right)
 \end{aligned} \tag{5.13}$$

A indicates the area within the contour enclosing $H_x \Big|_{i,j,k-1}$ and l_s is the length of the subpath adjacent to the PEC phone box. l_y and l_z express the spatial extension of the FDTD grid cells in the y - and z -directions, respectively.

The updating process for the modified H_z and H_y components is similar to the scheme described in equations 5.3 and 5.4 as well as equations 5.7 to 5.11. In contrast to the modeling of PEC wire structures, the 3-D CP method applied to entire solid regions allows the neglect of a large number of magnetic field components which are within the PEC.

The CP method retains the ability to model solid edges located arbitrarily inside a Yee-cell, since all information about the geometry is lost for a missing context between flux and E-field integration path. Therefore, a slightly modified edge approximation is used as depicted in figure 5.4. The original geometry of the phone (thick dashed line) was corrected to a modified shape (grey line with arrow) which enables the modeling of the edge region with the CP approximation. The affected H_z components can be updated as described in section 5.2.1.

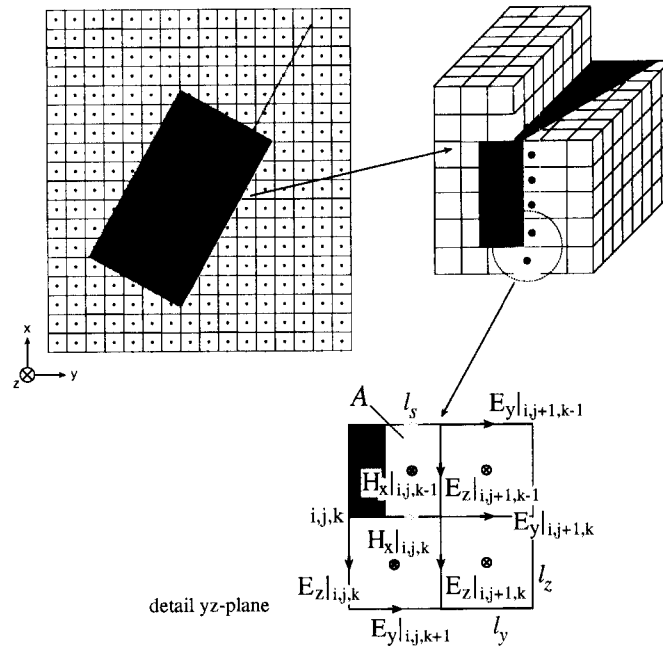


Figure 5.3: 3-D illustration of the CP method applied to a non-conformally oriented perfectly conducting box of a generic phone.

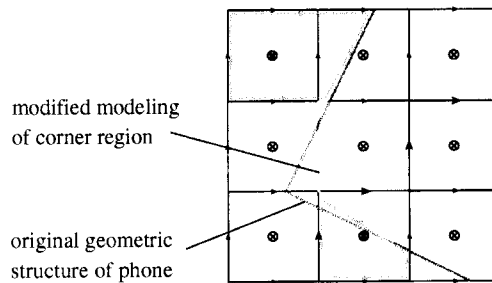


Figure 5.4: Modified edge approximation due to the inability of an accurate modeling of in-cell located corner regions.

5.2.3 Modeling of the Source

For non-conformally aligned active radiating antenna structures in particular, it is of great importance to achieve an improved representation of the

source within FDTD. On the contrary to grid conformally aligned antennas, the excitation of just one single FDTD edge can no longer be applied, since the excitation must be adapted to the orientation of the transmitter. Not following this kind of approach leads to an incorrect coupling between source and antenna, which results in unacceptable field distributions within the whole computational domain.

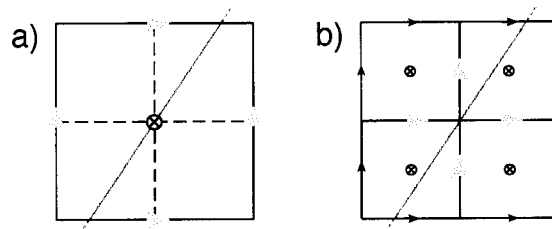


Figure 5.5: FDTD grid non-conformally aligned source modeling using distributed excitations: a) squarewise oriented; b) starwise oriented.

Three different approaches have been evaluated in order to achieve an appropriate source modeling:

1. Square-like distributed excitations:

For this source type all four electric field components located in a plane of the primary grid around a magnetic component are excited as shown in figure 5.5a). Both horizontally and vertically aligned components are weighted with the *sine* and the *cosine* function of the intermediate angle in order to achieve an orientation of the excitation conformal to the antenna's rotation. Due to the widely arranged spatial extension of the exciting components as well as major simplifications within the *sine/cosine* weighting approach, this source type results in a strongly swirled reactive near-field behavior which rotates the far-field by up to 10%. Furthermore, the mismatched coupling from the source to the antenna leads to increased radiated power compared to the conformally aligned structure.

2. Star-like distributed excitations:

This approach uses a *sine/cosine* weighting as already explained in the previous section using four electric field components oriented starwise around the intersection of two primary grid lines as shown in figure

5.5b). This results in improved near- and far-field behavior, i.e., a less swirled reactive near-field and a much closer agreement of the radiation pattern compared to the conformally aligned dipole antenna. However, in the close vicinity of the feedpoint region much higher E-field values than for the conformal excitation are obtained. The resulting absolute E-field distribution in the source of a dipole antenna rotated by 30° is compared to a conformally aligned model as shown in figures 5.6a) and 5.6c).

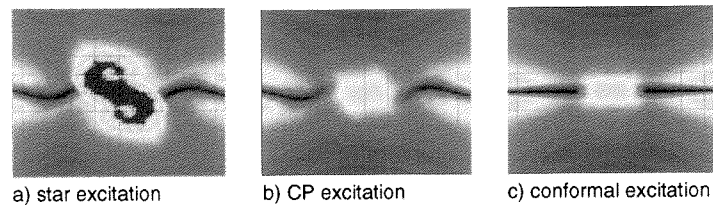


Figure 5.6: Comparison of source modeling techniques: distribution of absolute E-field in source region of dipole antenna rotated by 30° .

3. Contour Path excitation model:

In this approach none of the electric field components is excited directly as in the previous cases. Instead, a temporal variable E-field along the antenna axis in the feedpoint region is assumed. This assumption allows the appropriate magnetic field components to be determined by introducing the source signal $f(t)$ via a Faraday integration path during H-field updating. The procedure is similar to the CP method explained in section 5.2.1, using equations 5.3 and 5.4 in contrast to a tangential E-field value E_{tan} being equal to $f(t)$ instead of equal to zero. In figure 5.7 the CP excitation model is depicted. Whereas for both horizontally aligned E_{y1} and E_{y2} components in the source region the common Yee scheme is applied, those E- and H-field components which are disturbed by the presence of the antenna have to be determined using a modified updating scheme as follows:

- E_{y3} , E_{y4} : determination by collinear borrowing from linear collocated E_y neighboring components.
- H_{x1} to H_{x4} : determination similar to section 5.2.1.
- E_{x1} to E_{x2} : determination by projection of E_{tan} on the x-axis, i.e., multiplication of the E_{tan} value by $\cos(\beta)$.

This novel CP excitation model leads to good agreement between the rotated radiating structures and their conformally aligned equivalents with respect to near- and far-field behavior. Comparing the E-field in figure 5.6b) to the conformal orientation in figure 5.6c), a significant improvement was achieved, whereby the star-like excitation exceeds the ratio of applicability.

A weighted source modeling leads to unacceptable results for the staircase approach as well. Therefore, in order to be able to perform a meaningful comparison between staircasing and the CP approach, the developed CP excitation model was applied for all non-conformal simulations.

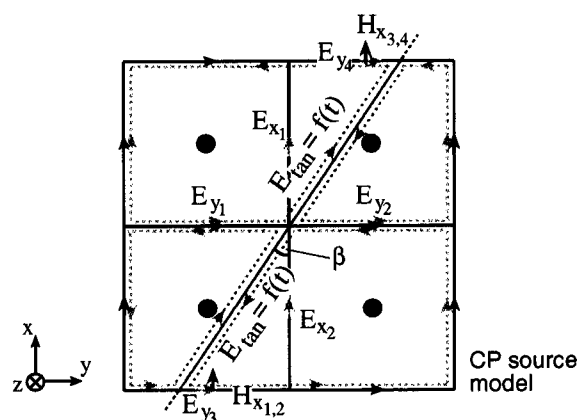


Figure 5.7: Improved modeling of a non-conformally aligned source region by applying the CP approach. This approach leads to an E-field distribution similar to the distribution of a reference source oriented conformally to the grid.

5.2.4 Stability Considerations

The common Yee scheme for non-dispersive, isotropic and lossless media has analytically proven to be stable using different approaches [17], [18]. For modified schemes such as the CPFDTD method this stability criterion is no longer valid as shown, e.g., in [19] and [20]. Due to the use of a non-causal and non-reciprocal collinear nearest neighbor approximation for the

deactivated E-field components (section 5.2.1), spuriously generated energy is introduced into the system, which leads to late-time instabilities within the analysis of closed and lossless resonant structures [20], [21].

The main target of the novel methods proposed in this paper is the analysis of transmitter structures interacting with lossy environments. For this kind of open boundary problem no such instabilities were obtained, since potentially generated spurious energy is attenuated by the absorbing boundaries, making the schemes well suitable for this kind of application.

However, in order to widen the method's capabilities to closed resonant structures, a scheme initially proposed in [21] and extended in [22] was evaluated. Its approach reconstitutes the lost reciprocity by performing a forced coupling between certain electric and magnetic field components applied to spatially extended PEC objects, e.g., the phone box. Within a setup as shown in figure 5.1, the $H_z|_{i,j}$ component is calculated using $E_y|_{i+1,j+1}$ by conformal borrowing, whereby this E-field component itself does not take into account $H_z|_{i,j}$ for its determination. The proposed stabilized approach involves the H-field component in the E-field updating process by weighting the length of its integration paths along $E_y|_{i+1,j+1}$:

$$\begin{aligned}
 E_y|_{i+1,j+1,k}^{n+\frac{1}{2}} &= E_y|_{i+1,j+1,k}^{n-\frac{1}{2}} + \\
 &\frac{\Delta t}{\epsilon_0 l_x} \left(\frac{1}{l_y+l_y2} [l_y2 H_z|_{i,j,k}^n + l_y H_z|_{i,j+1,k}^n] - \right. \\
 &\left. H_z|_{i+1,j,k}^n \right) + \frac{\Delta t}{\epsilon_0 l_z} \left(H_x|_{i+1,j+1,k}^n - H_x|_{i+1,j+1,k-1}^n \right) \quad (5.14)
 \end{aligned}$$

All terms correspond to variables which are depicted in illustrations 5.1 and 5.2.

Although this approach leads to an improved stability within closed resonant structures, it turned out to be much more difficult to develop a proper excitation modeling for open and lossy environments as discussed in section 5.2.3.

5.3 Results and Validation

The novel methods for CP and source modeling were compared to a straightforward staircase approach on the basis of perfectly conducting rotated dipole antennas and a previously described well characterized generic phone which was presented in [23]. There the results for the generic phone were validated by measurements using the near-field scanning system DASY3 [24]. The following antenna parameters were regarded for validation purposes:

- radiation characteristics
- near-field distribution
- feedpoint impedance

Since the source region is the most sensitive part for antenna modeling within FDTD, the determination of the feedpoint impedance turned out to be difficult, particularly for rotated sources, as explained in section 5.3.1. Therefore, in order to be able to perform a reliable comparison, all results are normalized to the total radiated power of the reference model. This model was chosen to have the same geometric structure as the rotated example, but was positioned conformally aligned to the FDTD grid. All electromagnetic field data in the vicinity of the rotated transmitter structure was recorded on an interpolated virtual conformally aligned grid to perform a direct comparison with the reference model in the postprocessing stage. The radiation pattern has been assessed using the near-to-far-zone transformation described in [25].

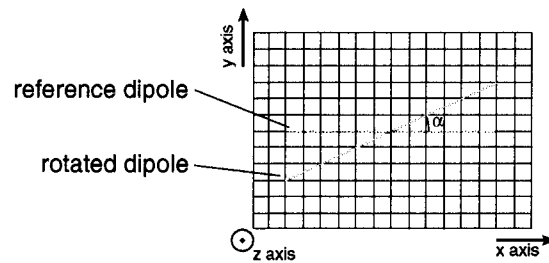


Figure 5.8: Dipole antenna located in the FDTD primary plane rotated by the angle α .

5.3.1 Dipole Antenna

The dipole antenna which was placed in the FDTD primary plane was modeled with a length of $\frac{\lambda}{2}$ at the frequency $f = 900$ MHz and was rotated by the angles $\alpha = 7^\circ, 20^\circ, 30^\circ$ and 40° , as depicted in figure 5.8. In order to match the location of the antenna tips with the FDTD grid nodes, the dipoles have slightly different lengths with respect to the four rotation angles examined. However, the length of the non-conformally modeled and reference dipoles was kept constant for a specific rotation angle to enable a meaningful comparison between the different methods. The computational domain

consisted of 160^3 cells using a homogeneous meshstep of 5 mm, which corresponds to an extension of 2.5λ in each spatial cartesian direction. For the absorbing boundary condition (ABC) a perfectly matched layer (PML) approximation [26] with a layer thickness of 8 was applied. The excitation at the feedpoint was modeled as described in section 5.2.3 with a smoothly increasing sinusoidal 900 MHz signal for the harmonic and a Gaussian sine pulse (bandwidth $B = 3$ GHz) for the transient simulations.

The validation of the radiation pattern revealed that the computation of the far-field seems to be insensitive with respect to modeling a simple dipole antenna, since very good agreement with the reference antenna was obtained for both methods. Comparison with the analytical results showed very low maximum deviations of 1.5% and 0.5% for the ϕ and θ components, respectively. These deviations may occur due to the representation of a finite antenna thickness within FDTD compared to an infinitesimal wire in the analytical solution.

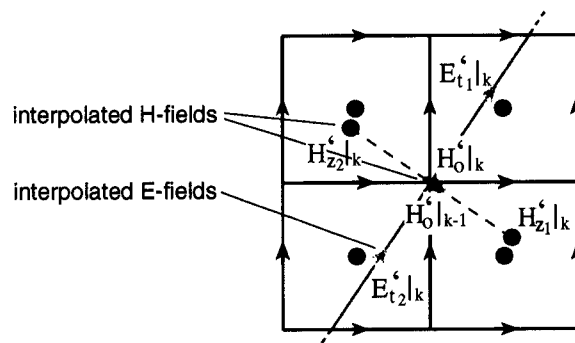


Figure 5.9: Determination of the feedpoint impedance by interpolation of electric and magnetic field values in the source region.

For the determination of the feedpoint impedance different approaches have been validated, whereby the calculation of voltage U and current I by use of symmetrically arranged and interpolated E- and H-field values adapted to the rotated structure in the feedpoint region turned out to be the most accurate method. Figure 5.9 depicts the positions of all values which are interpolated from the surrounding electric and magnetic Yee field components in the source region.

Figure 5.10 shows the feedpoint impedance of the reference, CP and staircase modeled antennas rotated at both 7° and 20° in the frequency range from 600 MHz to 2.5 GHz. For all examined rotation angles a better

agreement was found by application of the CP method. The highly sensitive resonance frequency in particular shows strong deviations for the staircase modeled approximation. However, the determination of the feedpoint impedance implies specific uncertainties, since for larger rotation angles the distance of the interpolated values from the original field components in the Yee grid increases.

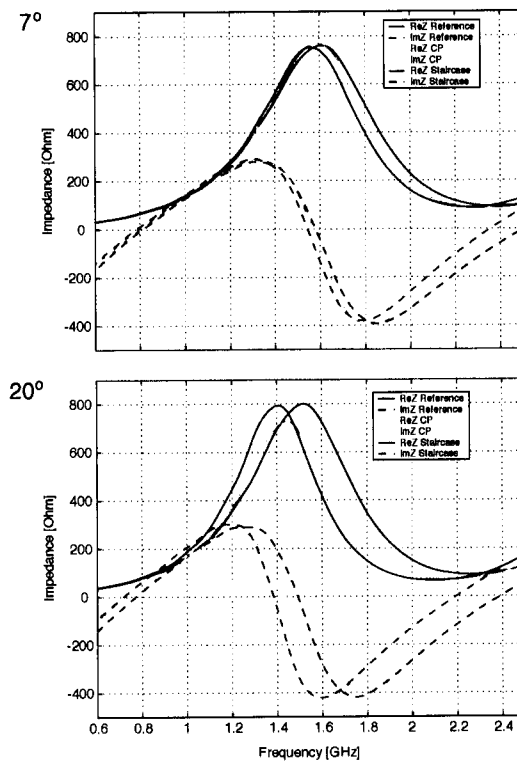


Figure 5.10: Feedpoint impedance of conformally oriented compared to 7° and 20° rotated dipole antennas as a function of the frequency.

For the comparison of the dipole antenna's near-field region the absolute values of E- and H-fields in the vicinity of the rotated antennas were recorded and compared to the conformally oriented reference model according to equation 5.15 for the electric field:

$$\left|err_{i,j}^E\right| [dB] = \left|20 \log_{10} \left(\frac{\left|E_{i,j}^{rot}\right|}{\left|E_{i,j}^{ref}\right|} \right)\right| \quad (5.15)$$

where $\left|err_{i,j}^E\right|$ is the error of the absolute electric field value at the Yee grid index i, j . $E_{i,j}^{rot}$ and $E_{i,j}^{ref}$ specify the E-field value for the rotated and the reference case, respectively. The deviation for the magnetic field is defined analogously. Figure 5.11 shows the error distribution of the electric field for a 40° rotated dipole antenna compared to the reference model. The observation plane which has been chosen has a spatial extent of $0.5\lambda \times 1\lambda$ at $f = 900$ MHz in the x - and y -directions and crosses the primary Yee grid plane within which the antenna is located. For all examined cases at the four rotation angles a better agreement is obtained for the CP modeled transmitter structure. Furthermore, the error is more restricted to the closest region of the antenna, as can be seen in the depicted example. For the staircase model the maximum error in the vicinity of the antenna exceeds 3 dB, whereas the CP case leads to deviations smaller than 0.5 dB.

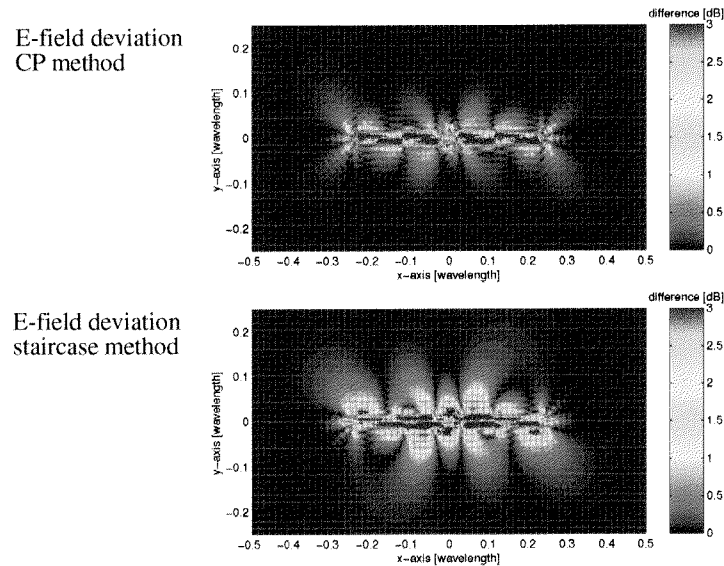


Figure 5.11: E-field distribution of a 40° rotated dipole antenna compared to the conformally oriented model.

5.3.2 Generic Phone

All parameters of the generic phone were validated at a rotation angle of $\alpha = 30^\circ$ analogous to the dipole antenna. Figure 5.12 shows the spatial dimensions of the phone and the mounted monopole antenna as well as a picture of the discretized model within the FDTD simulations. A homogeneous resolution of $3.8 \times 3.8 \times 3.8 \text{ mm}^3$ voxels was used in order to meet the rotated object's dimensions in the grid. For the ABC an eight layer PML was applied. The distance between boundary and phone was approximately λ . The source was modeled as described in the previous section but adapted to the geometry of the phone, i.e., part of the source region was ignored due to its location within the PEC of the phone box. As excitation the same signal forms as for the dipole antenna were used.

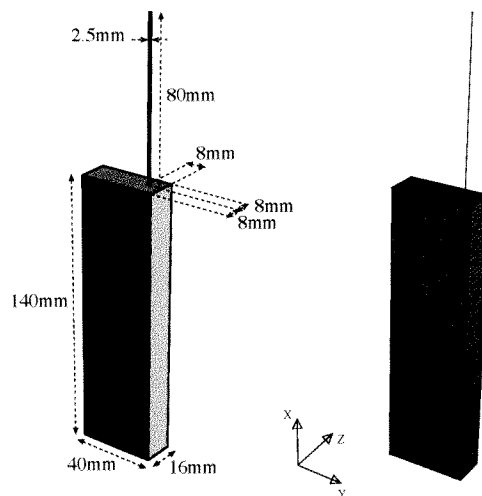


Figure 5.12: Geometric dimensions of the generic phone and its computer model within the FDTD simulations.

In Figure 5.13 the deviation of the radiation pattern for the CP and staircase approximations of the 30° rotated phone compared to the conventionally oriented reference model is shown. All E-fields were normalized to the radiated power of the reference phone. Contrary to the dipole antenna, for the more complex structure of the generic phone a better agreement is obtained using the CP modeling for both ϕ and θ angles. However, the far-field gain shows rather insensitive behavior with respect to grid non-conformal modeling.

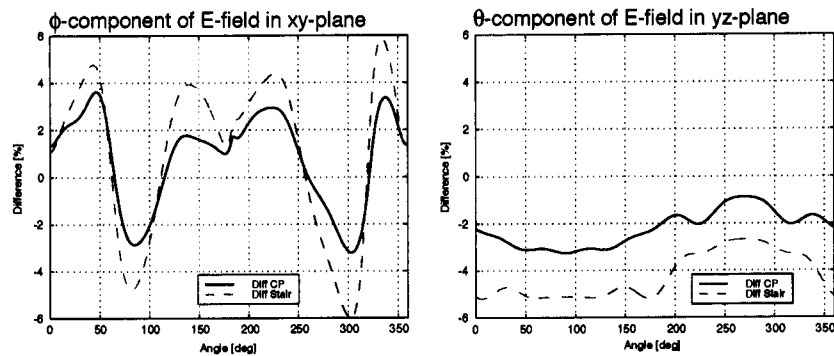


Figure 5.13: Difference in radiation patterns of a 30° rotated phone compared to the conformally oriented model.

2-D error distributions from the reference calculation for electric and magnetic fields are depicted in figures 5.14 and 5.15, respectively. The observation area is extended by about $0.5\lambda \times 1\lambda$ at $f = 900$ MHz in the x - and y -directions while the plane is located at 5 mm above the phone box. Low errors of less than 0.25 dB are obtained for the CP modeled phone in most of the regions observed, whereas the application of the staircasing approach leads to deviations larger than 2.5 dB in the reactive near-field region.

The feedpoint impedances of the two non-conformally aligned phone models are compared to the reference case in figure 5.16 for the frequency range from 500 MHz to 3 GHz. An obvious improvement results from the use of the CP approximation; the staircase approach leads to a strong frequency shift of about 100 MHz in the whole examined frequency band. Due to the presence of the PEC box, half the part of the source region is not considered for the excitation. Therefore, the determination of the feedpoint impedance by interpolation performs with increased accuracy for the phone example.

5.4 Conclusions

The proposed, implemented and tested locally conformal finite-difference scheme based on the CP approach enables improved spatial modeling of antennas, transmitter structures, etc. which are rotated within a FDTD grid plane. In order to represent an excitation with improved accuracy, a modified source model adapted to the geometry of non-conformally aligned transmitters was presented. The technique is computationally inexpensive,

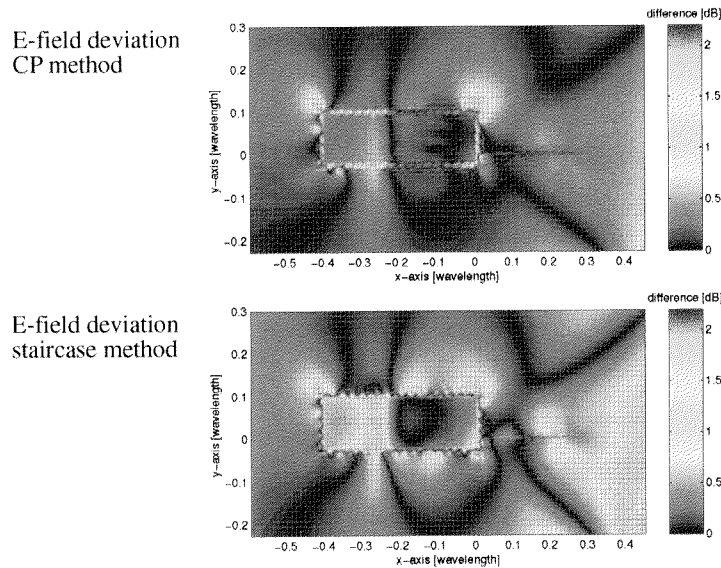


Figure 5.14: E-field distribution of a 30° rotated generic phone compared to the conformally oriented model at 5 mm above the phone box.

since only a small number of grid components are updated differently than the common FDTD scheme.

To assess the capabilities of the adapted CP method, the simulation of a dipole antenna and a generic phone was performed and compared to the staircased model. It was shown that, in general, the adapted CP approximation leads to more accurate results for all parameters, especially in the close near-field. This advantage is essential for accurate modeling of antenna structures embedded in complex lossy environments, e.g., for the assessment of absorption data.

Further improvement, especially for the feedpoint parameters, is expected with the combination of graded meshes and this technique. Extension of this approach to an arbitrary 3-D wire orientation is the topic of a subsequent research project. This can be performed by a trigonometric analysis in combination with incorporated static field solutions for all Yee components located around the antenna structure. In addition, the scheme's application range will be extended to resonant and closed structures as described in section 5.2.4.

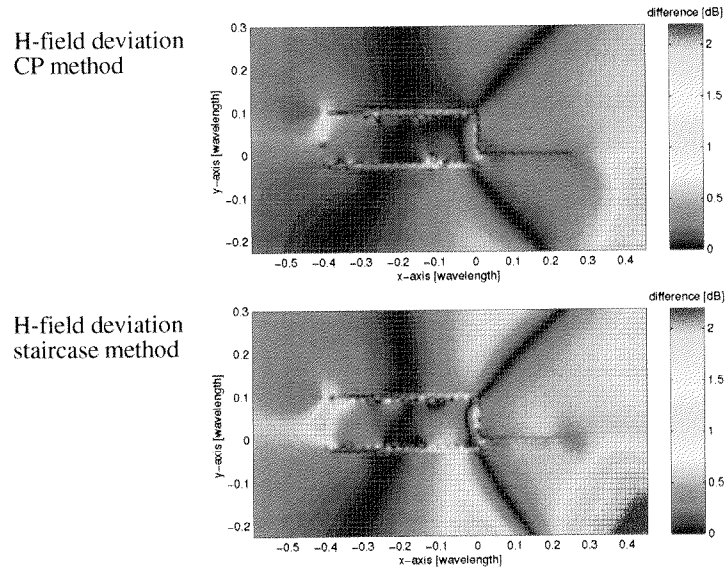


Figure 5.15: H-field distribution of a 30° rotated generic phone compared to the conformally oriented model at 5 mm above the phone box.

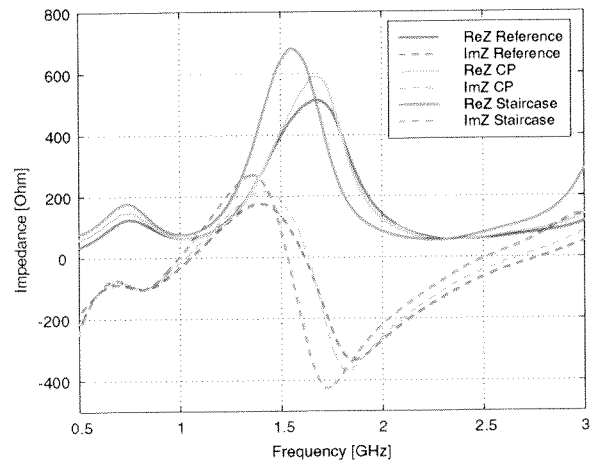


Figure 5.16: Feedpoint impedance of generic phone for reference, CP and staircase models as a function of the frequency.

5.5 Appendix

5.5.1 Subcell Contour-Path Modeling of Dielectric Structures in FDTD

In addition to grid non-conformally aligned thin PEC structures for which an enhanced modeling is proposed within this chapter, this section briefly outlines a CP based approach proposed in [13] which allows modeling curved dielectric material interfaces with improved accuracy. Figure 5.17 illustrates a setup consisting of an FDTD grid non-conformally aligned dielectric material transition (material 1: μ_1, ϵ_1 ; material 2: μ_2, ϵ_2). Different from the PEC case, this situation requires the tangential electric field E_{tan} at the interface boundary to be nonzero. In the same manner as performed for PEC structures, the magnetic field components located in the vicinity of the material transition (shown for $H_z|_{i,j}$ and $H_z|_{i+1,j}$) are calculated by application of Faraday's law using the contours (indicated by dotted lines) on each side of the transition.

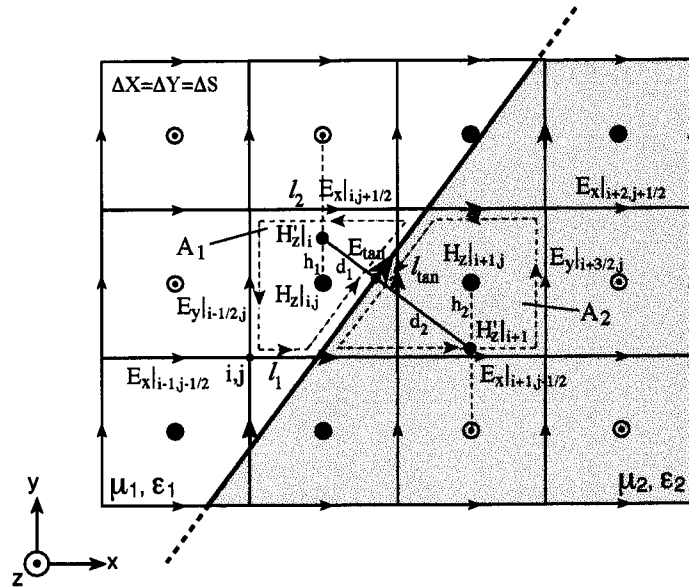


Figure 5.17: CPFDTD scheme using combined Faraday's and Ampère's law for improved modeling of grid non-conformally aligned dielectric material intersections (source: [13]).

All E-field components affected by the material interface (indicated by large arrows) are deactivated and kept unused for the updating process. For reasons of simplicity, a homogeneous mesh (grid step Δs) is considered. Both H-field components located in the xy-plane are consequently determined as follows:

$$H_z|_{i,j}^{n+\frac{1}{2}} = H_z|_{i,j}^{n-\frac{1}{2}} + \frac{\Delta t}{\mu_1 A_1} \left(\Delta s E_y|_{i-\frac{1}{2},j}^n - l_{tan} E_{tan}|^n + l_2 E_x|_{i,j+\frac{1}{2}}^n - l_1 E_x|_{i-1,j-\frac{1}{2}}^n \right) \quad (5.16)$$

$$H_z|_{i+1,j}^{n+\frac{1}{2}} = H_z|_{i+1,j}^{n-\frac{1}{2}} + \frac{\Delta t}{\mu_2 A_2} \left(l_{tan} E_{tan}|^n - \Delta s E_y|_{i+\frac{3}{2},j}^n - (2\Delta s - l_2) E_x|_{i+2,j+\frac{1}{2}}^n - (2\Delta s - l_1) E_x|_{i+1,j-\frac{1}{2}}^n \right) \quad (5.17)$$

where A_i and l_i indicate the area of the surface enclosed by the contour and the length of the subdivided path, respectively. l_{tan} is the length of the sub-path located on the material interface. Since both affected E-field components oriented in the x-direction have been previously deactivated, the collinear neighbors, i.e., $E_x|_{i-1,j-\frac{1}{2}}$ and $E_x|_{i+2,j+\frac{1}{2}}$ are *borrowed* for the contour path instead.

The determination of the tangential E-field component E_{tan} is performed by application of Ampère's law to the remaining perpendicular contour path:

$$E_{tan}|^{n+1} = E_{tan}|^{n-1} + \frac{\Delta t}{\varepsilon_1 d_1 + \varepsilon_2 d_2} \left(H_z'|_i^{n+\frac{1}{2}} - H_z'|_{i+1}^{n+\frac{1}{2}} \right) \quad (5.18)$$

using introduced virtual H-field components $H_z'|_i$ and $H_z'|_{i+1}$ which are assessed via linear interpolation from the corresponding H-field components:

$$H_z'|_i^{n+\frac{1}{2}} = \frac{(\Delta s - h_1) H_z|_{i,j}^{n+\frac{1}{2}} + h_1 H_z|_{i,j+1}^{n+\frac{1}{2}}}{\Delta s} \quad (5.19)$$

$$H_z'|_{i+1}^{n+\frac{1}{2}} = \frac{(\Delta s - h_2) H_z|_{i+1,j}^{n+\frac{1}{2}} + h_2 H_z|_{i+1,j-1}^{n+\frac{1}{2}}}{\Delta s} \quad (5.20)$$

where h_1 and h_2 are the spatial distances from the virtual H-field components to their neighbors determined via contour path. d_1 and d_2 refer to the distance of $H_z'|_i$ and $H_z'|_{i+1}$ from the material boundary.

The procedure shown is only derived for the 2-D case, but can be extended to three dimensions using the scheme developed within this chapter and discussed in section 5.2.1, i.e., by introducing virtual E-field components oriented in the y-direction at the location of E_{tan} . The values of these components are determined in the same manner, by recalculation from previously computed $H_z|_{i,j}$ and $H_z|_{i+1,j}$ but with incorporation of a reduced area A'_i which consequently enables the determination of H_x components located above and below.

References

- [1] K.S. Yee, "Numerical solution of initial boundary value problems involving Maxwell's equations in isotropic media", *IEEE Transactions on Antennas and Propagation*, vol. 14, pp. 302-307, 1966.
- [2] A. Taflove, *Computational Electrodynamics - The Finite Difference Time Domain Method*, Artech House, Norwood, MA, 1995.
- [3] D.M. Sullivan, *Electromagnetic Simulation Using The FDTD Method*, IEEE Press, Piscataway, NJ 008855-1331, 2000.
- [4] M.A. Jensen and Y. Rahmat-Samii, "EM interaction of handset antennas and a human in personal communications", *Proceedings of the IEEE*, vol. 83, no. 1, pp. 7-17, Jan. 1995.
- [5] A. Taflove, *Advances in Computational Electromagnetics: The Finite Difference Time Domain Method*, Artech House, Norwood, MA, 1998.
- [6] M. Okoniewski and M.A. Stuchly, "A study of the handset antenna and human body interaction", *IEEE Transactions on Microwave Theory and Techniques*, vol. 44, no. 10, pp. 1855-1864, Oct. 1996.
- [7] V. Hombach, K. Meier, M. Burkhard, E. Kühn, and N. Kuster, "The dependence of EM energy absorption upon human head modeling at 900 MHz", *IEEE Transactions on Microwave Theory and Techniques*, vol. 44, no. 10, pp. 1865-1873, Oct. 1996.
- [8] R. Holland, "Pitfalls of staircase meshing", *IEEE Transactions on Electromagnetic Compatibility*, vol. 35, no. 4, pp. 434-439, Nov. 1993.
- [9] A.C. Cangellaris and D.B. Wright, "Analysis of the numerical error caused by the stair-stepped approximation of a conducting boundary in fdtd simulations of electromagnetic phenomena", *IEEE Transactions on Antennas and Propagation*, vol. 39, no. 10, pp. 1518-1525, Oct. 1991.
- [10] P.H. Harms, J.F. Lee, and R. Mittra, "A study of the nonorthogonal fdtd method versus the conventional fdtd technique for computing resonant frequencies of cylindrical cavities", *IEEE Transactions on Microwave Theory and Techniques*, vol. 40, no. 4, pp. 741-746, Apr. 1992.
- [11] N.K. Madsen, "Divergence preserving discrete surface integral methods for Maxwell's curl equations using non-orthogonal unstructured

- grids", *Report UCRL-JC-109787, Lawrence Livermore National Laboratory*, 1992.
- [12] D.B. Shorthouse and C.J. Railton, "The incorporation of static field solutions into the finite difference time domain algorithm", *IEEE Transactions on Microwave Theory and Techniques*, vol. 40, pp. 986-994, 1992.
- [13] T.G. Jurgens, A. Taflove, K. Umashankar, and T.G. Moore, "Finite-difference time-domain modeling of curved surfaces", *IEEE Transactions on Antennas and Propagation*, vol. 40, no. 4, pp. 357-366, Apr. 1992.
- [14] M. Okoniewski and M. Stuchly, "Modeling of interaction of electromagnetic fields from a cellular telephone with hearing aids", *IEEE Transactions on Microwave Theory and Techniques*, vol. 46, no. 11, pp. 1686-1693, Nov. 1998.
- [15] P.S. Excell, P. Olley, and N.N. Jackson, "Modelling of an arbitrarily-oriented telephone handset in the finite-difference time-domain field computation method", *Jaces*, vol. 11, no. 2, pp. 55-65, 1996.
- [16] J. Fang and J. Ren, "A locally conformed finite-difference time-domain algorithm of modeling arbitrary shape planar metal strips", *IEEE Transactions on Microwave Theory and Techniques*, vol. 41, no. 5, pp. 830-838, May 1993.
- [17] A. Taflove and M.E. Brodwin, "Numerical solution of steady-state electromagnetic scattering problems using the time-dependent Maxwell's equations", *IEEE Transactions on Microwave Theory and Techniques*, vol. 23, pp. 623-630, Aug. 1975.
- [18] J.A. Pereda, L.A. Vielva, A. Vegas, and A. Prieto, "Analyzing the stability of the FDTD technique by combining the von Neumann method with the Routh-Hurwitz criterion", *IEEE Transactions on Microwave Theory and Techniques*, vol. 49, no. 2, pp. 377-381, Feb. 2001.
- [19] N.K.Madsen, "Divergence preserving discrete surface integral methods for maxwell's curl equations using nonorthogonal unstructured grids", *Tech. Rep. UCRL-JC-109787, Lawrence Livermore National Laboratory*, 1992.

- [20] M. Okoniewski, J. Anderson, J. Mrozowski, and S.S. Stuchly, "Arbitrarily located metal surfaces in FDTD technique", *Progress in Electromagnetics Research Symposium, Seattle, WA*, 1995.
- [21] I.J. Craddock, C.J. Railton, and J.P. McGeehan, "Derivation and application of a passive equivalent circuit for the finite difference time domain algorithm", *IEEE Microwave and Guided Wave Letters*, vol. 6, no. 1, pp. 40-42, 1992.
- [22] C.J. Railton and I.J. Craddock, "Stabilized CPFDTD algorithm for the analysis of arbitrary 3D PEC structures", *IEE Proceedings on Microwaves, Antennas and Propagation*, vol. 143, no. 5, pp. 367-372, Oct. 1996.
- [23] M. Burkhardt, N. Chavannes, K. Poković, T. Schmid, and N. Kuster, "Study on the FDTD performance for transmitters in complex environments", *Proceedings of the ICECOM, Dubrovnik*, pp. 83-86, Oct. 1997.
- [24] T. Schmid, O. Egger, and N. Kuster, "Automated e-field scanning system for dosimetric assessments", *IEEE Transactions on Microwave Theory and Techniques*, vol. 44, pp. 105-113, Jan. 1996.
- [25] A. Taflove and K.R. Umashankar, "Radar cross section of general three-dimensional structures", *IEEE Transactions on Electromagnetic Compatibility*, vol. 25, pp. 433-440, 1983.
- [26] J.P. Berenger, "A perfectly matched layer for the absorption of electromagnetic waves", *Journal of Computational Physics*, Oct. 1994.

Chapter 6

A Robust FDTD Local Refinement Scheme for General Application to Enhanced Antenna Analysis

Abstract A novel 3-D FDTD subgrid scheme is presented. It was developed under the objective of maximum stability, robustness as well as straightforward applicability within a CAD supported modeling environment. A novel temporal scheme based on interpolation in time, developed for this kind of multi-grid technique, shows superior performance compared to existing, extrapolation-based approaches. In addition, 3-D smoothing cubic splines are used for the spatial interpolation to enhance stability. This scheme has proven not only to be greatly robust but also highly efficient, since it may be staggered without losing stability for refinements tested up to 1:32. The performance of the implemented algorithm was benchmarked against high-resolution graded mesh modeling, with results obtained by MoM and GMT as well as by measurements. Furthermore, it has been demonstrated that the scheme can be utilized for automated grid generation combining subgrids with graded mesh within a state-of-the-art simulation platform, even for complex geometric structures.

¹N. Chavannes, J. Fröhlich, H.-U. Gerber and N. Kuster, "A robust FDTD local refinement scheme for general application to enhanced antenna analysis", *IEEE Microwave Theory and Techniques*, 2002 - to be published.

²This chapter addresses the theoretical part of the algorithm, whereas benchmarks and applications are presented in chapter 7.

6.1 Introduction

Within recent years, the Finite-Difference Time-Domain (FDTD) method has become the preferred technique for simulating a broad range of EM applications. The simple, straightforward and explicit scheme originally proposed by Yee in [1] has been greatly extended within pioneering efforts performed in [2], [3] and [4]. The scheme can be easily applied to complex problems, e.g., for antenna structures embedded within complex environments [5], [6], [7]. Nevertheless, restrictions in geometrical resolution due to computational limitations generally prevent meeting real-world engineering needs which often include highly detailed sub-objects within a largely extended space. In addition, the common Yee scheme represents a straightforward modeling of grid-non conformally aligned structures in a stair-stepped (*staircase*) approximation. Such spatially coarse modeling can introduce unacceptable errors, in particular for perfectly electric conducting (PEC) geometries [8], [9], as well as for dielectric structures [10].

A broad variety of methods have been proposed to reduce staircasing errors and to increase the mesh resolution within FDTD, including non-homogeneous (*graded*) meshes, local modifications of the rectilinear grid as well as subgrids.

Graded meshes [11], [12] are often applied to increase the FDTD grid resolution locally. Although being an elegant solution, their usage shows major disadvantages through waste of computational resources, since the grading expands through the entire width of the 3-D mesh. Moreover, the smallest cell used in the grid determines the global timestep which is applied throughout the entire computational domain. Furthermore, the variable mesh density introduces additional dispersion errors [13].

Improved efficiency is achieved by approaches which concentrate increased grid resolution to specific regions in the computational domain only. Schemes which modify the rectilinear FDTD cell structure, such as non-orthogonal coordinate systems [14] or subcell techniques [15], lead to strongly improved accuracy, but pose either high efforts in the grid generation or require a costly analysis of a complex object's shape.

A more general approach is the introduction of a subgrid. Subgrids are blocks of smaller mesh cells placed at specific locations of the computational domain without modifying the global mesh within the remaining space. Here the most crucial issue is the transfer of field information between coarse and fine grids. Schemes based on the Helmholtz Equation [16], [17] show a high efficiency, mainly for plane waves demonstrated on the basis of 2-D exam-

ples. A 3-D approach (1:2 refinement) based on curl and source matrices in the Finite-Integration (FI) technique [18] shows good behavior with respect to stability but therefore requires a reduction of the timestep determined by the Courant-Friedrichs-Lewy (CFL) criterion by a factor of 2. In [19] a method based on Ampère's law in integral form is presented which allows any integer refinement factor as well as dielectric material traversing the grid intersections. For a 1:3 refinement reflections from the subgrid boundaries in the range of more than -35dB have been reported. In [20] an efficient subgridding scheme applied to regions of different dielectric constants embedded into each other is proposed. The algorithm is derived for two dimensions and the refinement factor is determined by the ratio obtained for two adjacent dielectrics.

Significant improvements with respect to generalized applicability are achieved by methods based on spatial and temporal interpolation for the data transfer between coarse and fine grids as presented, e.g. in [21], [22], [23]. All three schemes provide good performance, however, [21] and [23] report of reflections in the range of -50dB ([21], 1:3 refinement, $\lambda/10$ cell size) as well as reductions of the maximum CFL to about 0.7 and 0.5 for grid refinements of 1:3 and 1:5, respectively. The schemes were tested and demonstrated to be stable for different numbers of timesteps (ts) (22 000 in [21], 2 500 in [23]). Excellent performance with respect to both low reflections and high stability is demonstrated in [22]. A nested mesh application of this scheme presented in [24] to model antenna structures like dipoles and helices shows errors up to 20% for certain configurations ($\lambda/2$ dipole at $f = 900$ MHz, $\lambda/300$ cell size, 1:16 refinement) in the closest vicinity of the antenna. Although the scheme is highly practical for a variety of configurations, [24] demonstrates an application range not particularly suited for antenna near-field analysis.

The objective of this paper was not only to improve existing subgridding algorithms with respect to performance but also to develop an algorithm which can be utilized within a state-of-the-art modeling environment for automatic generation of optimized grids.

6.2 Method

6.2.1 Spatial Interpolation Algorithm

The focus of the developed algorithm was on a smooth and stable transition between coarse and fine grids. Another important criterion was applicability within inhomogeneous material transitions. A small refinement factor of 2

was not considered as a disadvantage, since subgrids can easily be stepped sequentially or parallel when smooth and stable, leading to refinement factors of 2^n with $n \in \mathcal{N}^+$ which has been successfully tested for refinements up to 1:32.

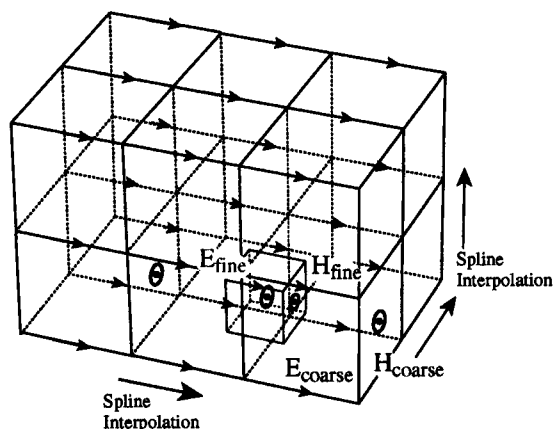


Figure 6.1: Arrangement of coarse grid, subgrid and spatial interpolation.

The best solution for temporal updating was achieved by a spatial positioning of the subgrid shifted by a quarter of the coarse grid's cell dimensions in each direction as proposed in [22], which leads to the smoothest transition, since all magnetic fields of the coarse as well as the fine mesh are collocated in a way simplifying spatial interpolation. The mesh step does not have to be modeled equidistant for the entire 3-D subgrid but for each cartesian direction. Figure 6.1 depicts a detailed view of this setup with a single subgrid cell placed into a $3 \times 2 \times 2$ coarse grid structure while E_{coarse} and E_{fine} are the electric field components in the coarse and the fine grids, respectively. H_{coarse} and H_{fine} indicate the corresponding magnetic field components in the two coupled grids. For the exchange of information between the two grids a novel scheme is proposed. It uses the electric and magnetic field components in the most external surface of the subgrid for information transfer from the coarse to the fine grid. The magnetic field components inside the inner subgrid region are used for the transfer in the opposite direction.

For the determination of the E_{fine} -field components in the transition region, a 3-D cubic spline scheme was taken into consideration due to reported low reflections [22]. For certain cases, particularly in the initial propagation

stage, the basic interpolating cubic spline leads to over- and underestimated values. A spline can be slightly smoothed to decrease the amount of misestimation and therefore further reduce instabilities:

$$S(p) = p \sum_i \{y_i - f(x_i)\}^2 + (1 - p) \int f''(x)^2 \quad (6.1)$$

where $f(x)$ defines a cubic spline through a series of (x_i, y_i) data points. The curve which minimizes $S(p)$ is known as a cubic smoothing spline [25] with p as smoothing parameter which controls the trade-off between minimizing the residual error and minimizing local variation. Figure 6.2 illustrates a possible situation with a series of four data points at $x = 1, 2, 3, 4$ and corresponding field values $y = 0, 0, 2, 1$. While the interpolating cubic spline leads to a strong underestimation in the range between $x = 1..2$, the smoothing cubic spline ($p = 0.98$) reduces this underestimation of the base values.

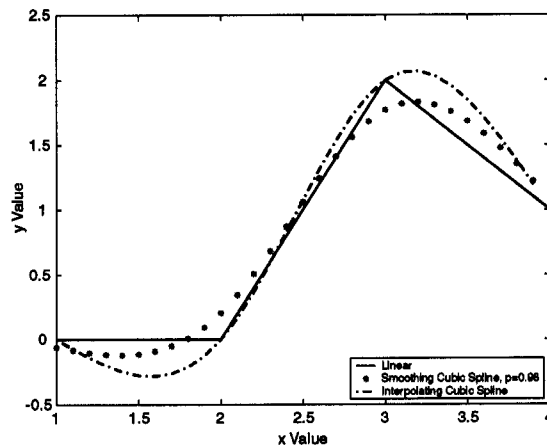


Figure 6.2: 3-D Spatial Interpolation: linear, interpolating and smoothing cubic splines.

In figure 6.1 for each spatial direction three corresponding E_{coarse} components are used, which leads to a system of 27 field values for the interpolation in this case. In order to simplify the interpolation algorithm and to speed up the updating process, the procedure can be separated into 1-D, 2-D and 3-D interpolations as shown in figure 6.3. The magnetic H_{fine} components which are located in the inner transition region are determined by applica-

tion of 1-D or 2-D cubic splines on the correlated H_{coarse} -field components, depending on their position.

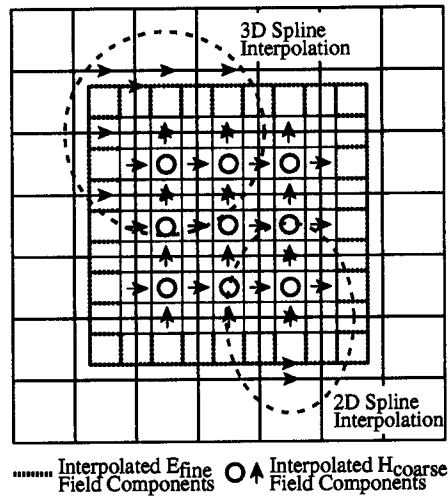


Figure 6.3: Interpolation method used depending on position of component.

6.2.2 Temporal Updating Scheme

Since the updating frequency in the subgrid is twice the one in the coarse grid, there will be some missing temporal information in the common FDTD updating scheme. Most of the proposed subgridding schemes use a temporal extrapolation to determine this information, since due to high refinement factors the missing components cannot be assessed from the coarse grid. Here a novel approach is presented which uses field data from the coarse grid at the current, past and the following time step to perform an interpolation in time. Figure 6.4 shows the detailed sequence of a full updating cycle. The determination of the temporal missing H_{fine} components at $t = n - \frac{1}{4}$ is shown in figure 6.5. For all cases where no PEC material traverses the transition region, a reduction factor of $0.95 dt_{max}$ allowed by the Courant criterion leads to stable solutions; otherwise a value of 0.9 was applied.

Steps performed at $t = n$:

1. Update of E_{coarse} at $t = n$ and H_{coarse} components at $t = n + \frac{1}{2}$ by basic Yee algorithm.

2. Apply spatial interpolation to determine all E_{fine} as well as H_{fine} components in border region (fig. 6.3, dotted).
3. Save E_{fine} and H_{fine} -field components located on surface for later use in step 4.
4. Determine E_{fine} at $t = n - \frac{1}{2}$ by 2nd order Taylor expansion using the E_{fine} at $t = n$ and from previous cycles at $t = n - 1$ and $t = n - 2$. Follow the same procedure to assess H_{fine} at $t = n - \frac{1}{4}$ using H_{fine} at $t = n + \frac{1}{2}$ and from previous cycles at $t = n - \frac{3}{4}$ and $t = n - \frac{3}{2}$.
5. Compute H_{fine} in border region at $t = n - \frac{1}{4}$ by Yee algorithm using E_{fine} from step 4, E_{fine} saved at $t = n - \frac{1}{2}$ and H_{fine} saved at $t = n - \frac{3}{4}$.
6. Average both values for H_{fine} at $t = n - \frac{1}{4}$ obtained within the last two steps using the factors optimized as described later in section 5.2.4, i.e., 0.349 and 0.651 for H-field interpolated values and indirect determination via the E-field, respectively.

Steps performed at $t = n + \frac{1}{4}$:

7. Apply Yee algorithm to compute all H_{fine} fields.
8. Save H_{fine} in border region (figure 6.3, dotted line).
9. Interpolate and store H_{coarse} located inside the fine grid (circles and thin arrows in figure 6.3) at $t = n + \frac{1}{4}$ from two collocated H_{fine} values.

Steps performed at $t = n + \frac{1}{2}$:

10. (Yee updating of the H_{coarse} components has already been performed in step 1).
11. Update E_{fine} fields by Yee algorithm.
12. Store all E_{fine} components located in the border region.

Steps performed at $t = n + \frac{3}{4}$:

13. Update all H_{fine} fields by the Yee algorithm.

14. The H_{coarse} components located inside the fine grid (circles and thin arrows in figure 6.3) are updated at $t = n + \frac{1}{2}$ with the field information from the fine grid (stored in step 8 and from current step).

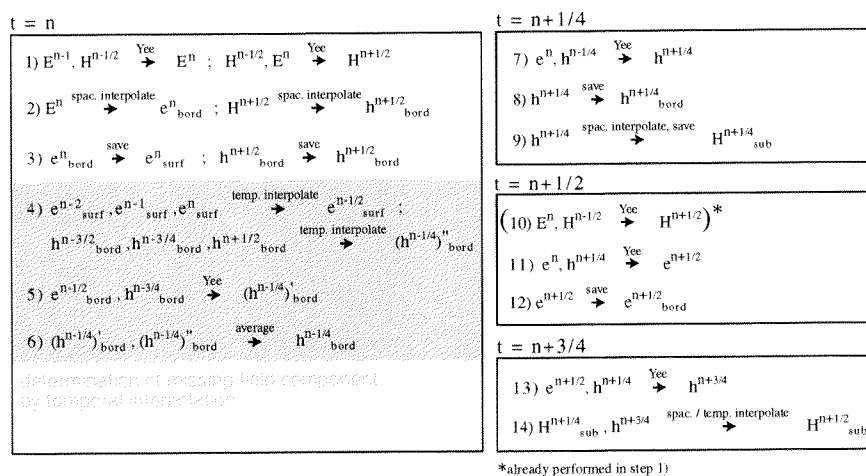


Figure 6.4: Detailed sequence of steps for a full updating procedure in the FDTD coarse and fine grid.

6.2.3 Special Treatment of Traversing PEC Materials

For the spatial interpolation in the transition region the spline scheme uses a set of three E_{coarse} components in each direction. For traversing PEC materials a special treatment of the interpolation algorithm has to be performed if at least one of the components is located inside the conductor. Therefore all affected components are determined using a slightly modified spline interpolation scheme which performs a 2-D or a 1-D spline interpolation depending on the localization of the cell for a virtually introduced E_{fine} component while including only those E_{coarse} components which are not located inside the conducting material as depicted in figure 6.6.

6.2.4 Integration Into a TCAD / Automeshing Environment

Any local refinement scheme is of limited application if it cannot be effectively integrated within and supported by an ergonomic user interface.

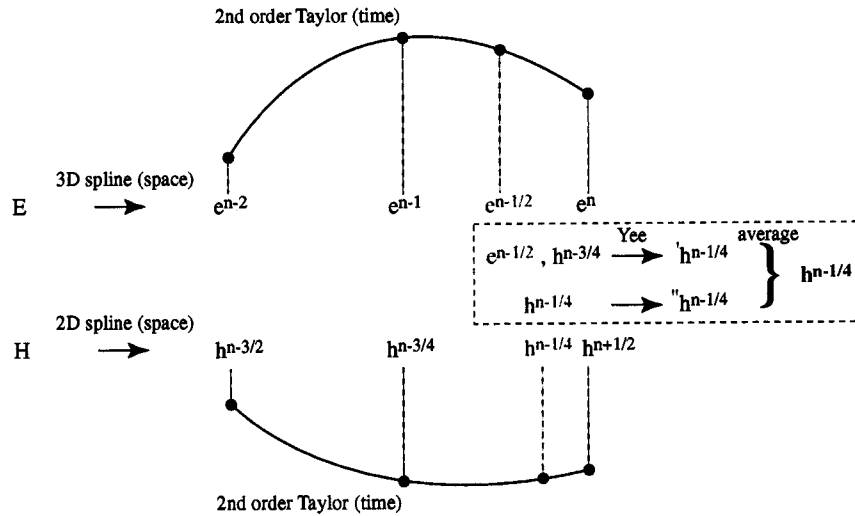


Figure 6.5: Temporal updating scheme: determination of missing $h^{n-1/4}$ component.

Only the combination of the three entities *TCAD*, *Subgrid* and *Automeshing* form the powerful instrument needed to make full usage of the described advanced FDTD modeling capabilities. Therefore the scheme was integrated into and combined with the simulation platform SEMCAD. SEMCAD is continuously improved and extended by a Swiss Consortium composed of two academic institutions (Integrated Systems Laboratory (IIS), ETHZ and IT'IS) as well as two commercial companies (Schmid & Partner Engineering AG (SPEAG) and Integrated System Engineering (ISE) AG). The platform is based on the state-of-the-art ACIS® 3-D based solid modeling environment featuring semi-automated generation of non-homogeneous meshes as well as fully automated material assignment. The CAD environment enables a grid independent positioning, tilting and moving of objects without any restrictions to a predefined resolution or grid configuration.

6.3 Reflection and Stability

6.3.1 Reflection from Boundary

The reflection at the subgrid - coarse grid interface was determined for a plane-wave traversing the subgridding region. Therefore a subspace consist-

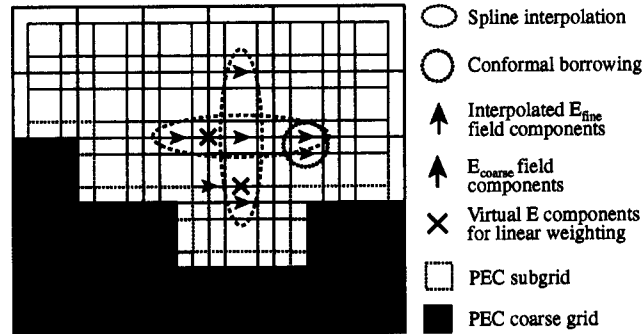


Figure 6.6: Application of modified interpolation schemes for PEC structures traversing the subgrid - coarse grid boundary.

ing of $31 \times 31 \times 23$ fine cells was placed inside a coarse grid computational domain extended about $0.5 \lambda \times 0.5 \lambda \times 1 \lambda$ in the x , y and z directions at $f_{max} = 10$ GHz with a minimum mesh step of $\lambda_{min}/60$. This setup is illustrated in figure 6.7 (shown for 1:16 subgrid transition). In order to observe the reflections from the subgrid boundary, a field sensor was placed at a three cells distance from the transition region used for spline interpolation. For the excitation, a gaussian sine pulse with a bandwidth $B = 10$ GHz was applied to a simulation including the subgrid as well as to a reference calculation where the subgrid was deactivated. In figure 6.8 the reflection from a 1:2 subgrid transition is depicted for the selected frequency range within 10 GHz. The type of interpolation applied in the scheme leads to very low reflections of ≤ -70 dB even at higher frequencies.

6.3.2 Stability Considerations

One of the major issues with respect to subgridding schemes is stability. The abrupt spatial and temporal transition between the two intersecting grids prevents the application of the Yee scheme throughout the entire computational domain, which does not satisfy the CFL condition. Furthermore, all errors introduced by inter- and extrapolation in time and space for the determination of missing components in the interface region are summed up in the iterative leap-frog updating process, which could lead to instabilities, i.e., the methods are conditionally stable. Due to the highly complex updating scheme of the presented algorithm and of 3-D subgridding schemes in general, an algebraic derivation has not yet been ruled out and will be

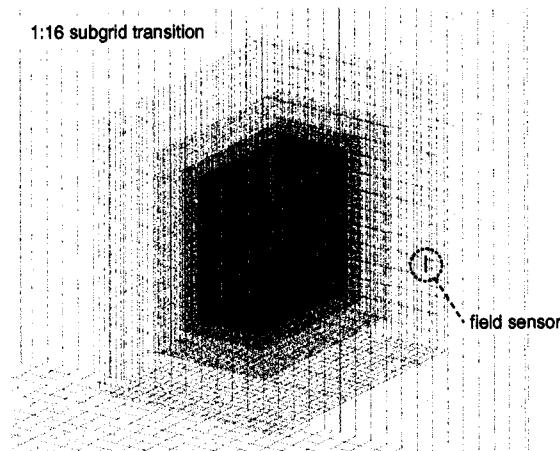


Figure 6.7: Reflection from subgrid interface for plane wave excitation: multi-grid transition (1:16) embedded into base-grid.

subject to future investigation. A meaningful investigation on general sub-gridding and stability is only presented in [26] for the spatial scheme of a 2-D subgrid based on a simple interpolation approach. However, the influence of corners and edges in the 3-D space cannot be covered by 2-D stability analysis.

In order to derive a stability criterion for the presented scheme, each of the 13 sub-steps within an updating cycle can be formulated as a relation between Yee field values at two following sequential timesteps either valid inside or outside the subgrid region, which will lead to a product of different matrix terms. Via Fourier mode analysis the corresponding amplification matrix has to be derived. To ensure stability of the system, all roots of the characteristic polynomial derived from the amplification matrix must be less or equal to one. An extensive discussion of this procedure is found, e.g., in [27] for the case of a 2-D problem using different time stepping schemes. A detailed description of the appropriate procedure can be found in [28] and [29]. The derivation of the characteristic polynomial for the method presented within this study obviously leads to a highly complex system for which the solution is beyond the scope of this paper.

However, by application of temporal interpolation instead of extrapolation for the determination of missing components as discussed in section 6.2.2, stable solutions were achieved for up to 20 000 timesteps using a slightly reduced CFL by a factor of 0.9. Further improvement was achieved

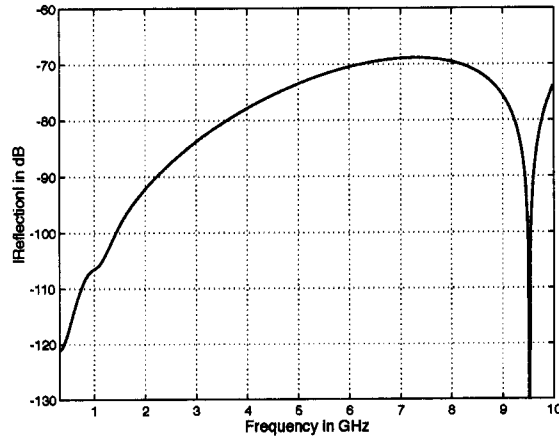


Figure 6.8: Reflection from a 1:2 subgrid region assessed within a 10 GHz frequency range.

by application of the smoothing cubic splines for spatial interpolation. The remaining tendency to instability occurred due to a slightly divergent computation of E- and H-field components in the vicinity of the subgrid boundary within the main grid. The temporal interpolation procedure described in section 6.2.2 performs an averaging procedure in step no. 6, weighting the influence of missing electric and magnetic field values determined in the previous steps 4 and 5. This indirectly specifies the order of discontinuity within the intersection region between the two grids. By experimental optimization, the averaging factors for the H-field values directly determined by interpolation ($h_h^{n-1/4}$) and indirectly calculated via the E-field and a following Yee update ($h_e^{n-1/4}$) were assessed. Two configurations signifying low- and high-level challenge with respect to subgridding have been applied for the optimization process: a plane wave traversing the subgrid and a dipole antenna where the PEC monopoles traverse the subgrid boundary. Optimal behavior was found for the following factors:

$$h_{border}^{n-1/4} = 0.651h_e^{n-1/4} + 0.349h_h^{n-1/4} \quad (6.2)$$

where $h_{border}^{n-1/4}$ corresponds to the H-field values located in the boundary region, initially missing at $t = n - 1/4$. By application of these factors no tendencies to instabilities were observed, even for testing up to 100 000 subgrid - main grid timesteps.

6.3.3 Grid Nesting Capability

The algorithm presented in this paper allows the easy and robust nesting of meshes, i.e., subgrids may be arbitrarily placed (sequential and parallel) and arranged into each other in order to achieve higher refinements for selected regions. The applied CFL timestep reduction factor of 0.9 can thereby be kept constant in the main grid, while for every followed nested grid the timestep is halved. This enables retention of the timestep in the main grid - which normally consists of the most mesh cells - almost at its maximum value. For the assessment of the reflection from such nested subgrids, 4 grids have been sequentially interleaved using a 4 and a 6 mesh cell distance from one grid to the next. Figure 6.7 shows a specific setup where the field sensor determining the reflections is placed just in front of the most outer subgrid. Except for the nested subgrids all mesh and simulation parameters are identical as the setup described in section 6.3.1.

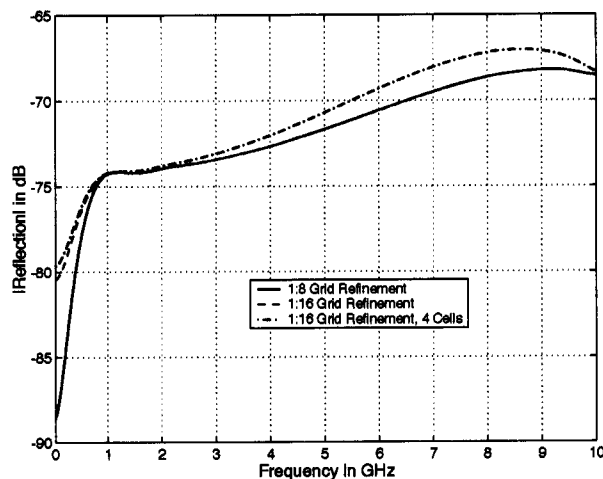


Figure 6.9: Reflection from the presence of nested grids for the cases of 1:8 and 1:16 refinement using 6 mesh cells between the grids and a decrease to 4 cells between the interleaved grids.

Figure 6.9 depicts the reflection from the subgrid - coarse grid boundary for refinements of 1:8 and 1:16 as well as for 4 and 6 cells between each grid using a 1:16 refinement. Removing the most inner subgrid for the 1:8 transition shows a significant effect only in the lowest frequency range up to 1 GHz. Positioning the grids closer to each other shows a slight increase of

the reflection by about 2 dB, mainly at higher frequencies. In general very low reflections < -65 dB are obtained in this broad frequency range for such high mesh refinement factors, which clearly demonstrates the mesh nesting capabilities of the demonstrated subgrid scheme.

6.4 Conclusions

A novel three-dimensional subgridding scheme for FDTD has been presented. It applies smoothing cubic splines for the 3-D spatial interpolation, greatly reducing reflections from the interface boundary. Furthermore, a novel temporal scheme based on interpolation in time leads to enhanced stability and robustness, compared to existing extrapolation based techniques. The scheme has proven to be robust without tendencies to instabilities above 100 000 subgrid - coarse grid timesteps using a just slightly reduced CFL number of 0.9. Low reflections in the range of < -65 dB are obtained for high mesh-nesting ratios of up to 1:16. Based on a broad variety of benchmark examples presented in chapter 7 of this thesis, the scheme demonstrates its general applicability for PEC or lossy dielectric materials traversing the subgrid boundary. Using a sequential and/or parallel nesting of low reflecting 1:2 schemes enables a straightforward application of this technique, providing high suitability for automated grid generation embedded in user-friendly CAD environments, even in the case of complex real-world engineering problems.

References

- [1] K.S. Yee, "Numerical solution of initial boundary value problems involving Maxwell's equations in isotropic media", *IEEE Transactions on Antennas and Propagation*, vol. 14, pp. 302-307, 1966.
- [2] A. Taflove, *Computational Electrodynamics - The Finite Difference Time Domain Method*, Artech House, Norwood, MA, 1995.
- [3] D.M. Sullivan, *Electromagnetic Simulation Using The FDTD Method*, IEEE Press, Piscataway, NJ 008855-1331, 2000.
- [4] K.S. Kunz and R.J. Luebbers, *The Finite Difference Time Domain Method for Electromagnetics*, CRC Press, Boca Raton, FL, 1993.
- [5] M.A. Jensen and Y. Rahmat-Samii, "EM interaction of handset antennas and a human in personal communications", *Proceedings of the IEEE*, vol. 83, no. 1, pp. 7-17, Jan. 1995.
- [6] M. Okoniewski and M.A. Stuchly, "A study of the handset antenna and human body interaction", *IEEE Transactions on Microwave Theory and Techniques*, vol. 44, no. 10, pp. 1855-1864, Oct. 1996.
- [7] V. Hombach, K. Meier, M. Burkhard, E. Kühn, and N. Kuster, "The dependence of EM energy absorption upon human head modeling at 900 MHz", *IEEE Transactions on Microwave Theory and Techniques*, vol. 44, no. 10, pp. 1865-1873, Oct. 1996.
- [8] R. Holland, "Pitfalls of staircase meshing", *IEEE Transactions on Electromagnetic Compatibility*, vol. 35, no. 4, pp. 434-439, Nov. 1993.
- [9] A.C. Cangellaris and D.B. Wright, "Analysis of the numerical error caused by the stair-stepped approximation of a conducting boundary in fdtd simulations of electromagnetic phenomena", *IEEE Transactions on Antennas and Propagation*, vol. 39, no. 10, pp. 1518-1525, Oct. 1991.
- [10] A. Akyurtlu, D.H. Werner, V. Veremey, D.J. Steich, and K. Aydin, "Staircasing errors in FDTD at an air-Dielectric interface", *IEEE Microwave and Guided Wave Letters*, vol. 9, no. 11, pp. 444-446, Nov. 1999.
- [11] D.H. Choi and W.J.R. Hofer, "A graded mesh FD-TD algorithm for eigenvalue problems", in *17th European Microwave Conference Digest*, 1987, pp. 413-417.

- [12] W. Heinrich, K. Beilenhoff, P. Mezzanotte, and L. Roselli, "Optimum mesh grading for finite-Difference method", *IEEE Transactions on Microwave Theory and Techniques*, vol. 44, no. 9, pp. 1569–1574, Sept. 1996.
- [13] Andreas Christ, Jürg Fröhlich, and Niels Kuster, "Analysis and correction of numerical phase velocity errors in nonuniform FDTD meshes", *IEEE Transactions on Microwave Theory and Techniques*, 2001, submitted.
- [14] P.H. Harms, J.F. Lee, and R. Mittra, "A study of the nonorthogonal fdtd method versus the conventional fdtd technique for computing resonant frequencies of cylindrical cavities", *IEEE Transactions on Microwave Theory and Techniques*, vol. 40, no. 4, pp. 741–746, Apr. 1992.
- [15] T.G. Jurgens, A. Taflove, K. Umashankar, and T.G. Moore, "Finite-difference time-domain modeling of curved surfaces", *IEEE Transactions on Antennas and Propagation*, vol. 40, no. 4, pp. 357–366, Apr. 1992.
- [16] S.S. Zivanovic, K.S. Yee, and K.K. Mei, "A subgridding method for the time-Domain finite-Difference method to solve maxwell's equations", *IEEE Transactions on Microwave Theory and Techniques*, vol. 39, no. 3, pp. 471–479, Mar. 1991.
- [17] J.W. Nehrass and R. Lee, "Optimal finite-Difference sub-Gridding techniques applied to the helmholtz equation", *IEEE Transactions on Microwave Theory and Techniques*, vol. 48, no. 6, pp. 976–984, June 2000.
- [18] P. Thoma and T. Weiland, "A consistent subgridding scheme for the finite difference time domain method", *International Journal of Numerical Modelling*, vol. 9, pp. 359–374, 1996.
- [19] M.J. White, Z. Yun, and M.F. Iskander, "A new 3-D FDTD multigrid technique with dielectric traverse capabilities", *IEEE Transactions on Microwave Theory and Techniques*, vol. 49, no. 3, pp. 422–430, Mar. 2001.
- [20] T.O. Körner and W. Fichtner, "Refractive index adaptive gridding for finite-Difference time-Domain methods", *International Journal of Numerical Modelling*, vol. 12, 1999.

- [21] M.W. Chevalier, R.J. Luebbers, and V.P. Cable, "FDTD local grid with material traverse", *IEEE Transactions on Antennas and Propagation*, vol. 45, no. 3, pp. 411–421, Mar. 1997.
- [22] M. Okoniewski, E. Okoniewska, and M. Stuchly, "Three-Dimensional subgridding algorithm for FDTD", *IEEE Transactions on Antennas and Propagation*, vol. 45, no. 3, pp. 422–429, Mar. 1997.
- [23] W. Yu and R. Mittra, "A new subgridding method for the finite-Difference time-Domain (FDTD) algorithm", *Microwave and Optical Technology Letters*, vol. 21, no. 5, pp. 330–333, June 1999.
- [24] S. Chaillou, J. Wiart, and W. Tabbara, "A subgridding scheme based on mesh nesting for the fdtd method", *Microwave and Optical Technology Letters*, vol. 22, no. 3, pp. 330–333, Aug. 1999.
- [25] C. de Boor, *A Practical Guide to Splines*, Springer-Verlag, New York, 1978.
- [26] P. Monk, "Sub-Gridding FDTD schemes", *ACES Journal*, vol. 11, no. 1, pp. 37–46, Mar. 1996.
- [27] C. Schuster, *Simulation, Analysis, and Parameter Extraction of Electronic Components and Circuits Using the Finite Difference Time Domain Method*, PhD thesis, Diss. ETH Nr.13522, Zurich, 2000.
- [28] K. W. Morton and D. F. Mayers, *Numerical Solution of Partial Differential Equations*, Cambridge University Press, Cambridge, UK, 1994.
- [29] J. W. Thomas, *Numerical Partial Differential Equations: Finite Difference Methods*, Springer, Berlin, Germany, 1995.

Seite Leer /
Blank leaf

Part III

**Benchmarks and
Applications**

Seite Leer /
Blank leaf

Chapter 7

Benchmarks: Antennas Embedded in Complex Environments

Abstract This chapter presents a variety of benchmark examples in the field of antenna design and dosimetry. In the first part, mainly helical antennas are addressed and represented in detail and with increasing modeling complexity, by application of the subgridding technique presented in chapter 6. Furthermore, the definite advantages of local refinement schemes for reduced computational requirements are demonstrated.

7.1 Benchmarks

7.1.1 Helical Antenna on PEC Ground Plane

The subgridding scheme was first tested against a benchmark published in [1]. Examined is a normal-mode monopole helical antenna over a PEC ground plane. The dimensions are summarized in table 7.1 and figure 7.1.

In order to perform an appropriate representation of the helix, a 1:4 (2 nested grids) subgrid transition was applied. For the most inner subgrid a high resolution of 0.19 mm was used, which enabled modeling the helical wire with a four cell diameter. The first and second subgrid consisted of 1.1×10^6 and 330×10^3 cells, respectively, whereas for the main grid a graded mesh ($\Delta s_{min} = 0.76 \text{ mm}^3$, $\Delta s_{max} = 7 \text{ mm}^3$, ratio = 1.2) was used, which lead to about 650×10^3 cells.

¹This chapter addresses the benchmarks and applications part of the subgridding algorithm presented in chapter 6.

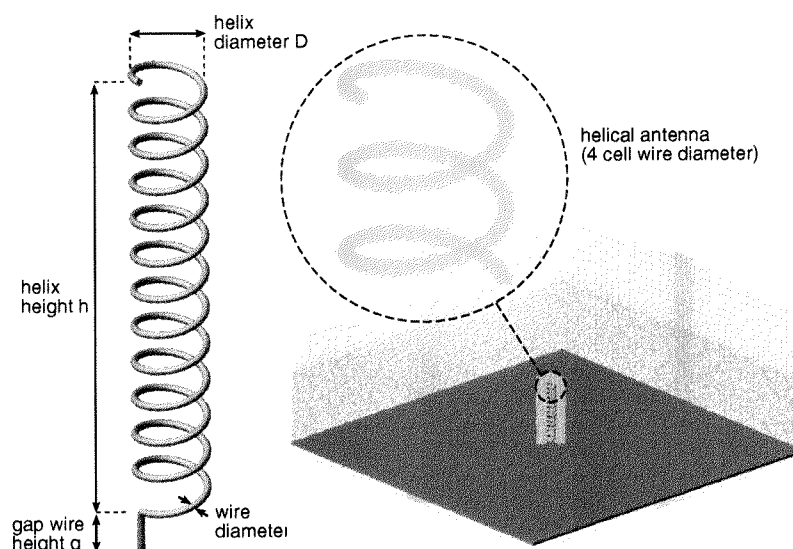


Figure 7.1: Helical antenna mounted on PEC ground plane operating in normal-mode: CAD model and FDTD grid (1:4 subgrid - graded mesh)

Figure 7.1 depicts the CAD model of the helical antenna placed on a ground plane embedded into a 1:4 subgrid as well as a detailed view of the discretized antenna tip section. Without application of the subgrid, the use of only a graded mesh (same parameters as for subgrid case) leads to 1.1×10^6 grid cells, which increases the computational runtime by a factor of about five.

Within the simulation, the PEC ground plane was modeled floating with respect to the absorbing boundary (AB) to simulate a ground layer of infinite extension. The distance from the antenna to the AB was about $\lambda/4$ at the frequency $f = 450$ MHz. The source was placed into a small gap of 0.19 mm in height, located between the ground plane and the helix feeding wire. The excitation itself is modeled by a resistive voltage source as proposed in [2] with an internal source resistance of 50Ω . To assess broadband frequency domain information, a gaussian sine pulse with a bandwidth $B = 200$ MHz was applied. For this case the simulation reached steady state after 30 ns (90×10^3 timesteps (ts) in 1:4 subgrid). All simulations were bounded by a perfectly matched layer (PML) [3] absorbing boundary condition (ABC) with a layer thickness of 8 cells.

Table 7.1: Dimensions of the normal-mode helical antenna.

Parameters	Dimensions
Number of turns n	12
Diameter of helix D	7.34 mm
Radius of helix wire a	0.38 mm
Height of helix h	50 mm
Gap between helix and ground plane g	5 mm

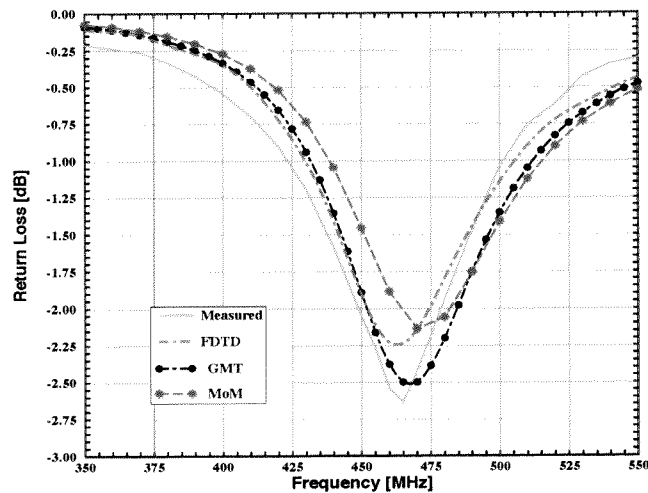


Figure 7.2: Comparison of the return loss for a helical antenna operating in normal-mode computed with FDTD using subgrids to measurements as well as results obtained from simulations performed with GMT and MoM.

The FDTD simulations were compared with results reported in [1]. They were obtained by applying the GMT-based 3D Multiple Multipole (MMP-3D) code [4], the MoM based Numerical Electromagnetics Code package *NEC-Win Professional* [5]. For the experimental impedance characterization, the antenna was mounted on a copper ground plane of 1 m^2 , whereby the nearest object was farther than in 2 m distance. The measurements were conducted with the Network Analyzer Agilent 8753C S-parameter test set.

Figure 7.2 shows the return loss with respect to a 50Ω reference of the measured and simulated helical antenna within a frequency range from 350 MHz to 550 MHz. The simulations using FDTD properly match the

resonance frequency. In general, the agreement of all three numerical techniques is within the uncertainties of the experimental setup. For the GMT model, the slight shift in the resonance frequency might be due to the use of a slightly smaller diameter than present in the physical helix by application of a thin wire expansion as a basis function. In MoM, the tangential H-field is modeled to be symmetric at the annular of the wire which is not true if electromagnetic coupling occurs in the immediate vicinity of structures like the helical wire. This might cause the prominent frequency shift observed.

7.1.2 Helical Antenna on Generic Phone at 900 MHz

The second more complex benchmark was the generic phone equipped with a helical antenna as defined in [6]. Figure 7.3 shows the physical phone and its numerical CAD model used within the FDTD simulations.

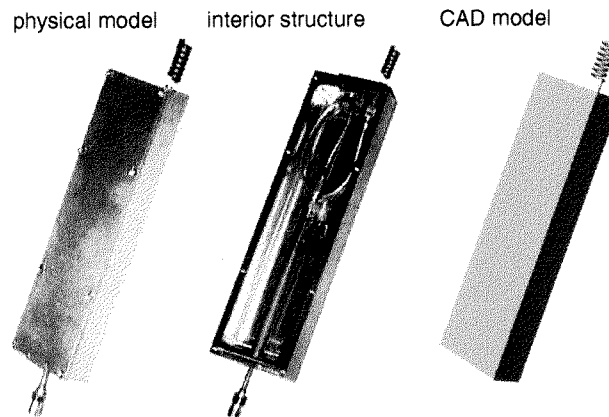


Figure 7.3: Generic phone equipped with helical antenna: physical (left), interior structure (middle) and CAD model (right) used within FDTD simulations.

The dimensions of the box were 40 mm×16 mm×140 mm. The axial-mode helix had 7 turns with a diameter of 6.4 mm and a pitch angle of 7.2°, whereby the feeding wire was 5 mm long and the helix wire cross-section was 1.3 mm in diameter.

Surface waves on the cable were suppressed by a $\lambda/4$ stub as well as ferrites. The feedpoint impedance was measured by the network analyzer (Agilent 8753E). The dosimetric evaluation was performed using DASY4 (Schmid & Partner Engineering AG, Zurich) according to EN50361 [7]. The

standard uncertainty for these evaluations was determined to be $\pm 12\%$ [8].

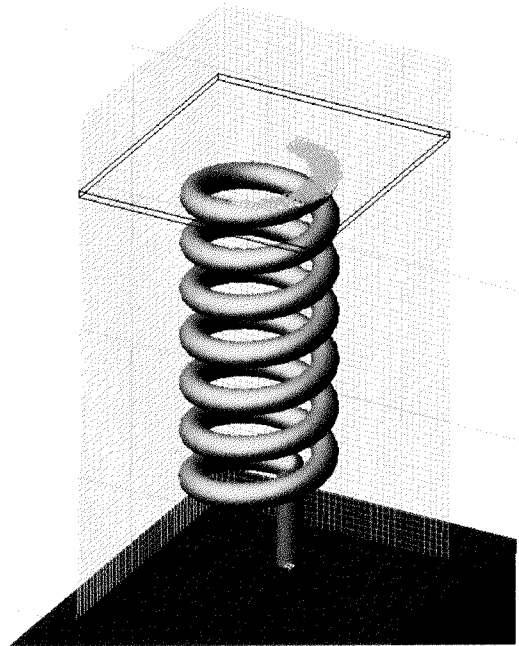


Figure 7.4: Helix located in 1:2 subgrid region.

Figure 7.4 depicts a detailed view of the helix model located inside a 1:2 subgrid with the discretized structure shown in a specific slice. Using a homogeneous subgrid resolution of 0.325 mm^3 in the region of the helix enabled a detailed representation of the helical cross wire section by 4×4 cells. For the free space computation domain extended by 1.2λ in each direction, a non-homogeneous mesh with a maximum step of 8 mm (ratio = 1.2) was applied. As reference calculation a computation using the same grid parameters but without integration of the subgrid was performed. The computation space was bounded by 8 layer PML. The discrete source was placed into a gap of 0.325 mm extension in the feedpoint region between the PEC box and helix feeding wire. The excitation is modeled as discussed in section 7.1.1 by a resistive voltage source (50Ω) and was excited using a broadband gaussian sine pulse.

In addition to the validation of the subgridding scheme, the influence of modeling and meshing detail on the obtained results was assessed. Therefore

two helices, *round* and *square* shaped, were modeled which consist only of single edges in wire diameter instead of multiple cells. The helical wires were modeled at the same electrical length as performed for the subgrid calculation. All additional grid parameters were kept constant compared to the subgrid model.

The two simulations result in identical impedances (figure 7.6). They also correspond well with the measurement values. This is also verified in figure 7.5 which shows a 2-D error distribution for the electric and the magnetic field compared to the reference solution in a plane which intersects the antenna's feedpoint region. The comparison of this near-field area reveals very low deviations of less than 0.05 dB in most of the regions observed for both field types. The percent error of the absolute E-field for ϕ - and θ -component in the far-field is better than $< 0.5\%$.

As expected, the non-accurate geometrical representation of the antenna leads to different results, which would not only have a significant effect on the impedance but also in the near-field of the antenna. This is of greatest importance if any scatter is within that region, e.g., a human hand or a head.

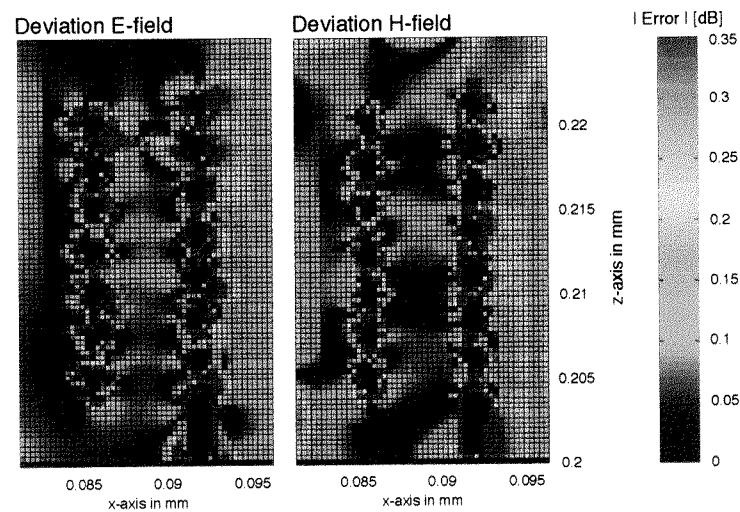


Figure 7.5: Error distribution of subgrid for electric and magnetic field compared to the reference solution in a plane intersecting the helical antenna.

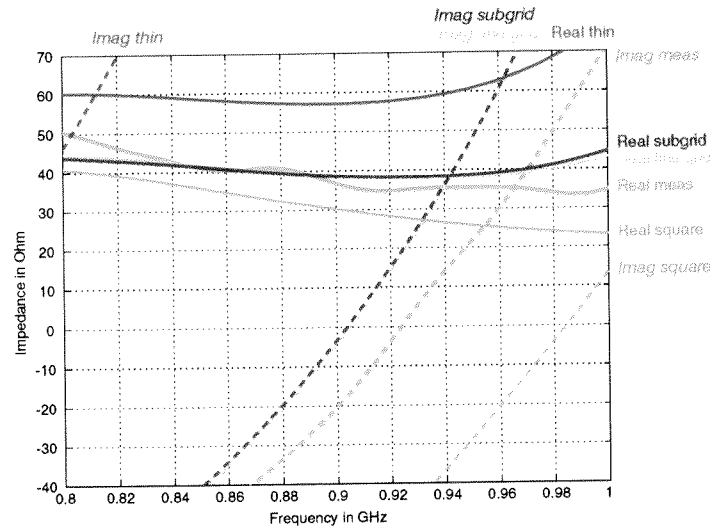


Figure 7.6: Comparison of feedpoint impedance for reference, subgrid and thin helix calculations to measurements.

7.1.3 Generic Phone - SAM Phantom

In order to validate the subgridding scheme and its applicability within non-homogeneous environments implying enhanced complexity as well as subgrids traversing material boundaries, the generic phone was simulated in the standard positions next to the Specific Anthropomorphic Mannequin (SAM) standard phantom defined in [9] and [10] (figure 7.7). The phantom shell was represented with $\epsilon_r = 3.5$. The interior is filled with head tissue simulating liquid at 900 MHz, i.e., using $\epsilon_r = 41.5$ and $\sigma = 0.97$.

One 1:2 subgrid was applied to achieve an identical grid resolution and number of cells as well as geometrical detail of the helix as in benchmark 3. Including the generic phantom the whole base-grid computation domain consisted of about 4×10^6 cells, whereby a graded mesh ($\Delta s_{min} = 0.65 \text{ mm}^3$, $\Delta s_{max} = 10 \text{ mm}^3$, ratio = 1.2) was used.

In table 7.2, the results for the measured (M) and simulated (S) spatial peak SAR values ($f = 900 \text{ MHz}$, normalized to 1 W input power) for the *touch* and 15° standard test positions and averaged over 1 g are summarized. Very good agreement is obtained for the *touch* position, which might result from the cancellation of simulation and experimental errors; however, the

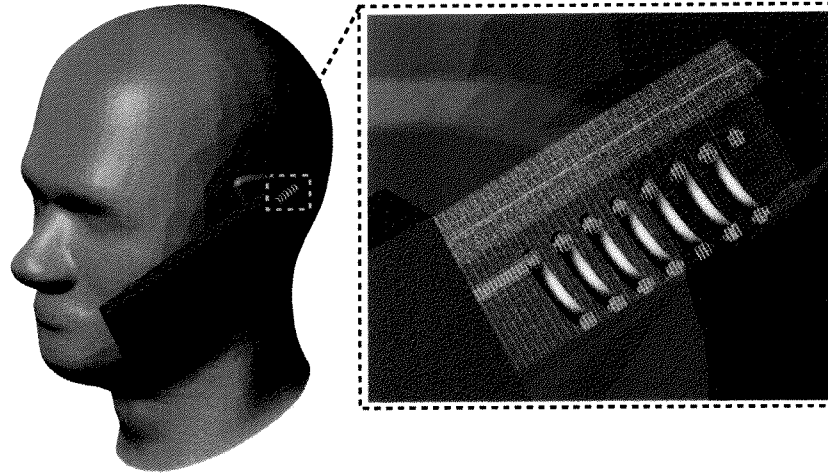


Figure 7.7: Helical antenna on generic phone placed within subgrid region close to SAM phantom model.

maximum deviations for both standard positions are within the uncertainty of the simulation and the tolerances of the measurement system. Figures 7.8 and 7.9 show the measured and simulated feedpoint impedance for both standard positions in a 300 MHz frequency range. Whereas the sensitive imaginary part shows slight deviations from the measured data, in general for both parts good agreement is obtained.

Table 7.2: 1 g averaged SAR in touch and 15°-tilted position

Type	SAR _M [W/kg]	SAR _S [W/kg]	Diff [%]
1g _{Touch}	9.72	9.65	-0.72
1g _{Tilted}	11.90	13.60	+14.2

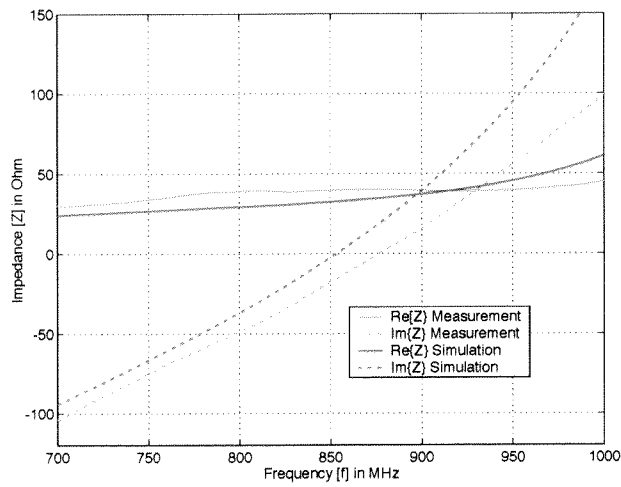


Figure 7.8: Feedpoint impedance in touch position.

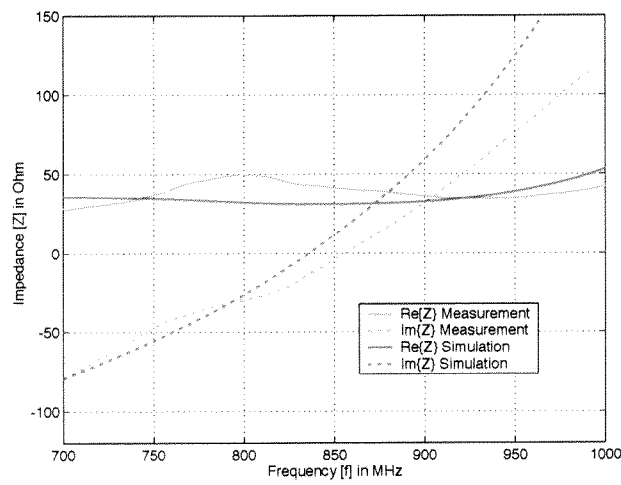


Figure 7.9: Feedpoint impedance in 15° position.

7.2 Discussion: Computational Efficiency

Commercial devices and equipment usually include structures which are considerably smaller than those of benchmark problems. Although these structures often do not significantly affect electromagnetic performance, it is generally impossible to exclude the occurrence of modeling influences *a priori*, for which reason highly detailed simulations are often desired. A typical example of the degree of detail needed is the analysis of real-world transmitter structures given in [11]. Furthermore, functional details of compact antennas embedded in a computational domain spatially expanded by several wavelengths may require resolutions smaller than $10^{-4} \cdot \lambda$.

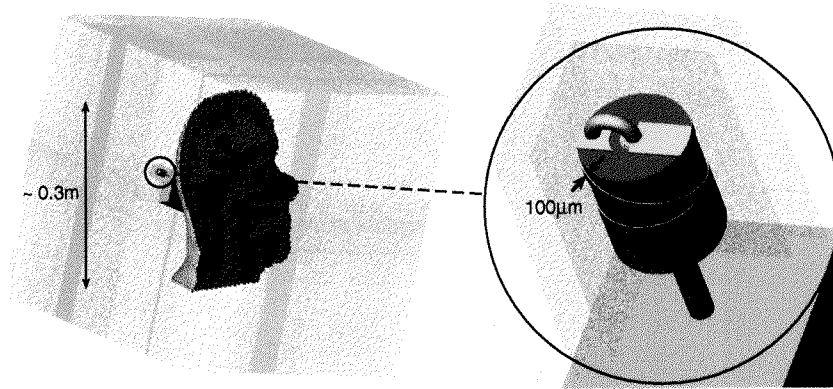


Figure 7.10: Enhanced modeling by application of a combined nested subgrid approach embedded within graded mesh.

Such an example is given by a bifilar antenna presented in [12], [13] mounted on a generic phone and placed next to the ear of a nonhomogeneous head model [14] as shown in figure 7.10. The $100\mu\text{m}$ structure can be simulated with only 5×10^6 cells in the main grid by application of a nested 1:4 subgrid combined with graded mesh (innermost subgrid had a high resolution of 0.1 mm^3 ; outer subgrid is composed of 190×10^3 mesh cells; main grid is graded from 0.4 mm up to 8 mm). The comparison between this enhanced approach and a common graded mesh as well as a homogeneous modeling with respect to computational requirements is shown in table 7.3. For a harmonic simulation at 2.4 GHz , steady state was reached after 30 periods, which corresponds to about 60×10^3 coarse grid - subgrid timesteps. The time indication in table 7.3 is related to LINUX on an Intel P4 1.7 GHz

architecture.

In some cases, high spatial resolution is not only required in a single sub-volume of the computational domain but within several independent ones. For such particular situations, graded mesh would not provide a significant reduction of computational expenses. A related example is shown in figure 7.11, evaluating the coupling effect between animals of different sizes embedded within an exposure chamber for bioexperiments [15]. By parallel application of four nested 1:4 subgrids, the animals were modeled with a high resolution of 0.5 mm. For this case, 4.9×10^6 homogeneous 2 mm grid cells are used within the main grid. The estimated computational expenses shown in table 7.4, compared to pure graded and homogeneous mesh, demonstrate that this example could not be numerically analyzed using common FDTD schemes due to missing or non-affordable computational resources.

Table 7.3: Memory and runtime requirements for the human head - miniature antenna model (LINUX on Intel P4 1.7 GHz).

Type	Base-Cells	Memory	Time
Sub 1:4	5×10^6	650 MB	14 h
Graded	20×10^6	2.5 GB	≈ 6 days
Homogeneous	11×10^9	≈ 1.5 TB	≈ 1.5 years

Table 7.4: Memory and runtime requirements for different methods to achieve an animal model resolution of 0.5mm (LINUX on Intel P4 1.7 GHz).

Type	Base-Cells	Memory	Time
Sub 1:4, 0.5 mm	4.9×10^6	1.5 GB	2 days
Graded, 0.5-5 mm	150×10^6	19 GB	≈ 40 days
Homog., 0.5 mm	310×10^6	≈ 40 GB	≈ 3 months

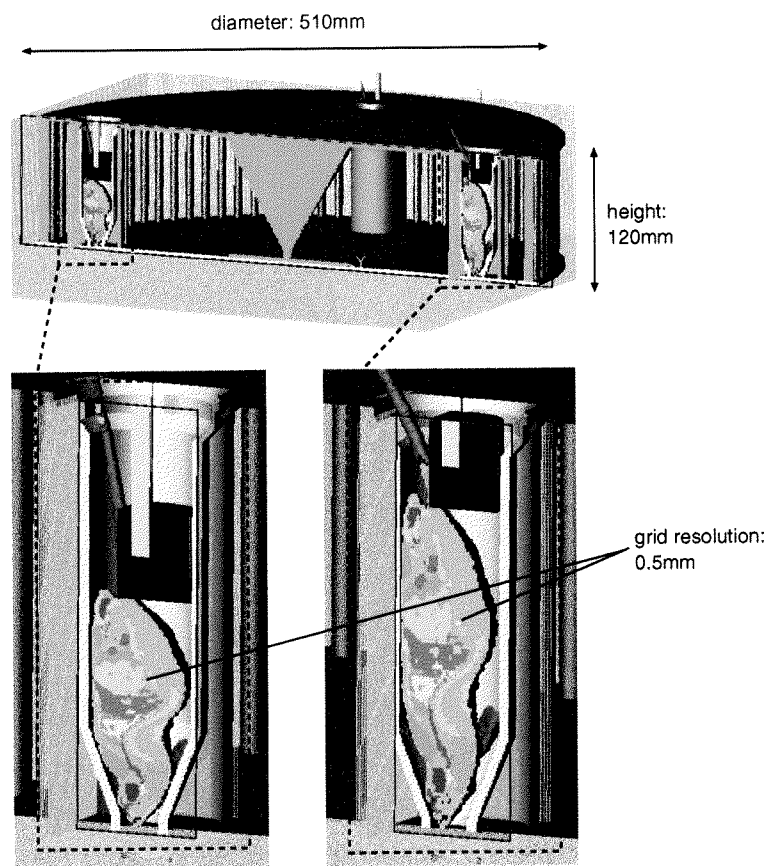


Figure 7.11: Combined multiple 1:4 subgrid - homogenous mesh: setup for bioexperiments including high resolution animal models.

References

- [1] Y.S. Tay, *Contributions Towards the Optimization of Hand-held Mobile Telecommunication Equipment by Computational Electromagnetics*, PhD thesis, Diss. ETH Nr.12311, Zurich, 1997.
- [2] M.J. Piket-May, A. Taflove, and J. Baron, "FD-TD modeling of digital signal propagation in 3-D circuits with passive and active loads", *IEEE Transactions on Microwave Theory and Techniques*, vol. 42, pp. 1514–1523, 1994.
- [3] J.P. Berenger, "A perfectly matched layer for the absorption of electromagnetic waves", *Journal of Computational Physics*, Oct. 1994.
- [4] C. Hafner and L.H. Bomholt, *The 3D Electrodynamic Wave Simulator*, John Wiley & Sons, 1993.
- [5] G.J. Burke, *Numerical Electromagnetics Code - NEC-4: Method of Moments*, Lawrence Livermore National Laboratory, California, Jan., 1992.
- [6] M. Burkhardt, N. Chavannes, K. Poković, T. Schmid, and N. Kuster, "Study on the FDTD performance for transmitters in complex environments", *Proceedings of the ICECOM, Dubrovnik*, pp. 83–86, Oct. 1997.
- [7] CENELEC, *EN 50361, Basic standard for the measurement of Specific Absorption Rate related to human exposure to electromagnetic fields from mobile phones*, Brussels, July 2001.
- [8] K. Poković, *Advanced Electromagnetic Probes for Near-Field Evaluations*, PhD thesis, Diss. ETH Nr.13334, Zurich, 1999.
- [9] CENELEC, *prEN 50360, Product standard to demonstrate the compliance of mobile telephones with the basic restrictions related to human exposure to electromagnetic fields (300 MHz - 3 GHz)*, Brussels, June 2000.
- [10] IEEE, *Std. 1528-200X, Recommended Practice for Determining the Spatial-Peak Specific Absorption Rate (SAR) in the Human Body Due to Wireless Communications Devices: Experimental Techniques*, June 2000.

- [11] N. Chavannes, R. Tay, N. Nikoloski, and N. Kuster, "RF design of mobile phones by TCAD: Suitability and limitations of FDTD", *IEEE Antennas and Propagation Magazine*, Submitted, 2002.
- [12] O. Leisten, Y. Vardaxoglou, T. Schmid, B. Rosenberger, E. Agboraw, N. Kuster, and G. Nicolaidis, "Miniature dielectric-loaded personal telephone antennas with low user exposure", *Electronics Letters*, vol. 34, no. 17, pp. 1628–1629, Aug. 1998.
- [13] O. Leisten, J.C. Vardaxoglou, and P. McEvoy, "Miniature dielectric-Loaded antennas for personal telephony and mobility", *Microwave Engineering Europe*, pp. 31–34, Aug. 2000.
- [14] M. Burkhardt, *Contributions Toward Uncertainty Assessments and Error Minimization of FDTD Simulations Involving Complex Dielectric Bodies*, PhD thesis, Diss. ETH Nr.13176, Zurich, 1999.
- [15] Sven Ebert, Jürg Fröhlich Walter, Oesch, Urs Frauenknecht, and Niels Kuster, "Optimized in vivo exposure setups for risk assessment studies at the mobile communication frequencies 902MHz and 1747MHz", in *2001 The Bioelectromagnetics Society*, St. Paul, Minnesota, USA, June 2001, p. 27.

Chapter 8

RF Design of Mobile Phones by TCAD: Suitability and Limitations of FDTD

Abstract This paper discusses the general suitability and possible limitations of an enhanced Finite-Difference Time-Domain (FDTD) simulation environment for straightforward and efficient RF design of complex transmitters. The study was conducted using one of the latest commercially available multi-band mobile phones. Simulations were conducted in free space and with various dielectric loads, whereby different parameters were evaluated such as impedance, efficiency, far-fields, as well as near-field distributions of E- and H-fields and the Specific Absorption Rate (SAR). The results are compared to measurements obtained with the latest tools available. In addition, mechanical design issues which show a significant influence on the electromagnetic (EM) field behavior could be predicted by simulations and were experimentally reproduced. The obtained accurate prediction of all essential performance parameters by straightforward simulations suggests that state-of-the-art software packages are suitable for device design in industrial research and development (R&D) environments with hardly any limitations, provided the availability of excellent and flexible user interfaces and the applicability of graded meshes combined with robust subgrids.

¹N. Chavannes, R. Tay, N. Nikoloski and N. Kuster, "RF design of mobile phones by TCAD: suitability and limitations of FDTD", *IEEE Antennas and Propagation Magazine*, 2002 - to be published.

8.1 Introduction

The last two decades have shown tremendous growth within the mobile telecommunications equipment (MTE) sector. Furthermore, consumers have put high demands on excellent product quality combined with low pricing. Due to increasing competition and rapid market expansion, the life cycles of the products themselves and hence device development cycles are getting shorter. In addition, new requirements have recently been introduced, such as mandatory safety guidelines defined by the regulatory agencies [1], [2], [3], [4]. The market might demand even more efficient devices due to increased public concern about possible adverse health effects of radio frequency (RF) exposure.

These new challenges for RF engineers clearly call for new analysis and optimization tools. Technical computer aided design (TCAD) is the answer provided such that these tools can be applied to real-world designs in a straightforward user-friendly manner. The needs are obvious:

- import and easy manipulation/modification of standard mechanical CAD data formats
- easy and accurate composition of different complex objects (consisting of hundreds of different subvolumes), i.e., different positions of a mobile phone at the human head
- resolutions of a few μm within relatively large environments (m)
- handling of PEC structures embedded in dielectric and lossy material/objects as well as the provision of lumped elements
- computation of all relevant parameters such as feedpoint impedance, radiation pattern, efficiency, heat distribution, etc.
- efficient model generation, short result return time, uncertainty assessment, result visualization which is directly comparable to measured results
- semi-automated optimization by genetic algorithm (GA)

Various numerical methods have been developed and applied for the analysis of antennas, e.g., the Method of Moments (MoM), the General Multipole technique (GMT), the Finite Element method (FE), and the FDTD method. Although some of these algorithms are well suited for the design of basic or

very specific antennas, the general application to structures embedded into largely non-homogeneous and lossy environments is impossible or very difficult. The relatively crude and computationally costly Finite-Difference Time-Domain (FDTD) technique has gained growing interest because of its robustness, suitability to handle complex problems composed of any number of subvolumes and general independence from material composition. The exponential growth of computer performance as well as various enhancements of the technique [5, 6, 7], originally presented by Yee [8], has made FDTD the most popular and most widely applied technique [9, 10, 11]. However, the severe limitations of FDTD have been:

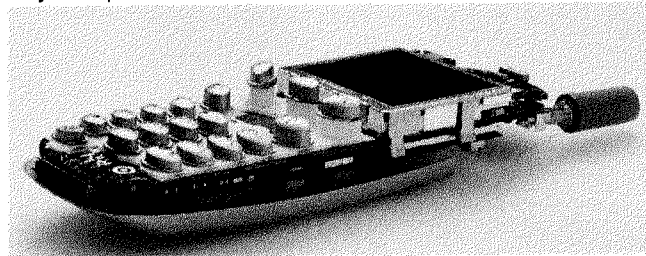
1. Real-world problems often consist of small technical structures embedded in a relatively large computational space. An example would be unintended capacitive coupling between electromechanical components, display, battery and RF shields inside a mobile phone which is operated in close proximity to a human head. These structures may have dimensions of only a few μm , whereby the computational space may reach one meter or more. Only the latest progress in a combination of graded meshes with subgrids can enable FDTD to handle such structures. Previous studies required simplifications such as rectangular metal boxes equipped with monopole or dipole-like structures. Pioneering efforts in helix modeling were mainly performed by staircased wire approximations due to missing tools [12], [10], [13], [14].
2. The restrictions to rectangular grids can result in unacceptable uncertainties due to the stair-stepped approximation of curved or grid non-conformally aligned structures [15], [16], in particular for complex MTE - head configurations [17]. Whereas certain studies have approximated the entire internal structure of CAD derived mobile phones by single PEC blocks [18], [19], the inclusion of specific interior parts was reported, e.g., in [20] by application of grid resolutions of about 1 mm. The investigations presented within this paper clearly point out the importance of an appropriate modeling including significant internal MTE structures modeled with highly refined FDTD mesh.
3. Although generation of the FDTD grid is trivial compared to grid mesh generation within other methods, e.g., FE, an optimized grid can significantly reduce computation time and accuracy of results. Some software packages operate on a predefined grid; others do not allow the handling of objects composed of hundreds of polyhedra or do not support the user with grid optimization [21]. Mainly for the analysis

of fine and detailed structures like antennas used in MTE which are embedded within largely extended spatial environments, the use of enhanced modeling schemes is highly recommended [22]. High efficiency is thereby achieved by the combination of optimized graded mesh [23] and local refinement schemes.

The objective of this study was to evaluate whether FDTD based tools can be utilized for supporting RF engineers in the design of mobile phones. This clearly demands that not only the outer shape of the device is simulated but all embedded electromechanical components which are RF relevant as shown in figure 8.1 and requires resolutions down to $100\ \mu\text{m}$ or less. The quality of the simulation is validated with measurement results utilizing the latest near-field measurement technology.

8.2 Mobile Phone

Physical phone



Phone model within CAD environment

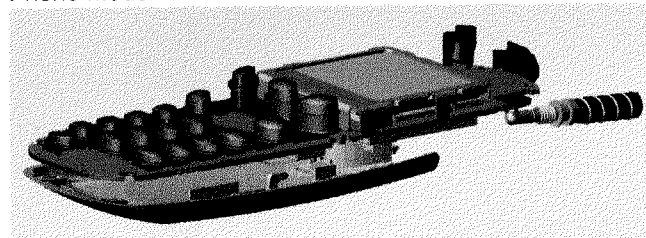


Figure 8.1: Motorola T250 phone: physical model (top) and its numerical equivalent used for the FDTD simulations (bottom).

The phone selected for this study was one of the latest commercially available tri-band phones (GSM, DCS, PCS), namely the T250 of Motorola

Inc. For the purpose of this study, two samples of the phone were purchased in Zurich. The first model was used only for measurements; the second was disassembled and optically examined. The product was designed at Motorola Inc. using the ProEngineer CAD platform. The CAD dataset was consequently exported in STL format for the purpose of modification and modeling within SEMCAD. In this paper the results of only the two main bands are reported, namely GSM and DCS.

8.3 Numerical Method

For all performed simulations the FDTD based platform SEMCAD was used [24]. SEMCAD is the internal simulation platform applied within our research group for research in electromagnetic computations which has also been commercialized by Schmid & Partner Engineering AG (SPEAG). It is continuously improved and extended by a Swiss Consortium composed of the Institute for Integrated Systems (IIS) of ETHZ, IT'IS, SPEAG and Integrated Systems Engineering (ISE) AG. The solid modeling environment is based on the state-of-the-art ACIS[®] modeling toolkit and allows the generation of complex 3-D objects as well as the import of whole CAD datasets in various formats. This CAD environment enables free positioning, tilting and moving of objects without any restrictions to a predefined resolution or grid configuration. In addition, a large database of non-homogeneous human and animal phantoms as well as standard phantoms widens the application range to dosimetry related investigations.

The postprocessing engine enables an extraction of time and frequency domain data from the near- and far-fields. In addition, the combined platforms SEMCAD and DASY4 (see section 8.4) allowed a direct comparison of numerical and experimental data within the same postprocessing environment.

The kernel provides 3-D full wave simulation and incorporates all state-of-the-art FDTD related features, such as the latest absorbing boundary conditions (ABCs) as well as various source/excitation types. Furthermore, a number of algorithms were implemented enabling improved representation of grid non-conformally aligned dielectric and PEC structures and enhanced precision through phase velocity correction for non-homogeneous meshes.

Moreover, the kernel was enhanced by a novel subgridding scheme proposed in [25] and integrated into the SEMCAD simulation platform, combined with semi-automated grid generation. Due to the use of 3-D cubic splines for the spatial interpolation of EM field values between the coarse

and the fine grid, very low reflections are obtained at the subgrid interface (≈ -110 dB for grid step of $\lambda/300$). Contrary to common local refinement schemes, it applies improved temporal interpolation scheme instead of incorporating extrapolated field data. This leads to high robustness and stability ($> 1e5$ time steps) of the method and makes it convenient for a broad range of applications. To further reduce reflections from the transition boundary, a basic refinement factor of two was chosen, which does not diminish the applicability of the scheme since the subgrids can easily be stepped into each other in a sequential or parallel way. This nesting capability was successfully tested for refinements up to 1:32.

Since the mobile phone CAD dataset consists of very detailed parts such as PCB layers and a helical antenna with a minimal spatial extension of $100 \mu\text{m}$, a common graded mesh approach would lead to a large number of Yee cells for the computational space, particularly when placed beside a human head model. Therefore, in order to reduce the computational requirements to a tolerable level, the use of these enhanced modeling techniques was unavoidable.

8.4 Measurement Technique

The measurements were conducted by application of the near-field scanning system DASY4 (Schmid & Partner Engineering AG, Switzerland), which is the fourth generation of the system described in [26] as shown in figure 8.2. The scanner was equipped with the latest probes providing the required isotropy, sensitivity and spatial resolution (see Table 8.1). The phantom used was the Twin SAM [27] which has been recently standardized for antenna performance characterization by various organizations. The probes and the system were calibrated according to [28], [29].

8.5 FDTD Modeling

8.5.1 Implementation of Phone

The first important step was to import the CAD dataset which was provided in STL format. In order to distinguish the individual pieces and to enable an assignment of the different material properties, each subfile was imported separately. The dataset consists mainly of electromechanical parts such as:

- triple band antenna

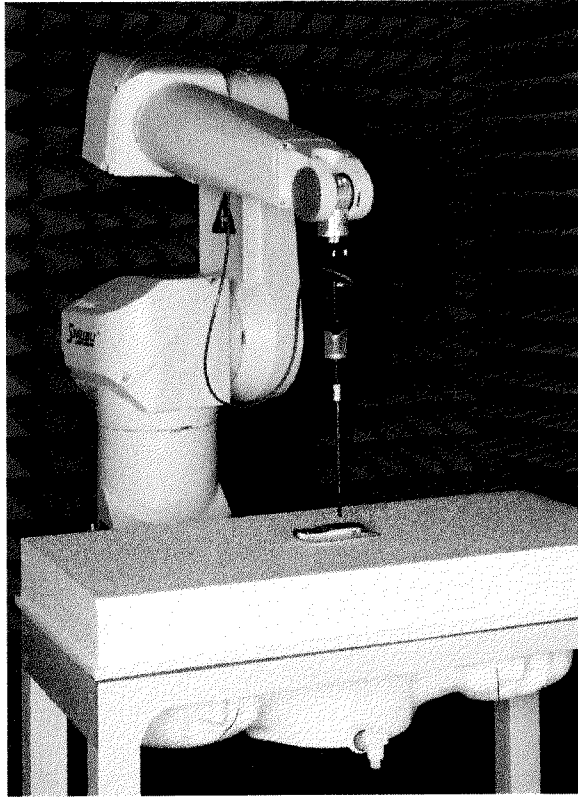


Figure 8.2: Automated dosimetric assessment system DASy4: free space measurement of mobile phone.

- PCB
- shields
- LCD and its holder
- lenses and housing parts
- keypad and buttons
- battery and battery contact
- connectors

Table 8.1: DASY4 probes employed for the experimental evaluation. The dynamic range was equal or larger than 0.1 - 3 GHz and the linearity better than ± 0.2 dB for all probes

probe type	dia- meter [mm]	dynamic range	dev. of axial isotropy [dB]	dev. of spherical isotropy [dB]
ET3DV6 1374	6.8	$2\mu\text{W}-0.1\text{W/g}$	$<\pm 0.05$	$<\pm 0.20$
EF3DV2 4004	3.9	$2-1000\text{ V/m}$	$<\pm 0.05$	$<\pm 0.30$
H3DV6 6060	5.0	$0.01-2\text{ A/m}$	$<\pm 0.12$	$<\pm 0.20$

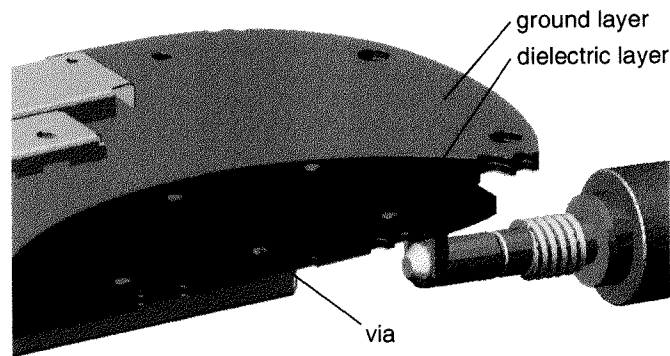


Figure 8.3: Numerical PCB structure consisting of 2 dielectric and 3 PEC layers as well as the interconnecting vias.

The phone was oriented with the PCB conformally aligned with an FDTD primary grid plane in order to reduce staircasing effects for the largely extended PEC structure. Whereas the basic dielectric parts like housing and buttons were maintained as imported into the FDTD platform, special attention was drawn to particular pieces which significantly influence the EM field behavior. The mechanical PCB part originally consisted of just one single PEC block; this had to be changed in order to represent internal losses due to the dielectric layers. Five separate layers were created: two dielectric ones which are embedded into three PEC ground layers. The grounds are

connected to each other by 50 vias (1 mm diameter) which are uniformly distributed over the entire PCB area. Figure 8.3 illustrates a detail of the PCB structure where part of the upper ground layer was removed to visualize the vias. The PCB ground and dielectric layers were modeled at a thickness of $110\ \mu\text{m}$ and $450\ \mu\text{m}$, respectively. A representation of the PCB structure incorporating additional components and details like conductor paths, cabling, ICs, etc. has not been performed.

All metallic parts are modeled as perfectly electric conductors, i.e., the affected components in the primary Yee grid are defined as equal to zero, which is acceptable at the observed frequencies (902 MHz, 1747 MHz). The dielectric components are represented within the FDTD simulation using the material parameters summarized in table 8.2. These parameters correspond with measured data provided by the manufacturers of the different electromechanical parts.

Table 8.2: Main dielectric parts of the mechanical CAD dataset and corresponding material parameters.

Part	ϵ_r	σ [$\frac{S}{m}$]
antenna bushing	2.5	3e-3
antenna cover	2.5	3e-3
PCB dielectric	4.5	7e-2
LCD glass	4.5	1e-2
LCD dielectric	3	1e-2
IrDA dielectric	3.5	2e-2
housing	3.5	2e-2
keypad/buttons	3.5	2e-2

8.5.2 Source Representation

In order to achieve proper excitation of the mobile phone structure, a source region was modeled which corresponds to the excitation of the physical phone. Figure 8.4 depicts the detailed setup in the CAD environment.

To achieve an electric separation from the antenna to the PCB, a small region of the upper PCB ground layer was isolated from its main part by introducing an air gap of 1 mm thickness. The discrete source was consequently placed in between the resulting PEC island-like plate and the remaining ground layer (red line). The plate itself was connected to the antenna stem using two PEC blocks, similar to the connection in the physical

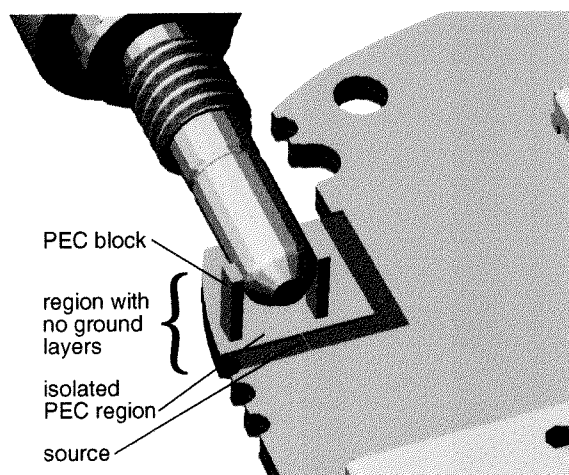


Figure 8.4: Excitation of the antenna - PCB structure in the modified source region.

model. To reduce capacitive coupling from the island-like PEC plate to the middle and lower ground layers, the grounding was removed and replaced with dielectric material within the specified region.

The source itself is modeled by a resistive voltage source as proposed in [30] with an internal source resistance of $50\ \Omega$. Due to the fairly broad extension of the source gap of 1 mm, it is discretized using three primary Yee grid edges, i.e., the source is applied to one edge whereas the remaining two edges are defined as PEC. As excitation, two signal forms have been applied:

1. To assess EM field information at a specific frequency, a harmonic sinusoidal excitation with a two period rising signal was used. The system reached steady state after 13 periods.
2. To assess broadband frequency domain information, a gaussian sine pulse with bandwidth $B = 1.5\ \text{GHz}$ was applied. For this case the simulation reached steady state after 8 ns.

Most of the results shown in section 8.6 are related to the GSM main frequency at transmit bands with center frequencies at 902 MHz and 1747 MHz specified as GSM900 and DCS1800 bands, respectively. They have been obtained by application of a sinusoidal continuous wave (CW) signal.

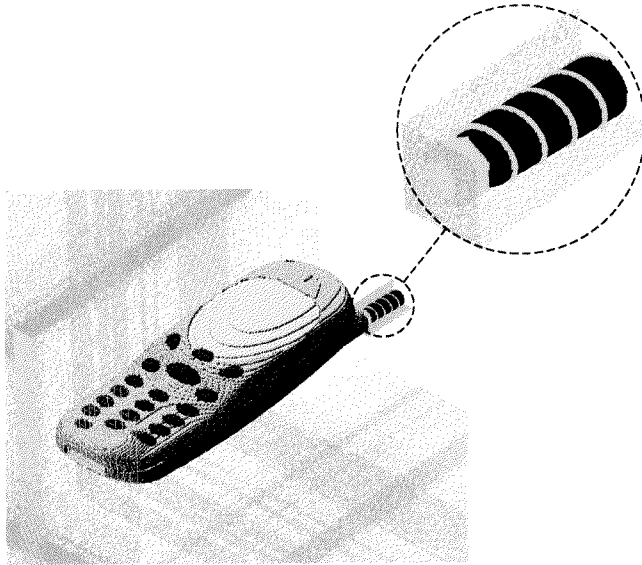


Figure 8.5: Application of FDTD grid: combination of graded mesh and subgrid (helical antenna).

8.5.3 Grid Generation / Simulation Parameters

The simulation platform SEMCAD incorporates semi-automated non-homogeneous grid generation which automatically adapts the mesh to a specific setup, e.g., increases the grid resolution within highly non-homogeneous or grid non-conformally aligned regions. In addition, the mesh can be manually configured to match particular user-defined requirements. Consequently, all materials are automatically assigned to every Yee cell in the grid.

In order to reduce memory and runtime requirements, the local refinement scheme (section 8.3) is applied to resolve certain regions of the phone model with a high resolution. The most crucial parts with respect to grid resolution are the antenna, including helical wire and monopole (0.65 mm wire diameter), as well as the PCB with its thin PEC ground layers (110 μm thickness).

Since the helical antenna is highly non-conformally aligned to the FDTD grid, it must be resolved by multiple cells in wire diameter in order to accurately represent the highly non-homogeneous field distribution. A spatial resolution of $0.2 \times 0.2 \times 0.1 \text{ mm}^3$ in x , y and z directions was chosen within the subgrid (1:2 refinement factor) surrounding the antenna, consisting of

about 500×10^3 mesh cells in total. Figure 8.5 depicts this configuration with combined graded mesh and subgrid.

Due to its grid conformal alignment in the z direction, the PCB structure can be resolved with a slightly higher resolution of $200 \mu\text{m}$, which properly resolves all dielectric and PEC ground layers. The subgrid used to model this region included the previous subgrid consisting of the helical antenna and the entire PCB, as well as all PCB parts which are connected to it such as shields and LCD holder. Furthermore, for configurations including head models, the subgrid was slightly extended in the z -direction, enclosing the most significant absorbing parts of the head. Its x , y and z axis resolution of $0.4 \times 0.4 \times 0.2 \text{ mm}^3$ results in a total number of about 5.5 million cells.

Within the free space simulation, the computational domain was extended about 0.75λ (at $f=902 \text{ MHz}$) in each spatial direction (distance phone - boundaries), which is just slightly larger than the phone itself. Since the subgrid enclosing the PCB has about the same spatial extent in the x and y directions, it was of no use for this simulation, for which reason just one subgrid was placed for the modeling of the antenna. All computations containing a head model placed beside the phone consisted of larger spatial domains extended by $1.25 \times 1.25 \times 1 \lambda$ in the x , y and z directions, which justifies the application of both subgrids. In order to avoid the introduction of additional errors caused by staircasing (section 8.3), the PCB (a significant PEC radiating part) was left conformally oriented to the FDTD grid. The standard positions for compliance testing were achieved by rotation of the dielectric lossy head models. For the outer grid in the free space simulation a non-homogeneous mesh using an increasing mesh step from 0.2 mm up to 7 mm (grading ratio = 1.5) was chosen, which leads to 4 million cells. The simulations including head models consisted of the same minimum and maximum mesh steps, whereby the human ear region was modeled with a $0.4 \times 0.4 \times 0.2 \text{ mm}^3$ grid resolution, leading to a total number of about 6 million cells.

All simulations were bounded by a perfectly matched layer (PML) [31] absorbing boundary condition (ABC) with a layer thickness of 8 cells.

8.6 Results and Validation

Within the experimental evaluations the physical device was put in operation using the Rhode & Schwarz Radio Communication Tester CTS55. The channel utilized in the measurements was the traffic channel ARFCN 62 ($f=902.4 \text{ MHz}$), which is the middle channel for the GSM900 system. The

power level was set to its maximum, i.e., Power Control Level 5 (33 dBm). The channel utilized in the DCS1800 measurements was the traffic channel ARFCN 698 ($f=1747.4$ MHz) which is the middle channel for DCS1800. The power level for DCS was set to its maximum, i.e., Power Control Level 0 (30 dBm). Communication between the tester and the device was established by active network link.

The phone design does not enable to directly measure the antenna input power with sufficient precision. For the purpose of this comparison, the antenna input power was determined indirectly by matching the simulated H-field distributions with measured ones from the DASY system. In order to achieve minimum uncertainty, a global least square fit was conducted on the H-field distributions of free space at different distances and inside the flat phantom. This enables a much more reliable determination of the input power at the feedpoint than conductive power measurements. The obtained values for the antenna input power are given in Table 8.3, to which all reported simulation results are normalized.

Table 8.3: Antenna Input Power at Feedpoint

Frequency	P_{in} [dBm]
GSM900	30.6
DCS1800	29.1

8.6.1 Validation of Antenna Model

Prior to the simulation of the complete phone model, the multiband antenna was examined as a monopole over a finite ground plane, in order to ensure proper representation of the antenna structure. Furthermore, the result was validated against measurements. In the measurement, the antenna was dismantled and its feed point was soldered to the center pin of the coaxial connector, the outer layer of which was soldered to the middle of a square-shaped copper plate with a thickness of 1 mm and a horizontal extension of 0.7×0.7 m². The impedance was measured using the HP 8753E network analyzer linked to the antenna via SMA connector at the backside of the plate.

This setup was reproduced using SEMCAD. The antenna CAD model was placed on a solid PEC ground structure consisting of the same spatial dimensions. In order to reduce the computational requirements, the antenna was modeled by application of a 1:8 subgridded region around it as shown in

figure 8.6. For the inner most subgrid a homogeneous resolution of $125 \mu\text{m}^3$ was applied, consisting of 2 million cells. Within the main grid a non-homogeneous mesh using mesh cells from 1 mm to 9 mm was used which (grading ratio = 1.4) led to a total of 1 million cells. Without making use of a local refinement scheme the computation domain would have consisted of 15 million cells.

Figure 8.7 compares the measured and simulated impedances in the frequency range from 800 MHz to 2 GHz. Regarding the complexity of the multiband antenna model, the general agreement of both real and imaginary parts is good. The resonance frequencies in particular match very well, leading to 948 MHz and 960 MHz (lower resonance) and to 1.695 GHz and 1.712 GHz (higher resonance) for measured and simulated impedances, respectively.

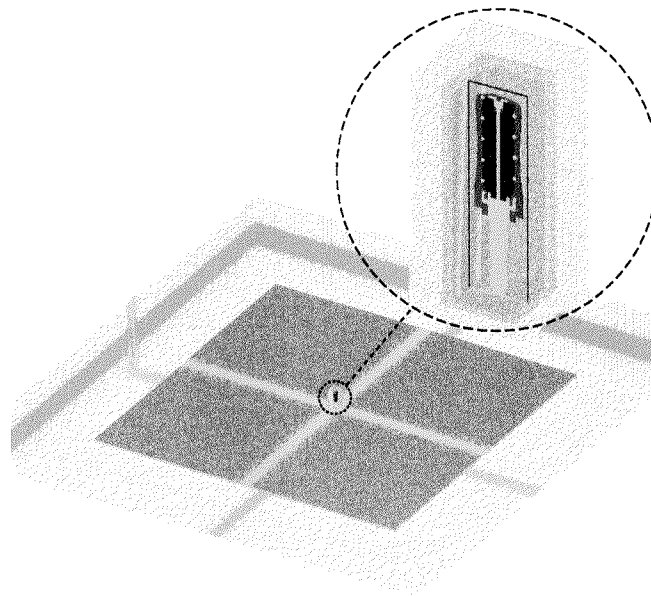


Figure 8.6: Multiband antenna placed on ground plate for broadband impedance assessment within FDTD simulation.

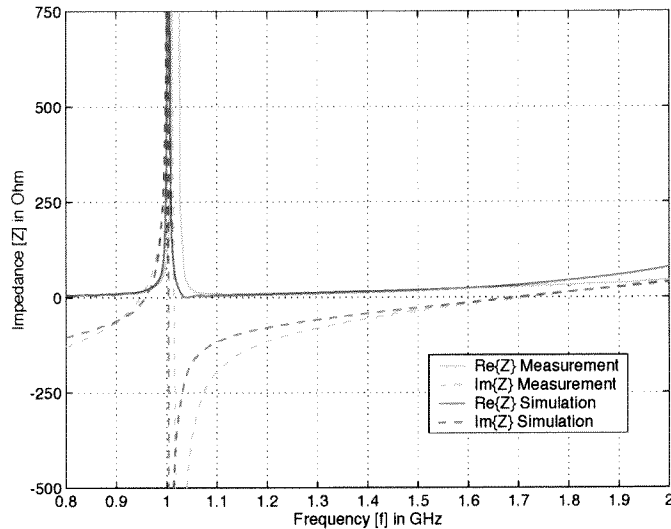


Figure 8.7: Multiband antenna: comparison of measured and simulated impedance in a frequency range from 800 MHz to 2 GHz.

8.6.2 EM Field Distribution - Free Space

Figure 8.8 depicts the measured and simulated E- and H-field distributions at the DCS1800 frequency. The fields were recorded in a plane located at 10 mm above the highest point of the phone (display), whereby the PCB was horizontally aligned in space. In order to reduce possible influence from nearby dielectrics, the phone was placed on styrofoam as shown in figure 8.2.

The comparison of the simulated to the measured distribution shows slight deviations in the region of the maxima, mainly close to the antenna. However, the general agreement for both characteristic E- and H-field patterns is very good.

8.6.3 Effect of the LCD Holder Connection

In order to assess the capabilities of the proposed FDTD simulation techniques with respect to MTE design purposes, special attention was given to major electromechanical parts which appeared to have a significant impact on the EM field behavior. Furthermore, the influence of FDTD grid resolution on the current distribution and EM field should be examined.

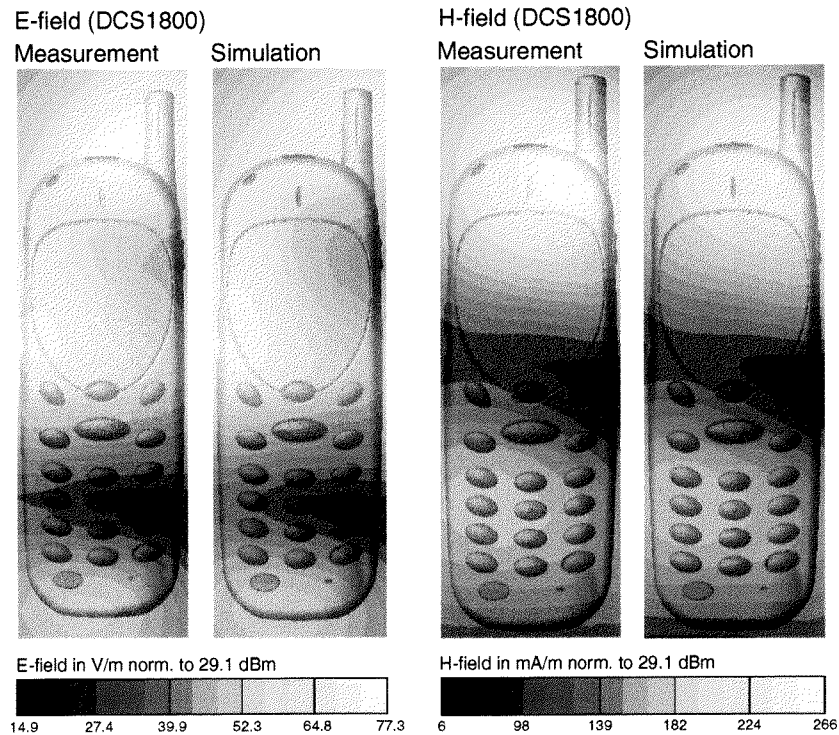


Figure 8.8: Comparison of simulation and measurement for the electric and magnetic field (DCS1800) shown in a plane located at 10 mm above the phone (from highest point). All fields are normalized to 29.1 dBm.

Particularly in the region of the liquid crystal display (LCD), major differences between simulation and measurements were obtained within an initial experimental assessment of the physical phone model. This effect occurs mainly at $f = 902$ MHz, since the current distribution on the phone at this particular frequency is localized to the LCD region. The LCD structure is mechanically fixed to the PCB by a metallic frame which itself is electrically connected to the ground of the PCB via 4 clamps. Figure 8.9 shows the configuration of this LCD holder.

A closer investigation of the physical holder structure revealed that the clamps actually do not create a proper RF short circuit to the PCB ground layer, while in the simulation a perfect electrical connection is achieved. Therefore the CAD model of the holder was modified in such a way that

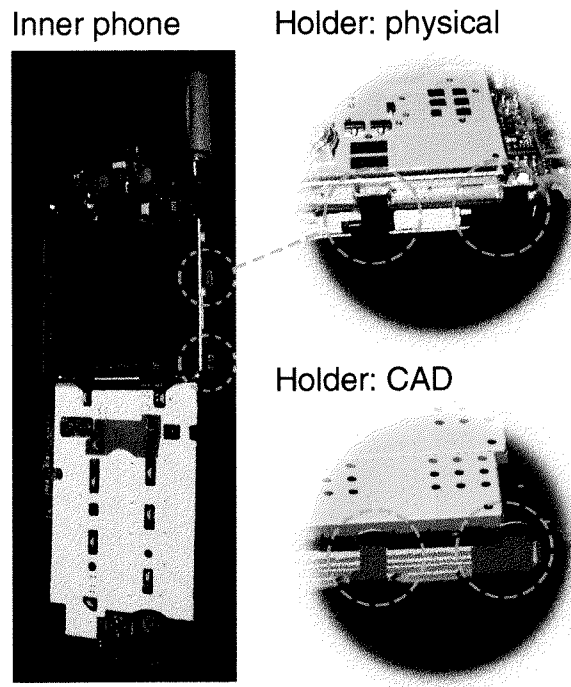


Figure 8.9: Metallic holder of the LCD structure: physical model and CAD representation.

part of the metallic clamp structure was removed, which made the holder float with respect to the PCB. The simulated magnetic field distributions in a plane located at 5 mm above the highest point of the phone housing is shown in figure 8.10 for the LCD holder in floating and connected configurations. It is observable that for a properly connected holder, the currents are capable of flowing on either side of the frame, whereas a floating holder leads to a much higher concentration of the H-field in the central region of the phone.

To verify the simulated effect, measurements have been performed using a physical phone model for which the LCD holder was released in one scenario and soldered to the PCB in the other scenario to force a floating and a short circuit situation. These modifications were realized on a third physical phone model in order not to change the high frequency behavior of the main device. All fields were normalized to 31.9 dBm input power similar to the procedure described in section 8.6.2. Since a different physical device was

used, the normalization input power value changed compared to all other results for the GSM900 band.

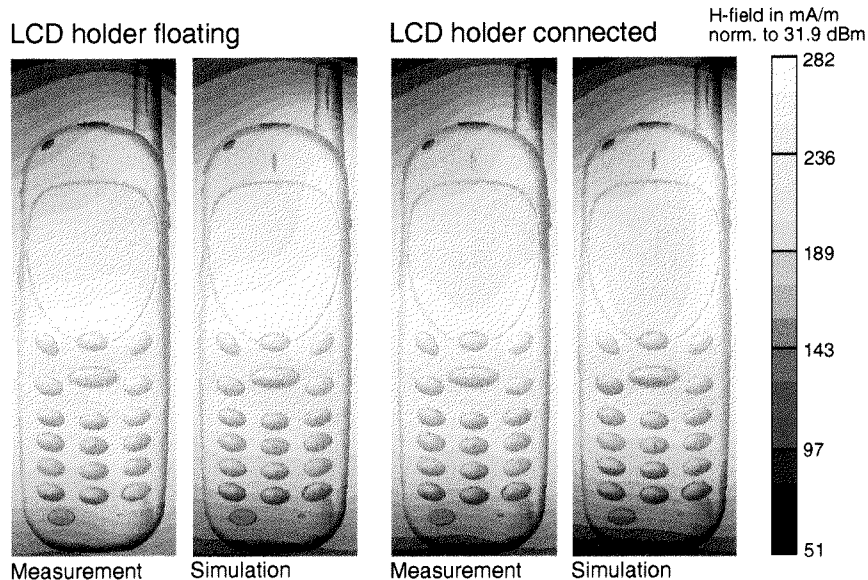


Figure 8.10: Comparison of connected and floating LCD holders for simulation and measurement in a plane located 5 mm above the phone (from highest point). All fields are normalized to 31.9 dBm.

As shown in figure 8.10 the LCD holder connection related EM field distribution predicted by the FDTD simulation is reproduced within the measured data. The characteristic near-field patterns, i.e., centralized and split current distributions on the LCD holder for the floating and short circuit connections, respectively, are obtained in both approaches. This basic example clearly demonstrates the capabilities of the described simulation technique, not only for verification of experimental methods but also to provide in depth analysis and understanding of the design.

8.6.4 Radiation Pattern - Free Space

In figure 8.11 the measured and simulated radiation patterns of the T250 mobile phone located in free space are compared. In the FDTD simulation the far-field pattern was determined using a near-to-far-zone transformation as proposed in [32]. The experimental assessment of the radiation

characteristics has been performed in a rectangular anechoic chamber. The measurement system within the anechoic chamber is automated; all data acquisition and turntable rotation is controlled by computer via GPIB. Figure 8.11 shows the radiation pattern for horizontal and vertical polarization within the xy and yz planes in dBi for the GSM900 and the DCS1800 band, respectively.

Good agreement between measurement and simulation is obtained for both polarizations in the cartesian planes observed. Due to the smaller amount of data points recorded in the experimental assessment, the field minima were not determined properly, leading to deviations in these regions. However, far-field data in general shows rather low sensitivity with respect to modeling detail for the numerical technique used. The three dimensional far-field patterns extracted from the simulation are depicted in the upper part of figure 8.12 for both frequency bands. As expected, the radiating phone structure including helical antenna operating in normal mode at $f=902$ MHz leads to a pattern similar to a dipole antenna. At $f=1747$ MHz the radiation is mainly determined by the PCB and the monopole section of the phone antenna, forming split radiation characteristics.

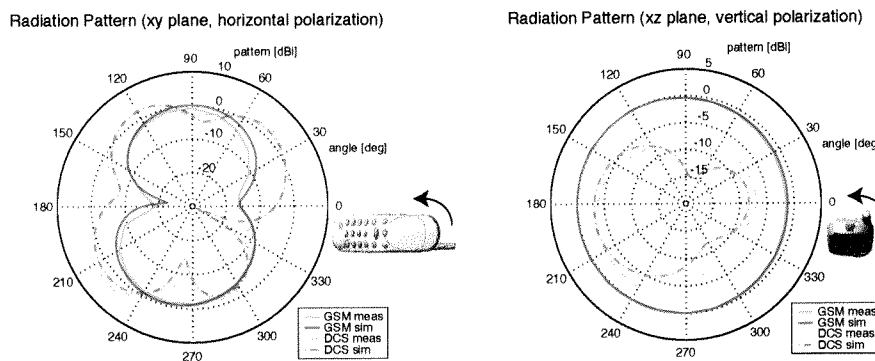


Figure 8.11: T250 phone in free space: measured and simulated horizontal and vertical polarizations of the 2-D radiation pattern within xy and xz cartesian plane for the GSM900 and the DCS1800 frequency bands.

8.6.5 Performance at Flat Phantom

Since the phone is usually operated in the vicinity of the human body, it is essential that the simulations can appropriately predict the performance for these conditions. The first evaluation was conducted at the well char-

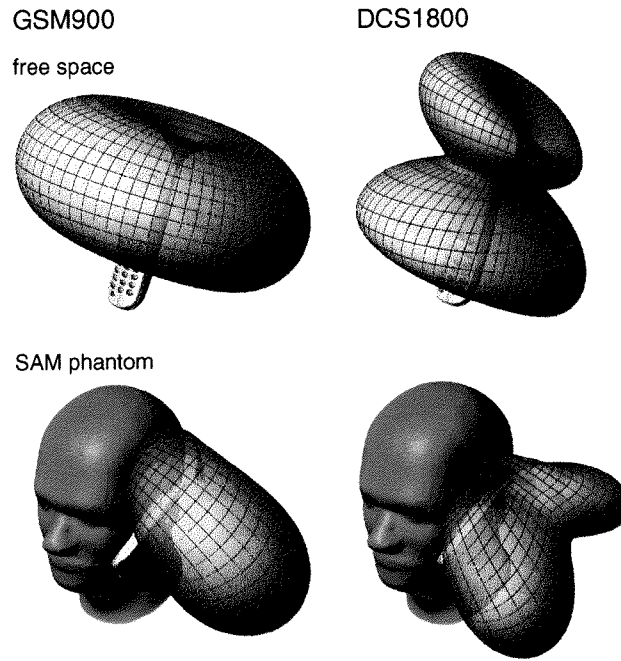


Figure 8.12: 3-D radiation pattern of the T250 mobile phone in free space as well as placed beside the SAM phantom operating in the GSM900 and the DCS1800 band.

acterized shape of a flat phantom, which is the test configuration for body-mounted operation. Figure 8.13 shows the configuration used and its spatial dimensions. The phone was positioned with its PCB horizontally aligned and its highest point touching the plastic shell of the SAM twin phantom flat section. The shell thickness was 4 mm, and the height of the brain tissue simulating liquid was 80 mm.

In lossy media the unit of interest in general is the specific absorption rate (SAR) which is defined as:

$$SAR = \frac{\sigma}{\rho} |E|^2 \quad (8.1)$$

whereby E is the induced electric field strength, σ is the conductivity, ρ the density of the medium. The dielectric parameters for liquid and shell which were used in the measurement and simulation at both GSM900 and DCS1800 frequencies are shown in table 8.4. They are consistent with the

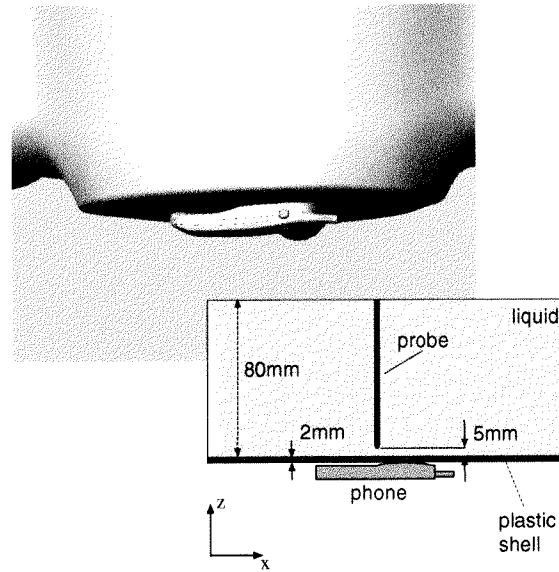


Figure 8.13: T250 mobile phone - SAM flat section: setup and spatial dimensions.

values proposed in [33], which were derived from worst-case considerations.

Figures 8.14 and 8.15 depict the measured and simulated SAR distributions within the liquid at 902 MHz and 1747 MHz for two distances of 5 mm and 10 mm from the inner surface of the shell. Although the regions of maxima show slight deviations between experimental and numerical data, very good agreement is obtained in most of the area observed. The strong dependence on the current distribution on the phone is manifested in figures 8.8 and 8.10, where the maximum H-fields are located above the lower LCD part and near the antenna at the GSM900 and DCS1800 frequencies, respectively.

Table 8.4: Material Parameters SAM Phantom

Material	902 MHz		1747 MHz	
	ϵ_r	$\sigma \left[\frac{S}{m} \right]$	ϵ_r	$\sigma \left[\frac{S}{m} \right]$
Liquid	41.5	0.97	40.0	1.40
Shell	3.5	0	3.5	0

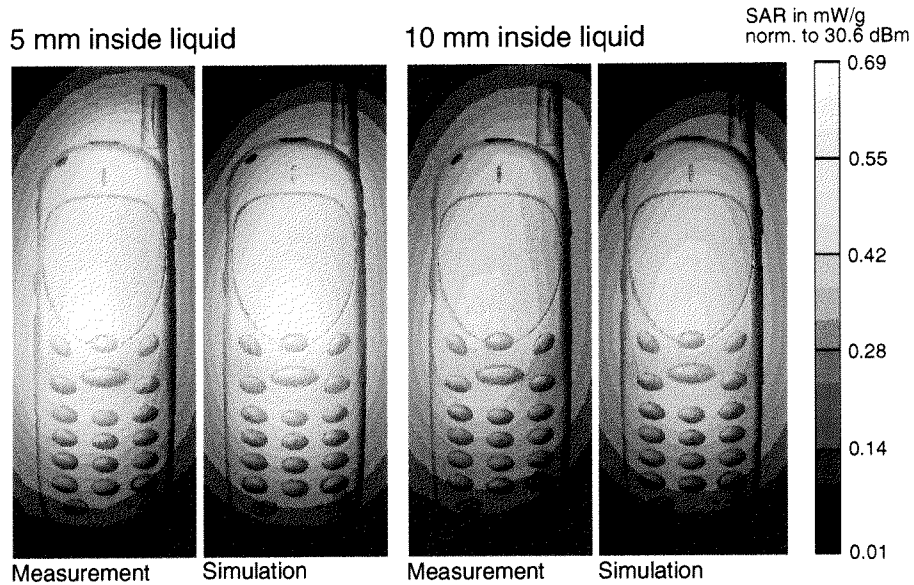


Figure 8.14: Comparison of simulation and measurement for the SAR distribution within the flat phantom at 902 MHz. The observation planes are located at 5 mm and 10 mm from the inner phantom surface. All fields are normalized to 30.6 dBm.

Table 8.5 summarizes the measured and simulated values for the peak SAR averaged over cubes of 1 g mass at both frequencies according to the procedure described in [34]. Comparison of the two methods yields excellent agreement for all values. The small deviations result from a possible cancellation of errors within the uncertainties of the simulation and the tolerances of the measurement system.

Table 8.5: 1 g averaged SAR for the phone - flat phantom configuration.

Type	SAR_M [W/kg]	SAR_S [W/kg]	Diff [%]
902 MHz _{1g}	0.71	0.74	+4.2
1747 MHz _{1g}	1.2	1.34	+11.7

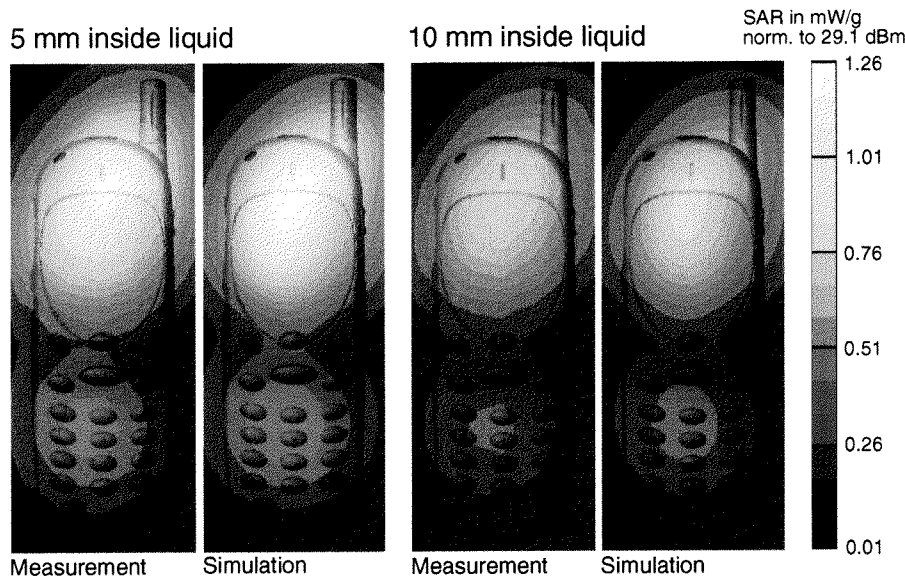


Figure 8.15: Comparison of simulation and measurement for the SAR distribution within the flat phantom at 1747 MHz. The observation planes are located at 5 mm and 10 mm from the inner phantom surface. All fields are normalized to 29.1 dBm.

8.6.6 Performance at the SAM Head

As performed in compliance testing of mobile phones, the device was placed beside the Specific Anthropomorphic Mannequin (SAM), the standard phantom defined in [27]. Figure 8.16 depicts the measurement setup with the T250 phone positioned at the SAM head as well as its corresponding CAD model within the simulation platform. The phantom consists of a dielectric shell with the shape of a human head and is filled with tissue simulating liquid. It is based on a large anthropometric survey conducted by the U.S. army [35] with its shape corresponding to the 90th percentile of the adult male heads measured. The reason for choosing an adult male head was that larger heads tend to absorb more electromagnetic energy [36]. Therefore, the adult male head yields a worse case exposure situation compared to, e. g., a child's head.

The thickness of the dielectric phantom shell ($\epsilon_r = 3.7$) is 2 mm. At the ear reference point, it is increased to 6 mm. The ear itself is shaped such

Measurement setup



CAD model within simulation



Figure 8.16: T250 phone model placed beside the SAM phantom in the measurements and within the simulation platform.

that it permits the accurate and repeatable positioning of the phone under test. The dielectric parameters of the tissue simulating liquid are the same as previously used in section 8.6.5 (table 8.4).

SAR distributions and averaged spatial peak SAR were assessed and compared for the *touch* and 15° *tilted* standard test positions as described in [37] and [27]. Illustration 8.17 depicts the measured and simulated SAR distributions in the SAM phantom at a distance of 4.7 mm normal to the inner shape of the shell. The scan was performed for the left side *touch* position at $f = 1747$ MHz and is logarithmically scaled, i.e., 0 dB are equal to the maximum peak SAR value obtained in the experimental data. Good

agreement is obtained between the measured and simulated distributions in the whole observation area.

The measured (M) and simulated (S) 1 g averaged peak SAR in *touch* and 15° *tilted* position at both frequencies are summarized in tables 8.6 and 8.7. Good to excellent agreement between the experimental and numerical data is obtained for all configurations. The low order of differences might again result from cancellation of errors occurring in the uncertainties of the simulation and the tolerances of the measurement system. In the *touch* position the SAR values show little dependence on frequency nor left/right application side. The strong variations in the 15° *tilted* position reveal the dominant influence of the high currents close to the antenna.

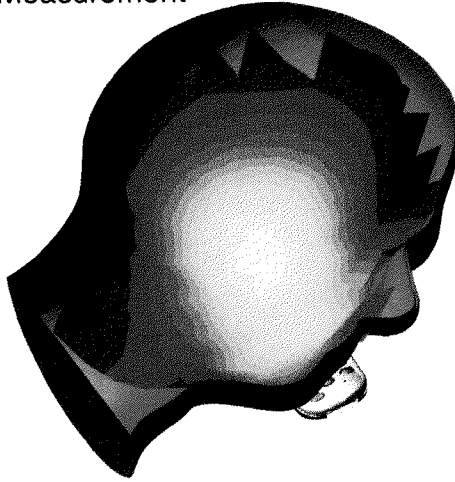
Table 8.6: 1 g averaged SAR in *Touch* position for the phantom - phone model.

Type	SAR _M [W/kg]	SAR _S [W/kg]	Diff [%]
902 ^{1g} _{right}	0.89	0.87	-2.2
902 ^{1g} _{left}	0.86	0.91	+5.8
1747 ^{1g} _{right}	0.97	1.01	+4.1
1747 ^{1g} _{left}	0.91	0.98	+7.7

Table 8.7: 1 g averaged SAR in *Tilted* position for the phantom - phone model.

Type	SAR _M [W/kg]	SAR _S [W/kg]	Diff [%]
902 ^{1g} _{right}	0.40	0.44	+10
902 ^{1g} _{left}	0.40	0.44	+10
1747 ^{1g} _{right}	1.03	1.01	-1.9
1747 ^{1g} _{left}	1.10	1.12	+1.8

Measurement



Simulation

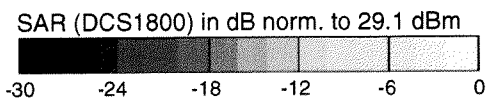
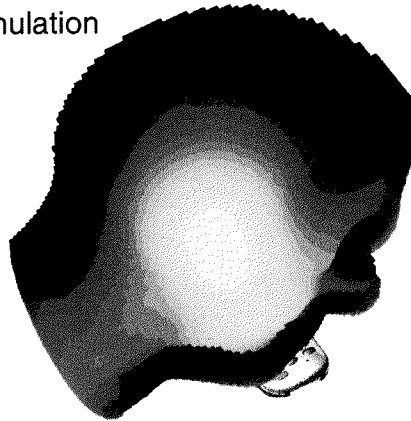


Figure 8.17: Measured and simulated SAR distribution within the SAM phantom (left side *touch* position, GSM1800).

8.6.7 Performance at Human Head

In order to evaluate the performance on an actual human head phantom, the performance of the device was also simulated next to the model of an actual human head. The High Resolution European Female head phantom (HR-EF-1) is the most detailed human head phantom currently available. It was generated from MRI images taken from a 40 year old female volunteer and consists of 121 different slices (figure 8.18). In the ear region, the slices have a thickness of 1 mm, while above and below the ear, the slice thickness was increased to 3 mm. The pinnae of the ear was pressed to the head in order to obtain a worst-case configuration, i.e., minimal separation between phone and head tissues. The high resolution of the ear region allows the accurate representation of the pinna as well as the anatomical details of the inner ear. The CAD model derived from the MRI scans is a precise numerical representation of the shapes of the organs and tissues in the slices. This allows the free positioning and tilting as well as flexible discretization within the numerical simulation software used without introducing uncertainties due to multiple sampling of fine anatomical details. 15 different tissue types were distinguished, the electrical parameters of which at the mobile phone frequencies were taken from [38].

The reference point for the positioning of the speaker of the phone was chosen to be 15 mm above the auditory canal opening, because this is the location of optimum acoustical coupling and therefore represents the position at which the phone is held during normal use.

In table 8.8 the 1 g averaged peak SAR obtained for the HR-EF-1 model in the *touch* and 15° *tilted* positions are compared to the SAM standard phantom at both frequencies. Due to the closer distance between the speaker part of the phone and head tissue for the HR-EF1 phantom (4 mm versus 6 mm), the overestimation of SAM is in the range of 10 - 30%.

8.6.8 Radiation Pattern - SAM Phantom

The 3-D far-field patterns of the mobile phone placed in the touch position with the SAM phantom at the GSM900 and the DCS1800 frequencies are shown in the lower part of figure 8.12. Whereas compared to the free space configuration the radiation characteristics are maintained, a shielding and absorbing influence of the lossy SAM head is obvious.



Figure 8.18: T250 phone model placed beside the high-resolution european female head phantom (HR-EF-1).

8.6.9 Computational Requirements

In table 8.9 the simulations including subgrid regions are compared to a simple graded mesh approach with respect to computational requirements. All computations have been performed on a 1.7 GHz Intel P4 machine operating under LINUX. A noticeable reduction of memory and runtime requirements is already achieved for the free space example consisting of a small simulation space. However, the comparison for larger spatial extensions including head models clearly reveals the needs of such FDTD local refinement schemes for complex real-world configurations. A powerful application is performed by combination of graded mesh and subgridding. Using only homogeneous grids in the whole simulation space leads to an unusable increase of the computational resources.

Table 8.8: 1 g averaged peak SAR in touch (to) and tilted (ti) left (l) hand positions for the SAM phantom (S) and the EF-1 non-homogeneous (E) model.

Type	SAR _S [W/kg]	SAR _E [W/kg]	Diff [%]
902 ^l _{to}	0.91	0.77	-15
902 ^l _{ti}	0.44	0.40	-9
1747 ^l _{to}	0.98	0.80	-18
1747 ^l _{ti}	1.12	0.73	-35

Table 8.9: Memory and runtime requirements for the phone in free space and beside the SAM phantom setup.

Type	Base-Cells	Memory	Time
Sub 1:2 _{free}	4.5×10^6	400 MB	8 h
Graded _{free}	11×10^6	850 MB	≈ 30 h
Homog _{free}	2×10^9	≈ 150 GB	≈ 200 days
Sub 2 \times 1:2 _{head}	6×10^6	1 GB	14 h
Graded _{head}	35×10^6	2.7 GB	≈ 4 days
Homog _{head}	8.5×10^9	≈ 1.5 TB	≈ 2.5 years

8.7 Conclusions

This study demonstrates that FDTD is a suitable technique for supporting engineers in the analysis, design and optimization of transmitters, even for the most complex cases such as mobile phones operating in the vicinity of the human body. The study also clearly revealed that efficient and flexible user-interfaces as well as graded meshes combined with robust subgrids are required in order to achieve the needed resolutions of small details in the range of $100 \mu\text{m}$ within locally restricted areas of the computational domain extended by one meter or more. Obvious items on the wish list for designers are shorter turn-around times and semi-automated optimization support, which are on our current research agenda together with features for uncertainty assessments.

References

- [1] FCC, "Evaluating compliance with FCC guidelines for human exposure to radiofrequency electromagnetic fields", Tech. Rep. Supplement C to OET Bulletin 65, Federal Communications Commission, Washington, D.C. 20554, June 2001.
- [2] CENELEC, *EN 50360, Product standard to demonstrate the compliance of mobile telephones with the basic restrictions related to human exposure to electromagnetic fields (300 MHz - 3 GHz)*, Brussels, July 2001.
- [3] CENELEC, *EN 50361, Basic standard for the measurement of Specific Absorption Rate related to human exposure to electromagnetic fields from mobile phones*, Brussels, July 2001.
- [4] IEC, *IEC 106/20/NP Generic product standard to demonstrate the compliance of electronic and electrical apparatus with the basic restrictions related to human exposure to electromagnetic fields (0 Hz - 300 GHz)*, July 2001.
- [5] A. Taflov, *Computational Electrodynamics - The Finite Difference Time Domain Method*, Artech House, Norwood, MA, 1995.
- [6] D.M. Sullivan, *Electromagnetic Simulation Using The FDTD Method*, IEEE Press, Piscataway, NJ 00885-1331, 2000.
- [7] K.S. Kunz and R.J. Luebbers, *The Finite Difference Time Domain Method for Electromagnetics*, CRC Press, Boca Raton, FL, 1993.
- [8] K.S. Yee, "Numerical solution of initial boundary value problems involving Maxwell's equations in isotropic media", *IEEE Transactions on Antennas and Propagation*, vol. 14, pp. 302-307, 1966.
- [9] M.A. Jensen and Y. Rahmat-Samii, "EM interaction of handset antennas and a human in personal communications", *Proceedings of the IEEE*, vol. 83, no. 1, pp. 7-17, Jan. 1995.
- [10] M. Okoniewski and M.A. Stuchly, "A study of the handset antenna and human body interaction", *IEEE Transactions on Microwave Theory and Techniques*, vol. 44, no. 10, pp. 1855-1864, Oct. 1996.

- [11] V. Hombach, K. Meier, M. Burkhard, E. Kühn, and N. Kuster, "The dependence of EM energy absorption upon human head modeling at 900 MHz", *IEEE Transactions on Microwave Theory and Techniques*, vol. 44, no. 10, pp. 1865–1873, Oct. 1996.
- [12] M.A. Jensen and Y. Rahmat-Samii, "Performance analysis of antennas for hand-Held transceivers using FDTD", *IEEE Transactions on Antennas and Propagation*, vol. 42, no. 8, pp. 1106–1113, Aug. 1994.
- [13] M. Burkhardt, N. Chavannes, K. Poković, T. Schmid, and N. Kuster, "Study on the FDTD performance for transmitters in complex environments", *Proceedings of the ICECOM, Dubrovnik*, pp. 83–86, Oct. 1997.
- [14] J.S. Colburn and Y. Rahmat-Samii, "Human proximity effects on circular polarized handset antennas in personal satellite communications", *IEEE Transactions on Antennas and Propagation*, vol. 46, no. 6, pp. 813–820, June 1998.
- [15] R. Holland, "Pitfalls of staircase meshing", *IEEE Transactions on Electromagnetic Compatibility*, vol. 35, no. 4, pp. 434–439, Nov. 1993.
- [16] M. Burkhardt, *Contributions Toward Uncertainty Assessments and Error Minimization of FDTD Simulations Involving Complex Dielectric Bodies*, PhD thesis, Diss. ETH Nr.13176, Zurich, 1999.
- [17] K.S. Nikita, M. Cavagnaro, P. Bernardi, N.K. Uzunoglu, S. Pisa, E. Pizzuzzi, J.N. Sahalos, G.I. Krikelas, J.A. Vaul, P.S. Excell, G. Cerri, S. Chiarandini, R. DeLeo, and P. Russo, "A study of uncertainties in modeling antenna performance and power absorption in the head of a cellular phone user", *IEEE Transactions on Microwave Theory and Techniques*, vol. 48, no. 12, pp. 2676–2685, Dec. 2000.
- [18] A.D. Tinniswood, C.M. Furse, and O.P. Gandhi, "Computations of SAR distributions for two anatomically based models of the human head using CAD files of commercial telephones and the parallelized ftd code", *IEEE Transactions on Antennas and Propagation*, vol. 46, no. 6, pp. 829–833, June 1998.
- [19] A. Schavioni, P. Bertotto, G. Richiardi, and P. Bielli, "SAR generated by commercial cellular phones - phone modeling, head modeling and measurements", *IEEE Transactions on Microwave Theory and Techniques*, vol. 48, no. 11, pp. 2064–2071, Nov. 2000.

- [20] O.P. Gandhi, G. Lazzi, A. Tinniswood, and Q.-S. Yu, "Comparison of numerical and experimental methods for determination of SAR and radiation patterns of handheld wireless telephones", *Bioelectromagnetics*, vol. 20, pp. 93–101, 1999.
- [21] M. Jayawardene, O. Leisten, P. McEvoy, R. Seager, J.C. Vardaxoglou, and A. Wingfield, "Comparative study of numerical simulation packages for analysing miniature dielectric-Loaded bifilar antennas for mobile communication", *Eleventh International Conference on Antennas and Propagation, IEE, London, UK*, vol. 1, pp. 260–264, 2001.
- [22] M. Siegbahn, "Master thesis: A mesh refinement method for FDTD and calculations on helical antennas for mobile communications", Tech. Rep., Uppsala University School of Engineering, Sweden, 1996.
- [23] W. Heinrich, K. Beilenhoff, P. Mezzanotte, and L. Roselli, "Optimum mesh grading for finite-Difference method", *IEEE Transactions on Microwave Theory and Techniques*, vol. 44, no. 9, pp. 1569–1574, Sept. 1996.
- [24] SEMCAD, "Reference manual for the SEMCAD simulation platform for electromagnetic compatibility, antenna design and dosimetry", *SPEAG - Schmid & Partner Engineering AG*.
- [25] N. Chavannes and N. Kuster, "Advantages and limitations of FDTD subgrid schemes for EM transmitters embedded within highly complex environments", *Proceedings of the 16th International Conference on Applied Electromagnetics and Communications ICECOM, Dubrovnik, Croatia*, pp. 85–89, Oct. 2001.
- [26] T. Schmid, O. Egger, and N. Kuster, "Automated e-field scanning system for dosimetric assessments", *IEEE Transactions on Microwave Theory and Techniques*, vol. 44, pp. 105–113, Jan. 1996.
- [27] IEEE, *Std. 1528-200X, Recommended Practice for Determining the Spatial-Peak Specific Absorption Rate (SAR) in the Human Body Due to Wireless Communications Devices: Experimental Techniques*, June 2000.
- [28] Klaus Meier, Michael Burkhardt, Thomas Schmid, and Niels Kuster, "Broadband calibration of E-field probes in lossy media", *IEEE Transactions on Microwave Theory and Techniques*, vol. 44, no. 10, pp. 1954–1962, Oct. 1996.

- [29] Katja Poković, Thomas Schmid, and Niels Kuster, "Robust setup for precise calibration of E-field probes in tissue simulating liquids at mobile communications frequencies", in *ICECOM'97*, Dubrovnik, October 15–17, 1997, pp. 120–124.
- [30] M.J. Picket-May, A. Taflove, and J. Baron, "FD-TD modeling of digital signal propagation in 3-D circuits with passive and active loads", *IEEE Transactions on Microwave Theory and Techniques*, vol. 42, pp. 1514–1523, 1994.
- [31] J.P. Berenger, "A perfectly matched layer for the absorption of electromagnetic waves", *Journal of Computational Physics*, Oct. 1994.
- [32] A. Taflove and K.R. Umashankar, "Radar cross section of general three-dimensional structures", *IEEE Transactions on Electromagnetic Compatibility*, vol. 25, pp. 433–440, 1983.
- [33] Antonios Drossos, Veli Santomaa, and Niels Kuster, "The dependence of electromagnetic energy absorption upon human head tissue composition in the frequency range of 300–3000 MHz", *IEEE Transactions on Microwave Theory and Techniques*, vol. 48, no. 11, pp. 1988 – 1995, Nov. 2000.
- [34] Subcommittee 2 IEEE SCC-34, *P1529/2000X, Recommended Practice for Determining the Spatial-Peak Specific Absorption Rate (SAR) Associated with the Use of Wireless Handsets - Computational Techniques*, Piscataway, USA, Sept. 2000.
- [35] Gordon et al., *1988 Anthropomorphic survey of U.S. army personnel: Methods and summary statistics*, Technical Report NATICK/TR-89/044, 1989.
- [36] Frank Schönborn, Michael Burkhardt, and Niels Kuster, "The difference of EM energy absorption between adults and children", *Health Physics*, vol. 74, no. 2, pp. 160–168, Feb. 1998.
- [37] CENELEC, *prEN 50360, Product standard to demonstrate the compliance of mobile telephones with the basic restrictions related to human exposure to electromagnetic fields (300 MHz–3 GHz)*, Brussels, June 2000.
- [38] C. Gabriel, "Compilation of the dielectric properties of body tissues at RF and microwave frequencies", Tech. Rep., Report N.AL/OE-

160

TR-1996-0037, Occupational and environmental health directorate, Radiofrequency Radiation Division, Brooks Air Force Base, Texas (USA), June 1996.

Part IV
Conclusions

Seite Leer /
Blank leaf

Chapter 9

Conclusion and Outlook

Summing up the results achieved as well as the contributions performed within this PhD thesis, all objectives described in the introduction have been fully achieved.

The rigorous analysis of various proposed techniques, mainly in relation to subgridding schemes, enabled the development of two novel 3-D based methods for FDTD local grid refinement. Excellent performance of the algorithms for numerous parameters was presented on the basis of various benchmarks. In particular the subgrid scheme provides a uniquely wide applicability and robustness compared to existing approaches. Within the framework of the KTI sponsored SEMCAD++ project, important contributions to the implementation of a whole EM simulation environment have been performed including the techniques described in this thesis. SEMCAD, providing support for grid-independent solid modeling, has proven to be an excellent basis for testing out new ideas, conducting benchmarks and demonstrating the efficiency of final implementations by simulation of highly complex problems. At the beginning of this thesis in 1998 the most enhanced MTE models consisted of square shaped helices mounted on PEC boxes. Today, commercially available mobile phones modeled by application of spatial resolution in the μm range can be completely analyzed within days.

Subsequent research studies directly related to the presented thesis could include:

- extension of the subcell method to a “true” 3-D processing as discussed at the end of chapter 5

- extension of the grid non-conformally aligned source model presented in chapter 5 to support multiple source forms, such as hard, voltage and added sources
- application of spatial non-homogeneous grid steps to the implemented subgridding scheme
- extension of the subgridding method presented in chapter 6 to serve as local absorbing boundary entities, i.e., discrete absorbers can be placed within a subdomain of the computational domain, e.g., to simulate an open boundary condition for coaxial cables, etc.
- combination of multi processing algorithms with subgrids, enabling the temporally parallel computation of multiple FDTD subdomains and leading to even shorter computation times
- application to FDTD thermal algorithms in a straightforward manner, due to the general interpolation based approach of the subgridding scheme
- extension of the developed and implemented local refinement algorithms by incorporation of static field solutions as discussed in chapter 4

Following the actual trends of the MTE and computation sector towards *pervasive computing* and body communication related applications, one may only imagine the level of complexity which will be handled within the coming decade. Multi-transmitter devices operating at different frequencies embedded within largely extended highly non-homogeneous environments are already today's state of the art. A simple example for such an application is, e.g., a person wearing a pacemaker, sitting in a car while using a GSM operating mobile phone which is connected via Bluetooth to a handsfree audio device.

The real-world example described in chapter 8 incorporating mobile phone and non-homogeneous human head model consisted of grid numbers in the range of $10^6 - 10^7$ (coarse grid) and $10^5 - 5 \cdot 10^6$ (subgrid) leading to computation times in the range of 15 hours (about 20 000 timesteps) on an Intel P4 1.7 GHz processor. Even for today's workstations, parallelization provides enormous computational capability, e.g., using a Beowulf cluster of about 400 Intel P4 processors clocked at 1.5 GHz leading to $3 \cdot 10^9$ Yee cells in memory and 1 hour running time for 10 000 timesteps (ETH *Asgard* project: Intel P3 Beowulf, 502 · 500/650 MHz, 500 GB RAM, LINUX). Even

linear extrapolation of computational power from the early 90s to today's standard PCs shows that such systems will also be available for the common user within 5-7 years.

The application of FDTD local refinement techniques in combination with enhanced modeling platforms will enable specifically tailoring the grid towards extreme spatial multi resolution environments, i.e., analysis of systems with R ratios of multiple 100 000 between the smallest cell size and the largest extension ($R \approx 5\,000$ for phone-head example from chapter 8):

- *pervasive computing*, in/on-body communications: embedding RF transmitter devices within multi-meter extended environments, wireless signal propagation within cellular environments
- biomedical applications of lasers: light backscattering from, or propagation through tissues that are in the millimeter range
- operation of integrated electronic and photonic devices and circuits: RF through optical electromagnetic wave propagation within microchips spanning $10\text{-}100\lambda$ but having critical structural features in the order of 0.001λ
- design of low-observable structures: RF/microwave backscattering from spatially extended scatterers requiring submillimeter-scale resolution

Due to its unlimited efficiency and computational power, the FDTD parallelization aspect is currently being closely investigated within the PhD thesis of my colleague Emilio Cherubini, in particular making the SEMCAD simulation platform applicable to distributed multiprocessing environments. LINUX based 64 bit CPU systems will dominate the number-crunching computational community within the next few years due to the excellent performance/price ratio. Further enhancements with respect to the KTI SEMCAD++ project which are currently being performed in the PhD thesis of my colleague Andreas Christ are related to minimizing dispersion errors in general FDTD meshes in combination with enhanced representation of material boundaries.

The high suitability of the SEMCAD environment for the rapidly emerging field of integrated optics will finally lead to a further extension of the platform within a subsequent KTI supported project by the middle of this year in a close cooperative effort between IIS, IT'IS and related industry partners.

Seite Leer /
Blank leaf

Appendix A

List of Symbols

α	attenuation constant [Np/m]
β	phase constant [1/m]
γ	propagation constant ($\gamma = \alpha + j \cdot \beta$)
ε	permittivity ($\varepsilon = \varepsilon_0 \cdot \varepsilon_r$)
ε_0	permittivity of vacuum [F/m] ($\varepsilon_0 = 1/\mu_0 c_0^2$)
ε_r	relative permittivity, dielectric constant [1]
η_0	characteristic wave impedance of vacuum [Ω] ($\eta_0 = 120\pi$)
ϕ	phase angle [degree or radian]
λ	wavelength [m]
μ	permeability ($\mu = \mu_0 \cdot \mu_r$)
μ_0	permeability of vacuum [H/m] ($\mu_0 = 4\pi \cdot 10^{-7}$)
μ_r	relative permeability [1]
ρ	tissue density [kg/m ³]
σ	electric conductivity [S/m]
σ_m	magnetic conductivity [Ω /m]
ω	angular frequency [rad/s] ($\omega = 2\pi f$)
A	area [m ²]
\vec{B}	magnetic induction [T = Vs/m ²]
c	specific heat [J/(kgK)]
c_0	velocity of light in vacuum ($c_0 = 2.99792458 \cdot 10^8$)
C	capacitance [F]
C_n	Courant-Friedrichs-Lewy number
d	distance, 1-D spatial extension [m]
\vec{D}	electric displacement [As/m ²]

\vec{E}	electric field [V/m]
f	frequency [Hz]
h	height, 1-D spatial extension [m]
\vec{H}	magnetic field [A/m]
j	imaginary unit ($j^2 = -1$)
\vec{J}	electric current density [A/m ²]
\vec{k}	wave vector [1/m]
l	length, 1-D spatial extension [m]
L	inductance [H=Vs/A]
$n\Delta t$	number of timesteps Δt
P	power [W]
R	resistance [Ω]
s	spatial length [m]
Δs	spacing in cartesian grid [m]
t	time [s]
Δt	time step [s]
T	temperature [K]
U	voltage [V]
v_p	phase velocity [m/s]
W	energy [J]
Δx	spatial Yee grid increment in cartesian x -direction [m]
Δy	spatial Yee grid increment in cartesian y -direction [m]
Z	impedance [Ω]
Z_{in}	input impedance [Ω]
Δz	spatial Yee grid increment in cartesian z -direction [m]

Appendix B

Bibliography

Papers Included in the Thesis

- [1] N. Chavannes and N. Kuster, “A novel 3-D CPFDTD scheme for modeling grid non-conformally aligned transmitter structures”, *IEEE Transactions on Antennas and Propagation*, Submitted, 2001.
- [2] N. Chavannes, J. Fröhlich, H.-U. Gerber, and N. Kuster, “A robust FDTD local refinement scheme for general application to enhanced antenna analysis”, *IEEE Transactions on Microwave Theory and Techniques*, Submitted, 2002.
- [3] N. Chavannes, R. Tay, N. Nikoloski, and N. Kuster, “RF design of mobile phones by TCAD: Suitability and limitations of FDTD”, *IEEE Antennas and Propagation Magazine*, Submitted, 2002.

Other Publications

- [4] M. Burkhardt, N. Chavannes, K. Poković, T. Schmid, and N. Kuster, “Study on the FDTD performance for transmitters in complex environments”, in *ICECOM'97*, Dubrovnik, October 15–17, 1997, pp. 83–86.
- [5] N. Chavannes, M. Burkhardt, and N. Kuster, “Simulation of wire antennas non-conformally oriented to the FDTD grid”, in *USNC/URSI National Radio Science Meeting*, Atlanta, Georgia, USA, June 1998, p. 73.

- [6] N. Chavannes and A. Christ, "Assessment of the minimum dimensions of a flat phantom for the simulation of an infinitely extended lossy half space", Tech. Rep., Institut für Feldtheorie und Höchstfrequenztechnik, ETH Zürich, 8092 Zürich, Switzerland, Jan. 1999.
- [7] K. Poković, T. Schmid, J. Fröhlich, N. Chavannes, and N. Kuster, "E-field probe with pseudo-vector information", in *21st Annual Meeting of The Bioelectromagnetics Society*, Long Beach, California, June 1999, p. 231.
- [8] K. Poković, T. Schmid, J. Fröhlich, N. Chavannes, and N. Kuster, "Numerical reconstruction routines for fields with linear or elliptical polarization", in *USNC/URSI National Radio Science Meeting*, Orlando, Florida, July 1999, p. 61.
- [9] N. Chavannes, M. Burkhardt, and N. Kuster, "Subcell modeling of antenna structures nonconformally oriented to the FDTD grid", in *15th International Conference on Applied Electromagnetics and Communications*, Zagreb, Croatia, Oct. 1999, pp. 55–59.
- [10] K. Poković, T. Schmid, J. Fröhlich, N. Chavannes, and N. Kuster, "E-field probe providing pseudo-vector information", in *15th International Conference on Applied Electromagnetics and Communications*, Zagreb, Croatia, Oct. 1999, pp. 110–113.
- [11] N. Chavannes, M. Burkhardt, and N. Kuster, "Numerical characterization of high resolution EM transmitters using a novel FDTD subgridding scheme", in *Millenium Conference on Antennas and Propagation*, Davos, Switzerland, Apr. 2000, vol. 1, p. 60.
- [12] M. Burkhardt, A. Christ, N. Chavannes, P. Regli, and N. Kuster, "FDTD simulations of antennas embedded in complex environments", in *Millenium Conference on Antennas and Propagation*, Davos, Switzerland, Apr. 2000, vol. 1, p. 96.
- [13] N. Chavannes and N. Kuster, "Numerical optimization of EM transmitters in complex environments by application of a novel FDTD subgrid scheme", in *USNC/URSI National Radio Science Meeting*, Salt Lake City, Utah, July 2000, p. 86.
- [14] N. Kuster and N. Chavannes, "Latest progress in analysis and synthesis RF tools for optimization of handheld transceivers (invited)", in *KEES, Seoul, Korea*, Aug. 2000.

- [15] N. Kuster and N. Chavannes, "Tutorial workshop: Interaction between antennas and the human body contents", International Symposium on Antennas and Propagation (ISAP 2000), ACROS Fukuoka, Japan, August 21, 2000.
- [16] N. Kuster and N. Chavannes, "Tutorial workshop: RF design criteria and performance assessment for handheld transceivers including an update on compliance standards (invited)", Mitsubishi Electric Corporation, Amagasaki, Japan, August 25th, 2000.
- [17] N. Kuster and N. Chavannes, "Novel RF design tools for optimization of handheld transceivers including an update on compliance standards (invited)", Technical Seminar at MITC, Tokyo, Japan, August 28th, 2000.
- [18] N. Kuster and N. Chavannes, "Analysis and synthesis RF tools for optimization of handheld transceivers (invited)", Seminar of KEES, Seoul, Korea, August 29th, 2000.
- [19] N. Chavannes and N. Kuster, "Advantages and limitations of FDTD subgrid schemes for the simulation of EM transmitters in the vicinity of the human body", in *Millenium Workshop on Biological Effects of Electromagnetic Fields*, Heraklion, Kreta, Greece, Oct. 2000, pp. 241–250.
- [20] A. Christ, N. Chavannes, K. Pokovic, H.-U. Gerber, and N. Kuster, "Numerical and experimental comparison of human head models for SAR assessment", in *Millenium Workshop on Biological Effects of Electromagnetic Fields*, Heraklion, Kreta, Greece, Oct. 2000, pp. 234–240.
- [21] N. Kuster, K. Poković, and N. Chavannes, "Technical trend on SAR measurements (invited)", ARIB Headquarter, Tokyo, April 5th, 2001.
- [22] N. Chavannes, H.-U. Gerber, A. Christ, J. Fröhlich, H. Songoro, and N. Kuster, "Next generation FDTD modeling capabilities for enhanced analysis of bioelectromagnetic interaction phenomena", in *2001 The Bioelectromagnetics Society*, St. Paul, Minnesota, USA, June 2001, p. 66.
- [23] A. Christ, N. Nikoloski, N. Chavannes, and N. Kuster, "Comparison of human head models for the compliance testing of mobile telephone equipment", in *2001 The Bioelectromagnetics Society*, St. Paul, Minnesota, USA, June 2001.

- [24] N. Chavannes, H.-U. Gerber, A. Christ, J. Fröhlich, H. Songoro, and N. Kuster, "Advances towards next generation FDTD modeling capabilities", in *Proceedings of the AP-S International Symposium and USNC/URSI National Radio Science Meeting*, Boston, Massachusetts, USA, July 2001, p. 257.
- [25] A. Christ, K. Poković, H.-U. Gerber, N. Chavannes, , and N. Kuster, "Experimental and numerical comparison of human head phantoms for SAR assessment at 900 and 1800 MHz", in *Proceedings of the AP-S International Symposium and USNC/URSI National Radio Science Meeting*, Boston, Massachusetts, USA, July 2001.
- [26] N. Chavannes, H.-U. Gerber, A. Christ, J. Fröhlich, H. Songoro, and N. Kuster, "Recent progress in FDTD modeling capabilities for analysis of transmitters operating in the vicinity of biological bodies", in *2001 International Congress of the European BioElectromagnetics Association*, Helsinki, Finland, Sept. 2001, pp. 73–74.
- [27] W. Kainz, N. Nikoloski, E. Schuhmacher, R. Überbacher, N. Chavannes, and N. Kuster, "High resolution animal models for numerical dosimetry", in *2001 International Congress of the European BioElectromagnetics Association*, Helsinki, Finland, Sept. 2001.
- [28] N. Chavannes, H.-U. Gerber, A. Christ, J. Fröhlich, H. Songoro, and N. Kuster, "Advances in FDTD modeling capabilities for enhanced analysis of antennas embedded in complex environments", in *2001 Proceedings of the International Conference on Electromagnetics in Advanced Applications*, Torino, Italy, Sept. 2001, pp. 353–356.
- [29] N. Chavannes, H.-U. Gerber, A. Christ, and N. Kuster, "Advantages and limitations of FDTD subgrid schemes for em transmitters embedded within highly complex non-homogeneous environments", in *2001 Proceedings of the 16th International Conference on Applied Electromagnetics and Communications*, Dubrovnik, Croatia, Oct. 2001, pp. 85–89.
- [30] A. Christ, N. Chavannes, N. Nikoloski, H.-U. Gerber, K. Poković, and N. Kuster, "Numerical and experimental evaluation of human head phantoms for the compliance testing of mobile telephone equipment", *to be submitted*, 2002.

Curriculum Vitae

Education

- Dipl. El.-Ing. ETH, degree 1998
Swiss Federal Institute of Technology, Zurich, Switzerland
Major: Electromagnetic Fields and Microwave Electronics
- Matura Gymnasium, degree 1991
Berne, Switzerland
- Primary School, 1979 - 87
Berne, Switzerland

Professional Experience

- Research Engineer 2/96 - 10/96
Siemens Microwave Research Laboratory
Zurich, Switzerland
- Graduate Research Assistant 4/98 - 1/00
Laboratory for Electromagnetic Fields and Microwave Electronics
Faculty of Electrical Engineering, ETH Zurich, Switzerland
- Graduate Research Assistant 1/00 - present
Laboratory for Integrated Systems
Faculty of Electrical Engineering, ETH Zurich, Switzerland

Awards

- C.C. Johnson Memorial Award, Platform Presentation, 2nd Place June 2001
Bioelectromagnetics Society

Personal data

- Birthdate: 25 April 1972 in Berne (Switzerland)
- Citizenship: Swiss
- Parents: Karin & Pierre Chavannes